

Wind Loading on Tensile Surface Structures - Experimental Approach -

Jimmy Silvia Georges Colliers

Master thesis submitted under the supervision of
Prof. dr. ir. Marijke Mollaert
Prof. dr. Steve Vanlanduit

The co-supervision of
Ir. arch. Maarten Van Craenenbroeck

Academic year
2013-2014

In order to be awarded the Master's Degree in
Architectural Engineering

Part I Master Thesis

Abstract

English

Since the design and the application of tensile membrane structures developed fairly recently, a lot of expertise and research still has to be performed. Especially in the field of wind analysis accurate wind load determination has to be examined. Compared to conventional building typologies, these structures tend to be extremely vulnerable to wind because of the low self-weight-to-load-ratio. In general, conventional codes on wind design give upper bound values for the majority of structures, but the level of uncertainties increases as the building configuration deviates from the codified norms.

This master thesis forms an initial step in the experimental wind tunnel analysis on tensile membrane structures, and especially for the wind loading on hyperbolic paraboloid roof and canopy structures. The thesis is composed of 3 main parts. The first part illustrates the current Eurocode procedure for determining the wind loads on common building geometries. The key concepts for basic wind design are introduced according to the chronological calculation steps and evaluated for membrane canopy structures. The pressure coefficient distributions are discussed for flat and duo-pitch roofs and canopies, in order to evaluate the fabrication techniques of the models, validate the accuracy and precision of the measurements and to create a reference-testing field for the research on hyperbolic paraboloid roof structures. The second part focuses on the research for appropriate modelling and wind tunnel testing procedures for double curved canopy structures. A feasibility study on production process and material is performed based on most important model requirements and directories, among them the simultaneous pressure measurement on the upper and lower face of very thin roof structures. Three thin-shelled rigid roof structures are fabricated, i.e. a flat roof, a duo-pitch roof and a hypar roof, all equipped with removable walls to investigate the wind load on building roofs and open canopies. The third part displays the outcome of the experimental wind tunnel analysis. Wind tunnel testing is used in a first stage for validation of conventional building typologies in accordance to relevant codes and literature, and in a second stage for fundamental research of data on new membrane typologies. The recorded wind tunnel data is processed and evaluated for each test case. The models are tested under continuous rotation and for discrete angles of attack, as part of enclosed building envelope and as an open canopy itself. The rotation sequence is used to evaluate the wind pressure variation in function of the orientation, to define the most critic building orientations, and to assess the pressure alteration on the upper face of the roof for the open and enclosed state. The obtained pressure coefficient distributions for different angles of attack are visualised in charts and compared to EC1 – part 1.4 for flat and duo-pitch roofs and canopies, and to ‘Das Hängende Dach’, (Otto, 1954) for the hypar roof. Finally, the distributions for the hypar roof and canopy could be used for calculating wind loads on equivalent structures, and could form a basis for extensive research for the Eurocode on membrane structures.

Keywords: Membrane structures, Building and canopies roofs, Hyperbolic paraboloid roofs, Wind tunnel testing, Wind tunnel models, Pressure coefficients

Nederlands

Door de recente opmars in het ontwerp en vervaardigen van membraanstructuren is er een achterstand in expertise en onderzoek voor deze structuren. Vooral op het gebied van windanalyse is er nood aan het accuraat modelleren van windbelastingen. Vergeleken met conventionele gebouwtypologieën zijn deze structuren uiterst gevoelig voor wind, als gevolg van de lage eigengewicht-belasting verhouding. De conventionele normen inzake windbelasting geven over het algemeen bovengrenzen aan voor de meeste structuren, maar de onzekerheid neemt toe wanneer de gebouwconfiguratie afwijkt van wat in de normen wordt behandeld.

Deze masterthesis geeft een aanzet met betrekking tot het experimentele windtunnelonderzoek voor membraan-structuren, en specifiek voor de windbelasting op hyperbolische paraboloiden daken en afdaken. De thesis bestaat uit drie grote delen. Het eerste deel illustreert de procedure die gehanteerd wordt door de Eurocode voor het bepalen van windbelastingen op veel voorkomende gebouwvormen. De belangrijkste concepten voor de berekeningen worden geïntroduceerd en geëvalueerd voor membraanstructuren. De drukcoëfficiëntverdelingen voor platte daken, zadeldaken en -afdaken worden besproken om de mogelijke fabricagetechnieken van fysische modellen te evalueren, de precisie en nauwkeurigheid van de metingen te valideren, en om een referentiekader te creëren voor het onderzoek op hyperbolische paraboloiden dakvormen. Het tweede deel focust op het onderzoek naar gepaste fabricage- en windtunnel testprocedures voor dubbel-gekromde afdaken. Een haalbaarheidsstudie naar productieproces en materiaal is uitgevoerd op basis van de belangrijkste model-eisen, waaronder de simultane drukmeting aan de boven- en onderzijde van zeer dunne dakstructuren. Er werden drie dunwandige stijve modellen vervaardigd: een plat dak, een zadeldak en een hyperbolisch paraboloiden dak, allemaal voorzien van wegneembare muren om gesloten gebouwen en open afdaken te kunnen testen. Het derde deel geeft de resultaten van het windtunnelonderzoek. In een eerste fase worden de windtunneltesten gebruikt voor de validatie van de resultaten voor conventionele gebouwtypologieën in overeenstemming met de huidige normen en literatuur, terwijl ze in een tweede stadium worden gebruikt voor fundamenteel onderzoek naar de nieuwe membraantypologieën. De geregistreerde windtunneldata worden verwerkt en geëvalueerd voor elke testopstelling. De modellen worden getest onder continue rotatie en voor specifieke invalshoeken, met het dak enerzijds als onderdeel van een gesloten gebouw en anderzijds als een open afdak. De rotatiesequentie is gebruikt om de winddrukvariatie in functie van de oriëntatie te evalueren, de meest kritieke oriëntaties te bepalen, en om de drukwijziging op de bovenzijde van het dak te evalueren voor de open en gesloten toestand. De verkregen drukcoëfficiëntverdelingen voor verschillende invalshoeken worden gevisualiseerd in tabellen en vergeleken met EC1 – deel 1.4 voor platte daken, zadeldaken en -afdaken, en met ‘Das Hängende Dach’ (Otto, 1954) voor het hyperbolische paraboloiden dak. Tot slot kunnen de drukcoëfficiëntverdelingen voor het hyperbolische paraboloiden dak en afdak gebruikt worden voor de berekening van windbelastingen op vergelijkbare constructies en tevens een fundamentele basis vormen voor verder onderzoek in het kader de Eurocode voor het ontwerpen van membraanstructuren.

Trefwoorden: Membraan structuren, Gebouwdaken en afdaken, Hyperbolische paraboloiden daken, Wind tunnel testen, Wind tunnel modellen, Drukcoëfficiënten

Français

Les progrès récents dans la conception et la fabrication des structures textiles, nécessitent encore beaucoup de recherche et d'expertise. En particulier dans le domaine de l'analyse, la détermination précise de la pression du vent doit être examinée. Comparée aux typologies de construction classiques, ces structures sont très sensibles au vent, en raison de leur faible ratio poids-charge. En général, les normes relatives à la pression du vent donnent des valeurs limites supérieures pour la majorité des structures, mais l'incertitude augmente lorsque la configuration du bâtiment n'est pas reprise dans les normes établies.

Ce mémoire présente, pour les structures textiles, une étude initiale en soufflerie et spécifie la pression du vent sur les toitures et les auvents de forme parabolique hyperbolique. Le mémoire se compose de trois parties principales. La première partie illustre la procédure utilisée par l'Eurocode pour déterminer les actions de vent sur les types de structures courantes. Les concepts-clés de cette procédure sont présentés et évalués pour les structures constituées de membranes. Les distributions de coefficient de pression pour les toitures et les auvents plats et pentus sont analysées afin d'évaluer les techniques de fabrication des modèles, valider l'exactitude et la précision des mesures, et de créer une référence expérimentale pour les structures de forme parabolique hyperbolique. La deuxième partie se concentre sur les méthodes de fabrication et de contrôle des auvents à double courbure. Une étude de faisabilité pour la fabrication et le choix de matériau est basée sur les exigences principales, y compris la mesure simultanée de la pression sur la face supérieure et inférieure d'un modèle très mince. Trois modèles de toiture rigides ont été élaborés, une toiture plate, une pentue et une de forme parabolique hyperbolique, toutes équipées de cloisons amovibles permettant de mesurer la pression de vent sur les toitures des bâtiments et sur les auvents ouverts. La troisième partie présente les résultats de l'analyse expérimentale en soufflerie. Dans une première phase, les essais en soufflerie sont utilisés pour la validation des résultats des bâtiments de typologie classique, en conformité avec les normes et la littérature. La méthodologie est ensuite utilisée pour les nouvelles typologies d'architecture textile. Les données de soufflerie enregistrées sont traitées et évaluées pour chaque configuration. Les modèles sont testés en rotation continue et pour des angles d'attaque discrets, avec la toiture faisant partie d'une enveloppe fermée et positionnée comme auvent ouvert. La séquence de rotation est utilisée pour évaluer la variation de la pression du vent en fonction de l'orientation, pour déterminer les orientations les plus critiques, et pour évaluer la modification de la pression sur la face supérieure de la toiture pour les situations ouvertes et fermées. Les distributions de coefficient de pression obtenues pour différents angles d'attaque sont visualisées en forme de tableaux et comparées avec EC1 - partie 1.4 pour les toitures et les auvents plats et en pente, et avec "Das Hängende Dach" (Otto, 1954) pour la toiture en forme de parabolique hyperbolique. Finalement, les distributions pour la toiture et l'auvent en forme parabolique hyperbolique pourraient être utilisés pour le calcul des pressions de vent sur des structures similaires, et pourraient constituer une base pour des recherches approfondies pour l'Eurocode concernant les Structures-Membranes.

Mots-clés: Structures membrane, Toitures du bâtiment et auvents, Toitures en forme de parabolique hyperbolique, Essais en soufflerie, Modèles de soufflerie, Coefficients de pression

Foreword

At an early age, my interest in the construction industry has formed, and in particular for large engineering and architectural works. Throughout the years, this interest has grown significantly. Consequently, it was an easy choice to start the bachelor program of architectural engineering at the Vrije Universiteit Brussel, followed by the master program at the Brussels Faculty of Engineering in a collaboration between the Vrije Universiteit Brussel en the Université Libre de Bruxelles.

Throughout this training program, a broad base of knowledge was applied, ranging from pure analytical and mathematical competencies to more conceptual and cultural capabilities. It was this versatility that attracted me and suited my urge to build a wide field of expertise and knowledge. Since the third bachelor year onwards we were introduced to lightweight membrane structures. These currently developing lightweight structures combining structural efficiency and double curved shapes matched perfectly my desire for structural efficient, minimalistic and smoothly shaped structures. Account in addition, for my analytic attitude and the need for expertise on these structures, it was straightforward to perform my master thesis research on membrane structures. The subject of wind loading on tensile surface structures has been raised in response to the current challenges in wind design on membrane structures by prof. dr. ir. Mollaert M., prof. dr. Vanlanduit S. and ir. arch. Van Craenenbroeck M.

Hereby, I would like to thank all professors and their assistants for sharing their knowledge and expertise with full commitment to their disciplines of specialization. Moreover, I would especially like to thank my thesis supervisors for their expertise and assistance during the master thesis research of the last year. Furthermore, I would like to thank my friends and parents. The encouragement and support through moments of deadlines, jury presentations and exams has been an important incentive to insist and to successfully finish the study program of architectural engineering. Moreover, I would especially like to thank my parents to give me the opportunity to achieve the master degree of science in architectural engineering.

Jimmy Colliers

Acknowledgements

I would like to thank prof. dr. ir. Mollaert M., prof. dr. Vanlanduit S. and ir. arch. Van Craenenbroeck M. for the supervision of the research part of this master thesis and for giving me the opportunity to perform this research. Their enthusiasm, experience, assistance, and support regarding the research are gratefully acknowledged.

The experimental wind tunnel study was carried out at the Department of Toegepaste Mechanica, Vrije Universiteit Brussel, where access was provided to the large industrial open return wind tunnel and the Scanivalve measuring equipment. I would like to thank Wéry A. and Rezayat A. of the Department of Toegepaste Mechanica for the information regarding wind tunnel testing and for their assistance and help during the wind tunnel tests. Special thanks need to be expressed to the FablabXL at the Erasmushogeschool Brussels for the access to their Dimesnion 3D-printer, Cyborg Laser cutters and the BZT portal CNC milling machine. I would like to thank Standaert L for his assistance and help with the equipment and machines. Also special thanks to the Department of Toegepaste Meachnica for the financial support granted for the wind tunnel models, and to the Department of Civil Engineering for providing access to the laboratory where I fabricated the models. I would like to thank Heremans R. for his experience, assistance and help by the production of the IPC material. Furthermore, I would like to thank prof. arch. Lindekens J, prof. arch. Berlemont T., arch. Gonzáles A. G., ir. arch. Meyrant S. and ir. arch. Ney L. for the supervision of the design part of this master thesis. Their enthusiasm, experience, assistance, and support regarding the design are gratefully acknowledged.

Finally, I would especially like to thank my friends and parents. Their constant encouragement helped me to keep everything in perspective and successfully complete this master thesis.

Jimmy Colliers

Table of Contents

Part I Master Thesis

Abstract.....	I
Foreword.....	IV
Acknowledgements.....	V
Table of Contents	VI
List of Figures	VIII
List of Tables.....	X

1 Introduction	1
1.1 Membrane structures	1
1.2 Problem statement.....	3
1.3 State-of-the-art.....	5
1.3.1 Tensile surface structures.....	5
1.3.2 Expertise and research.....	6
1.4 Methodology.....	7
1.5 Design.....	7
2 Wind Actions.....	8
2.1 Wind.....	8
2.2 Eurocodes.....	11
2.2.1 Eurocode NBN EN 1991-1-4:2005.....	12
2.2.2 Modelling of wind actions	12
2.2.3 Wind interaction	12
2.2.4 Pressure coefficients.....	13
2.2.5 Building roofs	13
2.2.5.1 Flat roof.....	14
2.2.5.2 Monopitch roof.....	15
2.2.5.3 Duo-pitch roof	16
2.2.5.4 Hypar roof	17
2.2.6 Canopy roofs.....	18
2.2.6.1 Monopitch canopy	19
2.2.6.2 Duo-pitch canopy.....	20
3 Wind Tunnel Models.....	21
3.1 Model Specifications	21
3.2 Fabrication process.....	22
3.2.1 Requirements.....	22
3.2.1.1 3D printing in ABS.....	22
3.2.1.2 Male CNC milling	23

3.2.1.3	Thermoforming of thermoplastics.....	24
3.2.1.4	Gypsum / IPC / Polyester composite on half-open mould.....	24
3.2.1.5	IPC composite in fully closed mould.....	25
3.2.1.6	Synthesis feasibility study.....	25
3.3	Wind Tunnel Models production	26
3.3.1	Flat Roof Structure.....	27
3.3.2	Duo-pitch Roof Structure	27
3.3.3	Hypar Roof Structure	29
4	Wind Tunnel Experiments	31
4.1	Experimental set-up	31
4.1.1	Wind tunnel.....	31
4.1.2	Scanivalve	32
4.1.3	Measurement set-up	33
4.1.4	Measurement methodology.....	33
4.2	Measurements	35
4.2.1	Flat roof	36
4.2.1.1	360°-rotation	36
4.2.1.2	Discrete angles of attack	37
4.2.2	Flat canopy.....	38
4.2.2.1	360°-rotation	38
4.2.2.2	Discrete angles of attack	39
4.2.3	Duo-pitch roof.....	40
4.2.3.1	360°-rotation	40
4.2.3.2	Discrete angles of attack	41
4.2.4	Duo-pitch canopy.....	43
4.2.4.1	360°-rotation	43
4.2.4.2	Discrete angles of attack	44
4.2.4.3	Discrete angles of attack – Free flow field	46
4.2.5	Hypar roof.....	48
4.2.5.1	360°-rotation	48
4.2.5.2	Discrete angles of attack	49
4.2.6	Hypar canopy.....	53
4.2.6.1	360°-rotation	53
4.2.6.2	Discrete angles of attack	55
5	Conclusion.....	58
5.1	Fabrication process of the wind tunnel models.....	58
5.2	Wind tunnel experiments.....	58
5.3	Future scope.....	59
6	Bibliography.....	60
<hr/>		
Appendix A: Wind Actions – Eurocode – Mathematical model for wind design		65
Appendix B: Pressure Measurement Graphs – 360°-rotation.....		73
Appendix C: Pressure Coefficient Distributions – Discrete angles of attack.....		82
<hr/>		
Part II	Design Portfolio	
Outdoor-Serpentine Theatre: Provincial Recreation Park ‘De Schorre’		1

List of Figures

Figure 1: Classification of tensile membrane constructions – [20].....	1
Figure 2: Typical membrane shapes – [45].....	1
Figure 3: Limited overview variety of tensile surface structures – Oeuvre of Fabritec Structures and Fabritecture – [18] [19]	2
Figure 4: Overview collapsed membrane structures – [1] [5] [21] [23] [28] [29] [36] [40] [41] [51] [55] [57] [58]	4
Figure 5: Key developments in tensile surface architecture – [20].....	5
Figure 6: Synclastic, anticlastic – [20]	5
Figure 7: Basic membrane shapes – [32].....	5
Figure 8: curvature – wind pressure – [20].....	5
Figure 9: The three main wind tunnel tests for membrane structures – [45].....	6
Figure 10: Outdoor-Serpentine Theatre at the Provincial Recreation Park 'De Schorre'	7
Figure 11: Methamorphosses I - P. Ovid, verse lines 56-66 – [37].....	8
Figure 12: Theory behind origin of wind currents – [15] [38]	9
Figure 13: Beaufort Scale –[59]	10
Figure 14: Logarithmic Interpolation overall and local pressure coefficients – [8]	13
Figure 15: Geometrical specifications of flat roofs – [8].....	14
Figure 16: Geometrical specifications of monopitch roofs – [8].....	15
Figure 17: Geometrical specifications of duo-pitch roofs – [8]	16
Figure 18: Geometrical specifications of a hypar roof with shape parameter of 4,7 – [47]	17
Figure 19: Airflow over and under canopy roofs – [8]	18
Figure 20: Geometrical specifications of monopitch canopies – [8].....	19
Figure 21: Geometrical specifications of duo-pitch canopies – [8].....	20
Figure 22: Wind tunnel models – [45] [64].....	21
Figure 23: 3D printing procedure	23
Figure 24: BZT portal CNC milling machine.....	23
Figure 25: Thermoforming process – [49] [63]	24
Figure 26: fabrication process wooden base	26
Figure 27: Virtual and scaled test models for wind tunnel experiments; flat, duo-pitch and hypar roof.....	26
Figure 28: Fabrication process flat and duo-pitch roof	28
Figure 29: Fabrication process of the hypar roof with a shape parameter of 11,3	30
Figure 30: Large wind tunnel at the VUB	32
Figure 31: Top and side view of the large section open return wind tunnel at the VUB.....	32
Figure 32: Top view of test section set-up for atmospheric boundary layer generation by Ir. De Paepe W.....	32
Figure 33: Scanivalve ZOC33/64Px – [56].....	32
Figure 34: Measurement set-up.....	33

Figure 35: Flow chart measurement methodology.....	34
Figure 36: Wind tunnel pressure measurements – continuous rotation – flat roof.....	36
Figure 37: Analysis flat roof – external pressure coefficients	
Left: Eurocode – external pressure coefficients – flat roof	
Right: Wind tunnel measurements – flat roof.....	37
Figure 38: Wind tunnel pressure measurements – continuous rotation – flat canopy.....	38
Figure 39: Analysis flat canopy – net pressure coefficients	
Left: Eurocode – net pressure coefficients – flat canopy	
Right: Wind tunnel measurements – flat canopy.....	39
Figure 40: Wind tunnel pressure measurements – continuous rotation – duo-pitch roof with pitch inclinations of 30°	40
Figure 41: Analysis duo-pitch roof – external pressure coefficients for perpendicular angle of attack	
Left: Eurocode – external pressure coefficients – duo-pitch roof with pitch inclinations of 30°	
Right: Wind tunnel measurements – duo-pitch roof with pitch inclinations of 30°	41
Figure 42: Analysis duo-pitch roof – external pressure coefficients for parallel angle of attack	
Left: Eurocode – external pressure coefficients – duo-pitch roof with pitch inclinations of 30°	
Right: Wind tunnel measurements – duo-pitch roof with pitch inclinations of 30°	42
Figure 43: Wind tunnel pressure measurements – continuous rotation – duo-pitch canopy with pitch inclinations of 30°	44
Figure 44: Wind tunnel net pressure coefficient distributions – discrete angles – duo-pitch canopy with pitch inclinations of 30°	44
Figure 45: Analysis duo-pitch canopy – net pressure coefficients for parallel and perpendicular angle of attack	
Left: Eurocode – net pressure coefficients – duo-pitch canopy with pitch inclinations of 30°	
Right: Wind tunnel measurements – duo-pitch canopy with pitch inclinations of 30°	45
Figure 46: Duo-pitch canopy wind tunnel model – boundary layer and free flow field test case	46
Figure 47: Analysis duo-pitch canopy – net and external pressure coefficients for parallel and perpendicular angle of attack	
Left: Wind tunnel measurements – duo-pitch canopy with pitch inclinations of 30° – boundary layer	
Right: Wind tunnel measurements – duo-pitch canopy with pitch inclinations of 30° – free flow field.....	47
Figure 48: Wind tunnel pressure measurements – continuous rotation – hypar roof with a shape parameter of 11,3.....	49
Figure 49: Wind tunnel external pressure coefficient distributions – discrete angles – hypar roof with a shape parameter of 11,3.....	49
Figure 50: Analysis hypar roof – external pressure coefficients with high corner under attack	
Left: Literature - Otto, F., Das Hängende Dach, 1954 –hypar roof with a shape parameter of 4,7	
Right: Wind tunnel measurements – hypar roof with a shape parameter of 11,3.....	50
Figure 51: Analysis hypar roof – external pressure coefficients with low corner under attack	
Left: Literature - Otto, F., Das Hängende Dach, 1954 –hypar roof with a shape parameter of 4,7	
Right: Wind tunnel measurements – hypar roof with a shape parameter of 11,3.....	51
Figure 52: Wind tunnel pressure measurements – continuous rotation – hypar canopy with a shape parameter of 11,3.....	54
Figure 53: Wind tunnel net pressure coefficient distributions – discrete angles – hypar canopy with a shape parameter of 11,3.....	55
Figure 54: Analysis hypar canopy – net pressure coefficients with high corner under attack	
Left: Wind tunnel measurements – hypar canopy with a shape parameter of 11,3	
Right: Simplified net pressure coefficient distribution – hypar roof with a shape parameter of 11,3	56
Figure 55: Analysis hypar canopy – net pressure coefficients with low corner under attack	
Left: Wind tunnel measurements – hypar canopy with a shape parameter of 11,3	
Right: Simplified net pressure coefficient distribution – hypar roof with a shape parameter of 11,3	57

List of Tables

Table 1: External pressure coefficients for flat roofs – [8].....	14
Table 2: External pressure coefficients for monopitch roofs – [8].....	15
Table 3: External pressure coefficients for duo-pitch roofs – [8].....	16
Table 4: External pressure coefficients for a hypar roof with shape parameter of 4,7 – [47].....	17
Table 5: Net pressure coefficients for monopitch canopies – [8].....	19
Table 6: Net pressure coefficients for duo-pitch canopies – [8].....	20
Table 7: Synthesis feasibility study of the production process.....	25
Table 8: Synthesis feasibility study of the material.....	25
Table 9: Wind tunnel characteristics.....	32
Table 10: Wind tunnel testing conditions – flat roof.....	36
Table 11: Wind tunnel testing conditions – flat canopy.....	38
Table 12: Wind tunnel testing conditions – duo-pitch roof with pitch inclinations of 30°.....	40
Table 13: Wind tunnel testing conditions – duo-pitch canopy with pitch inclinations of 30°.....	43
Table 14: Wind tunnel testing conditions – hypar roof with a shape parameter of 11,3.....	48
Table 15: Wind tunnel testing conditions – hypar canopy with a shape parameter of 11,3.....	53

1

Introduction

1.1 Membrane structures

Membrane structures are lightweight spatial structures that are characterised by the tensioned membrane surfaces. Conventionally, membranes are used as non-structural cladding element on facades or as non-structural partitioning element in frame-structures such as stages. Furthermore membrane surfaces are also used as structural elements that contribute to the stability of membrane structures. Depending on the structural use of the membranes, these structures can be categorized as pneumatic or tensile membrane structures. Pneumatic or air-inflated membrane structures owe their structural stability to an overpressure that pre-stresses the membranes while for tensile membrane structures the pre-stress is applied mechanically.

Tensile surface structures originate in a variety of applications, with a lot of different shapes, sizes, proportions, orientations, et cetera. These structures could be classified by the application and/or by the predominant structural shape. For example Figure 1 considers a particular classification of nine different tensile membrane constructions, ranging from covering, over internal, to attached and from open, over closed, to convertible. Furthermore, these structures can be assessed and subdivided into some simple but ‘typical’ membrane shapes as illustrated in Figure 2. Membrane structures have a large design freedom, however all concepts are based on a variety of high and low points. Depending on the number, the position and the kind of these high and low points, a structure could be catalogued as hyper, cone, arch, dome, wave type or a combination. A limited overview of different tensile surface structures is illustrated in Figure 3.

All of these tensile surface structures are mainly constituted from membranes, cables, struts and some other structural elements. The structural interaction between all components ensures the stability and stiffness of these structures. All loads are transferred to the surroundings by tension forces in the membranes and the cables, while the struts or columns transmit the compression forces. The stiffness of the flexible membranes is ensured by sufficient double curvature and mechanically applied pre-stress in the membrane. The membranes are mainly tensioned in a supporting system by boundary cables and turnbuckles. Turnbuckles are implemented to allow pre-stressing and adjusting the pretension in the cables and thus also the pretension of the membrane itself.

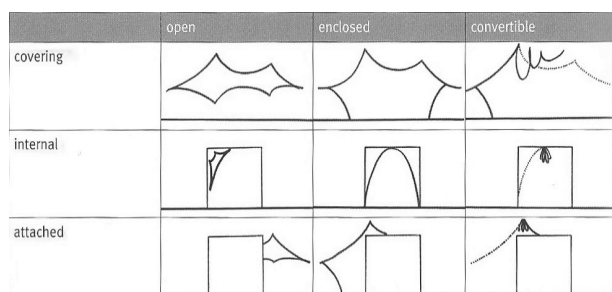


Figure 1: Classification of tensile membrane constructions – [20]

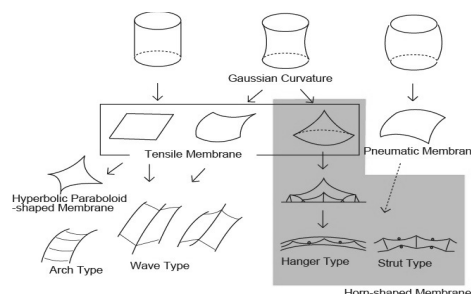


Figure 2: Typical membrane shapes – [45]

Tensile surface structures could be classified by the application and/or by the predominant structural shape. Membrane constructions could be classified from covering, over internal, to attached and from open, over closed, to convertible. Furthermore, these structures could be subdivided into some simple but ‘typical’ membrane shapes (hyper, dome, wave type or a combination).



Celebration Park – [18]



Hampton Battery – [18]



Dfw terminal a garage – [18]



Skysong ASU – [18]



Eckerd college – [18]



Expo boulevard Shangai – [18]



Greyhound terminal – [18]



Northside swim centre – [18]



MG transit centre – [18]



Four winds theater – [19]



Queensland tennis court – [19]



Modular aurora – [18]



Reid park zoo – [18]



BC Place Stadium – [18]



AS Venafro – [18]

Figure 3: Limited overview variety of tensile surface structures – Oeuvre of Fabritec Structures and Fabritecture – [18] [19]

Tensile surface structures exist in a wide variety of shapes (hyperbolic paraboloids, cones, arch forms, domes and wave types) and functions (covering, internal, attached, open, closed, convertible). Membrane structures are commonly applied as canopy structures, building integrated roofs or attached canopies. The function can range from solely solar shading to fully conditioning building components. Their application field ranges from small-scale solar shading pavilions over medium-scale canopies to large-scale stadium roofs or building skins.

1.2 Problem statement

Since the design and the application of tensile membrane structures developed fairly recently, a lot of expertise and research still has to be performed. Especially in the field of wind analysis accurate wind load determination has to be examined. The wind load determination on tensioned lightweight membrane structures is a complex problem. These structures are strongly affected by external loadings such as wind because of the low self-weight-to-load-ratio. Beside this membrane structures are applied and executed in a large variety of applications, shapes, sizes, proportions and orientations, causing the structural engineers to make simplifying assumptions and approximations during the calculation of membrane structures under wind load. These assumptions lead inextricably to over- or under-dimensioning of the structures. Over-dimensioning has mainly impact on the economical aspect. The engineer of today has to deal with durability, sustainability and optimal use of materials by limiting the excessive consumption of raw materials. Under-dimensioning on the other hand could cause more severe effects. It could jeopardise the safety and normal use of these structures. Recently several membrane structures have collapsed under wind loading around the world, causing economic and human loss. A limited overview of some collapsed tensile surface structures is illustrated in Figure 4. The failure of these structures is not limited to a specific application field but is observed for various membrane structures, ranging from temporary structures such as festival stages and tents, to permanent structures such as the indoor training facility of the Dallas Cowboys football team.

The low self-weight-to-external-load-ratio stipulates the vulnerability of these lightweight structures to external wind loads. The lack of expertise on these rather young structures causes a large number of incidents and structural failures that initiate from different origins. Most known structural failures are initiated by failure of the membranes due to rupture, failure of the supporting system due to bending of struts or snapping of cables, failure of the connections or fixtures between membrane and supporting structure and failure of the foundations due to uplift of the entire structure. Mark that in most cases a failure of one single element could cause the entire tensile surface structure to collapse, there the global structural stability of these structures depends on the interaction between all constituting elements. Besides, also non-destructive problems could occur, such as fluttering or galloping. These phenomena mainly avert the normal use and the comfort of these structures and could initiate creep and fatigue problems.

From this point of view, more accurate wind design is required for these tensioned membrane structures, without over-dimensioning the structural elements. In order to optimise the structural design of these lightweight structures under wind loading, a detailed wind analysis should be performed on some ‘typical’ membrane geometries (hyperbolic paraboloids, cones, arch forms, domes and wave types). A more accurate wind load determination on these ‘typical’ shapes will allow the structural engineer to perform a more accurate wind design, by drastically reducing the amount of simplifying assumptions and approximations. In this research domain experimental wind tunnel analysis on tensile surface structures could provide accurate wind load and safety factor determinations and could form a fundamental basis for a more general Eurocode on designing membrane structures. The need for accurate wind-load standards on these types of structures has already been stressed in several publications [24] [25], stating the lack of the current standards in governing the wind-resisting strength for these structures and the need for an industry-wide set of standards.



International Boatshow Nieuwpoort, Belgium – October, 2003 – [41]



Dallas Cowboys indoor practice facility, USA – May, 2009 – [28]



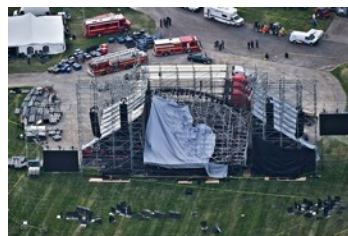
Film set County Antrim, Northern Ireland – September, 2011 – [5]



Pukkelpop Kiewit, Belgium – August, 2011 – [55] [57]



Indiana State Fair stage, USA – September, 2011 – [29] [58]



Toronto stage Radiohead, USA – June, 2012 – [40]



Circus tent Belize, USA – Oktober, 2010 – [1]



Arkansas Music Pavilion, USA – July, 2012 – [23]



Garden pavilion, Netherlands – August, 2012 – [36]



Star Phoenix smoking tent, Canada – January, 2014 – [21]



Flanders Open Rugby Dendermonde, Belgium – May, 2009 – [51]

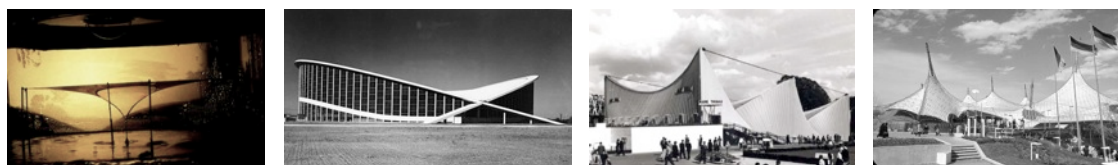
Figure 4: Overview collapsed membrane structures – [1] [5] [21] [23] [28] [29] [36] [40] [41] [51] [55] [57] [58]

Recently several membrane structures have collapsed under wind loading around the world, causing economic and human loss. Failure is observed for various membrane structures, ranging from temporary structures to permanent structures. The structural failures initiate from different origins: failure of the membranes due to rupture, failure of the supporting system due to bending of struts or snapping of cables, failure of the connections or fixtures between membrane and supporting structure or failure of the foundations due to uplift of the entire structure.

1.3 State-of-the-art

1.3.1 Tensile surface structures

The popularity and the use of tensile surface structures have been growing increasingly during the last 25 years. These structures were mainly introduced in the sixties by the soap bubble experiments of the German architect and structural engineer Frei Otto, who is considered as one of the pioneers in lightweight and tensile membrane structures. The roof of the Dorton Arena, also called the “Raleigh Livestock Arena” dates from 1952 and can be considered as the first modern tensile surface structure. The following years especially during expos and exhibitions, engineers and architects experimented a lot with this type of structures. For example at the Brussels Expo in 1958 the French architect and engineer Rene Sager engineered the Marie Thumas Pavilion, and at the Montreal Expo in 1967 Frei Otto designed the German Pavilion (Figure 5).



Soap film model, rail station
Stuttgart, 2000 – Otto F.

Dorton Arena, N-Carolina, 1952
– Severud F. & Nowicki M.

Marie Thumas Pavilion,
Brussel Expo 1958 – Sarger R.

German Pavilion, Montreal
Expo 1967 – Otto F.

Figure 5: Key developments in tensile surface architecture – [20]

The increased popularity is caused by some specific qualities and advantages of this type of structures. Membrane structures are very attractive and unconventional because of their sculptural and expressive architectural shapes. They are also extremely light compared to the more conventional building structures. This lightweight feature is enhanced by the intrinsic structural efficient use of materials in tensile surface structures. The structural stability is provided by adequate surface curvature and pre-stress in the membrane, rather than by the mass of the construction elements. The beneficial combination of low self-weight and tensile loading of the membrane allows these structures to span large areas with a minimum of material and internal supports. Another advantage of membrane structures is their possibly high translucency, which is related to the daylighting and the aesthetic possibilities of the architectural design. The translucency of the fabric depends strongly on the material properties of the fibres, the weave, the coating and the colour. In addition to above-mentioned characteristics, membrane structures tend to be flexible, mobile and temporary, convertible and adaptive. A drawback of lightweight structures is the increased sensitivity to external load conditions compared to conventional building structures. This phenomenon is physically perceptible by the relatively large deflections of the structure and is the natural consequence of the relative high ratio of the external loads (wind and snow) to the self-weight of the construction. Another determining factor for this phenomenon is based on the radius of membrane curvature and the membrane pre-stress, and thus the structural efficiency of the lightweight structure.

The geometry and form of tensile surface structures depends strongly on the boundary conditions i.e. the form and layout of the boundaries, the structural supporting system and the applied pre-stress in the membrane. These structures owe their structural stability and stiffness to the double curved shape of the membrane, which is generated by the tensile force equilibrium and the applied pre-stress in the membrane. The double curved spherical shape of synclastic surfaces is tensioned and stabilized by a pneumatic or hydraulic pressure, while the double curved saddle shape of anticlastic surfaces is tensioned and stabilized by a mechanically applied pre-stress (Figure 6). The structural behaviour and efficiency of the construction is positively affected by the flexibility of membrane structures. The load and stress paths in the membrane are function of the fabric orientation, i.e. warp and weft fibres, the shape of the membrane and thus the boundary layout and the supporting structure (Figure 7). The intrinsic flexibility allows these structures to respond to a particular external loading case by changing the overall membrane shape and rearranging the load and stress paths, within the allowed boundaries, to a more effective structural constellation to take the loads.



Figure 6: Synclastic, anticlastic – [20]



Figure 7: Basic membrane shapes – [32]



Figure 8: curvature – wind pressure – [20]

Tensile surface structures are very susceptible to external loadings. The relatively high stretch of the material can cause large deflections under snow and wind. Taking into account the flexibility and lightweight aspect of these structures it becomes obvious that the wind load, and especially the uplifting wind load, will become in most cases the most judicial design parameter for membrane stresses and cable forces in lightweight structures. From structural and serviceable point of view it is recommended to limit the large deflections under external loading to ensure stability and normal use of the structure. There are two main possibilities to reduce the deflections under external applied loads and to improve the structural behaviour of the membrane structure. Both approaches aim to increase the overall stiffness of the lightweight structure. The most efficient solution to reduce the deflections under wind is increasing the curvature of the flatter areas by reconsidering the boundary conditions, while increasing the pre-stress is an alternative solution. However, we have to consider that an increased curvature could generate a higher wind pressure. The wind pressure is related to the overall dimensions of the structure, the aerodynamics, the orientation, the wind angle of attack, et cetera. If we consider Figure 8, it is clear that in this case a higher curvature creates a larger face to the windward direction and thus a higher wind pressure.

1.3.2 Expertise and research

The need for expertise and research on the fairly recently developed tensile surface structures has led to the development of TensiNet [66], a Thematic Network for Upgrading the Built Environment in Europe through Tensile Structures. TensiNet is an association of partners spread over different European countries and aims to collect, share and exchange all available research and expertise by bringing together active researchers, engineers, designers, urban planners, architects, material suppliers, and checking authorities on the design and checking of tensile membrane architecture. The European Design Guide for Tensile Surface Structures [20] is a product of three years of work by the members of TensiNet. This guide should be seen as a state-of-the-art report and a first step in the direction of a European Normative document. Chapter 6: ‘*Structural Design Basis and Safety Criteria*’ gives a short overview of the currently available national design guides and codes for tensile surface structures and chapter 7: ‘*Design Loading Conditions*’ provides recommendations for loading combinations.

This European Design Guide illustrates clearly that one of the identified research priorities is the determination of accurate wind loadings on lightweight tensile membrane structures. Notwithstanding some experimental analysis and studies have already been performed, there is still need for additional accurate and representative research on the wind loading of membrane structures. There are three main approaches for wind tunnel analysis of tensile surface structures (Figure 9). On one hand, the structure could be considered to deform very little under external wind loading, which would not cause significant variation of the wind pressure coefficients. In this case rigid models will be used to generate the pressure distribution. Two categories are defined: local pressure tests and overall pressure tests on the membrane surface. On the other hand, the deformability and flexibility of the membrane structure should be considered incontestable in structures that deform significantly under external wind loading. This experimental analysis will use aero-elastic models for more detailed analysis of the sensitivity to the dynamics and side effects of wind loading on membrane structures. These wind tunnel tests are performed by optical measurements. In both approaches Finite Element Modelling could relate the wind tunnel analysis to numerical simulations such as Computational Fluid Dynamics (CFD). The interaction between the wind loading and the structural behaviour of the lightweight membrane constructions is a complex problem. Therefore wind tunnel experiments are needed to programme and improve CFD calculations for open canopy structures. A new coupling model between wind load and structural behaviour should be defined to optimise the numerical simulations for these membrane structures.

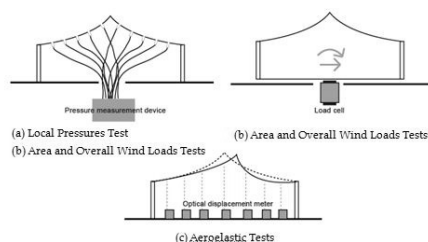


Figure 9: The three main wind tunnel tests for membrane structures – [45]

Rigid models are used for local and overall pressure tests on membrane structures that deform very little under wind loading. Aero-elastic models are used for optical tests on membrane structures that deform significant under wind loading.

Up to now the wind analysis for membrane structures is rather limited, to external pressure coefficient distributions of conical or horn shaped membrane roofs [9] [17] [31] [42] [45] [46] and hypar roofs [47] [53] [54] both part of an enclosed building envelope, and some specific case studies [3] [4] [11] [12] [43]. The main goal of the research aspect of this master thesis is to execute experimental wind tunnel testing, to analyse the obtained results in relation to the available literature, and to generate more accurate wind load determinations on some typical tensile membrane structures, i.e. hypars. The final objective is to gather knowledge and deeper insight in the structural behaviour of tensioned membrane structures under wind loading, and to generate the necessary data (visualised in charts) for more accurate and safe wind load calculations on these structures.

1.4 Methodology

This master thesis will expound the performed experimental wind tunnel analysis on the pressure coefficient distribution for hyperbolic membrane canopy structures, starting from the investigation of appropriate fabrication techniques for the test models. The thesis is composed of 3 main parts. The first part illustrates the current Eurocode procedure for determining the wind loads on common building geometries. The second part focuses on the research for appropriate modelling and testing procedures for open canopy structures. The third part displays the outcome of the experimental wind tunnel analysis. The experimental analysis assumes wind as a static load case with a negligible influence of geometric changes of the membrane shape on the measured pressure coefficients. The obtained pressure distributions on the considered membrane surfaces will be processed, evaluated and compared to the conclusions of some earlier experimental studies. The presented research could form a basis for the further investigation of more accurate safety factors and weighing factors for wind loading in different load combinations, because the current safety and weighing factors are defined by expertise without a statistical base and could be much too conservative. The experimentally obtained results and conclusions from the wind tunnel analysis will be visualised in charts that could be used for calculating wind loads on lightweight structures, and could form a fundamental basis for a Eurocode part on the design of membrane structures.

1.5 Design

Parallel to the research of this master thesis, a master proof design has to be made in line with the presented research. The design involves an Outdoor-Serpentine Theatre at the Provincial Recreation Park 'De Schorre' in Boom, Belgium (Figure 10). This recreation park is a former clay pit, which is taken back by nature. The industrial history of this site is still tangibly present in the typology of the landscape and the remnants of the industrial activity. The site is characterised by steep slopes of the former clay pits and artefacts such as an old clay excavator and the ruins of a former brickyard. The park is committed to the experience of '*culture in nature*', which is already apparent by annually organized events such as Tomorrowland, Mano Mundo, Xtreme Xperience, et cetera. From this point of view an outdoor theatre will form a qualitative extension to the present facilities and will contribute to the experience of '*culture in nature*' deeper in the park. Moreover, the steep slopes of the former clay pits lend themselves perfectly for seating stands of theatres.

The design comprises a total of two outdoor theatres and a bridging hiking track. The hiking track focuses on the changing experience of the nature by providing different approaches and various perspectives on the surrounding landscape. Within this dynamic context, the two theatres form a resting point where the natural landscape could be perceived peacefully. Both theatres are covered with tensile membrane roofs, sheltering the stands and stages from the natural elements. Membranes could be added, moved or removed depending on the specific requirements of the performances or the seasonal changes of the natural elements. Both theatres blend with their surrounding on a unique way. The small theatre has a rather dense structural grid and has a cosy and an intimate character, while the large theatre is more open and suits mid to large-scale performances. Next to the cultural performances, both theatres could be used as picnic areas, exhibition spaces or resting places to explore nature. For the elaborated discussion of the design is referred to the Design Portfolio.

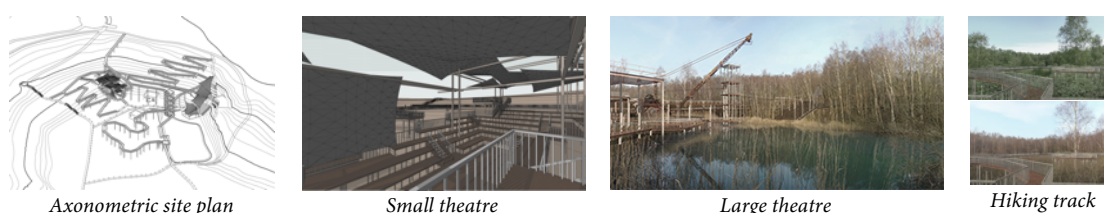


Figure 10: Outdoor-Serpentine Theatre at the Provincial Recreation Park 'De Schorre'

2

Wind Actions

2.1 Wind

Preliminary, a passage from the first book of the fifteen-piece Latin poetry “*Methamorphoses*” by the hand of Roman poet Publius Ovidius Naso, where he wrote about the wind in a passage on the creation of the world.

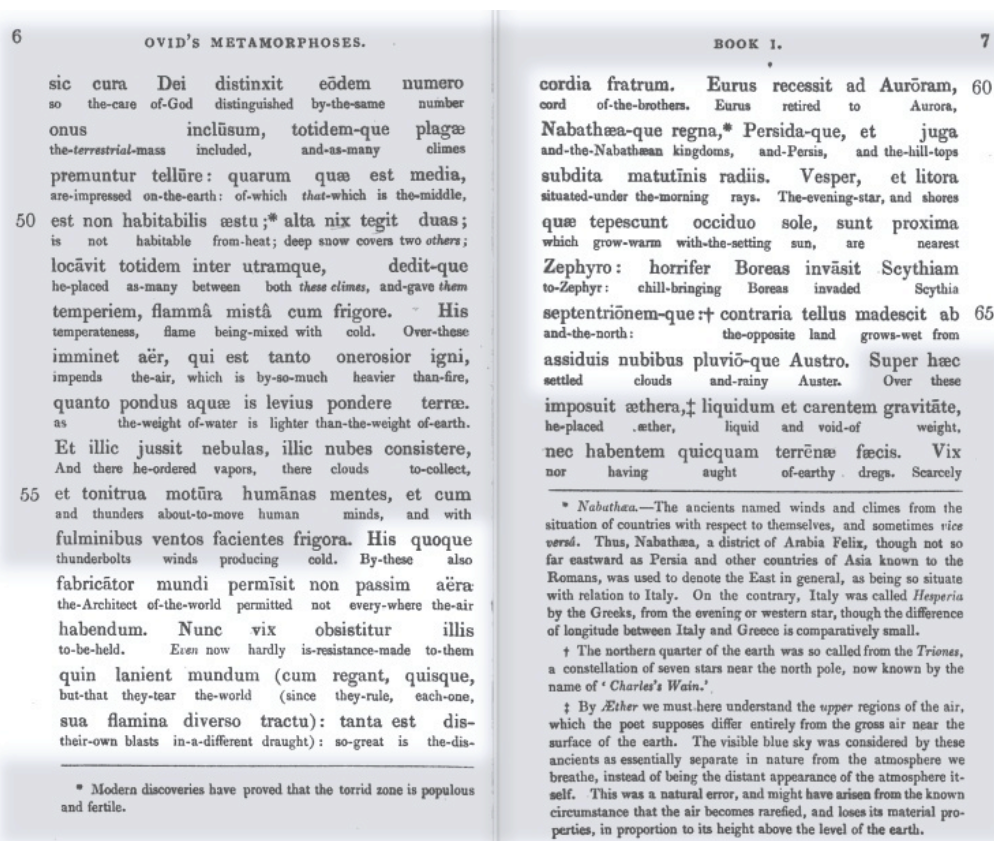


Figure 11: *Methamorphoses I* - P. Ovid, verse lines 56-66 - [37]

The architect of the world made the air move. Not in one direction, but by four main winds. These four winds or brothers, with their own blasts in a different direction, rule the world and sow damage while they quarrel. Eurus, the East Wind, blows from the countries where the hilltops light under the morning rays bringing warmth and rain; Zephyrus, the gentle West Wind, blows from the evening stars and the countries where the beach warms in the setting sun initiating light spring and early summer; Boreas, the rough and cold North Wind, invades from the cold northern latitudes bringing winter; and Auster, the warm South Wind, settles dark clouds, rain and storm in late summer and autumn. (*Methamorphoses I*, 57-66)

These four main winds are established with four sub winds to complete a total of eight winds in Greek mythology, and were taken in Roman mythology. Even nowadays these main and minor wind directions and their corresponding names are still retained.

Wind is the natural movement of air from the atmosphere that results from a complex interplay of global and local parameters such as differential earth heating, earth rotation, sun movement, seasons, constitution of continents and oceans, terrain roughness, orography, et cetera (Figure 12). The global movement of air is a direct result of the horizontal pressure differences caused by differential heating of the earth between the warm equator and the cold poles. The position of the sun and the curvature of the earth’s surfaces cause a more incident sunlight absorption in the equatorial areas compared to the dispersed sunlight absorption in the polar areas. The resulting temperature difference forms the basis of the three-cell atmospheric convection model that describes the typical wind flows around the globe by Hadley cells between the equator and the 30th latitude; Ferrel cells between the 30th and the 60th latitude; and Polar cells between the 60th latitude and the pole. The Hadley and Polar cells are temperature driven, and together induce the interstitial Ferrel cells. Warm air that rises creates low-pressure zones near earth’s surface and high-pressure zones in the higher atmosphere, while cool air that falls creates zones of low-pressure in the higher atmosphere and zones of high-pressure near the earth’s surface. The resulting horizontal pressure differences at the earth’s surface are the driving force of air movement, flowing from zones with a higher pressure to zones with a lower pressure in accordance with the prevailing pressure gradient resulting in north and south oriented winds. In addition, these north and south oriented winds are deflected by the earth’s rotation. This phenomenon (coriolis effect) causes the winds on the northern hemisphere to deflect to the right and on the southern hemisphere to the left (both seen along the wind direction), resulting in northeaster and southwester winds on the northern hemisphere and northwester and southeaster winds on the southern hemisphere. Finally, one should mark that the convection cells will shift with a particular lag in accordance with the latitudinal movements of the sun, which is also linked to the different seasons. Beside wind is also strongly affected by the inertia forces at the earth’s surface.

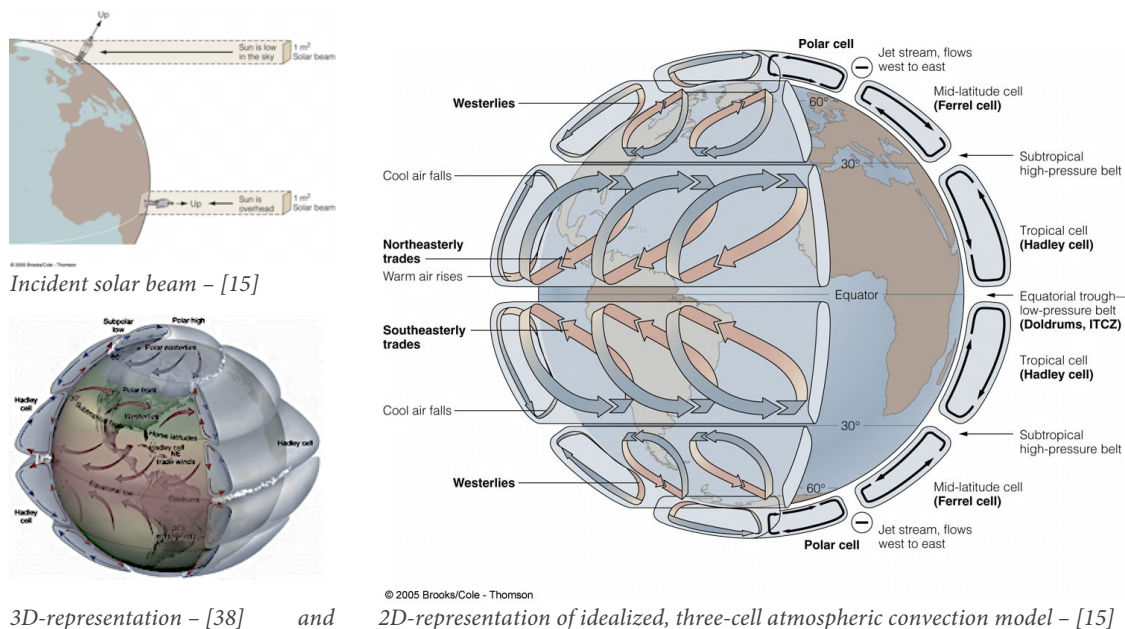


Figure 12: Theory behind origin of wind currents – [15] [38]

Wind currents result from horizontal pressure differences caused by differential heating of the earth. The temperature difference forms the basis of the three-cell atmospheric convection model. The Hadley and Polar cells are temperature driven, and together induce the interstitial Ferrel cells. The induced north and south winds are deflected by the earth’s rotation (coriolis effect).

Wind engineering investigates the effect of wind in both, the natural and the built environment in terms of wind climate, wind impact, wind comfort, wind energy, et cetera. The significance is essential for the analysis and the design of the built environment in the field of structural engineering. Especially where wind will be the dominant load in the structural design process, ranging from buildings (low- and high-rise), to bridges (suspension and cable stayed), to chimneys, electricity towers and so on.

Often, wind is described in reference to the scale of Beaufort (Figure 13), which was introduced in 1838. The British Navy used this scale as a technique to estimate the speed of winds at sea by interpreting the water surface or the sails of the ship. This already shows the significant affection of membrane structures by the interacting wind. Later on the empirical Beaufort scale and its classification of thirteen wind strengths, ranging from calm winds to hurricanes, has been updated for use on land. Nowadays wind-measuring devices have been developed, allowing very accurate determination of the actual wind speed. For several decennia the wind speeds have been recorded at various meteorological stations in different nations. These recorded wind data will allow describing the wind by a mathematical model, i.e. a logarithmic or power law wind speed profile in function of the height above the ground and several location specific boundary conditions. Consequently a statistic wind model will be used during the structural design process of buildings, in order to model the wind actions that could load a structure within a certain annual probability of exceedance. In addition, unusual and complex structures or boundary conditions will require numerical modelling by Computer Fluid Dynamics techniques or experimental boundary layer wind tunnel testing.

Beaufort number	Wind speed				Mean wind speed (ft / kmh / mph)	Description	Wave height		Sea conditions	Land conditions	
	kt	km/h	mph	m/s			m	ft			
0	0	0	0	0	0-0.2	0 / 0 / 0	Calm	0	0	Flat.	Calm. Smoke rises vertically.
1	1-3	1-6	1-3	0.3-1.5	0.2 / 0.4 / 2	Light air	0.1	0.33	Ripples without crests.	Wind motion visible in smoke.	
2	4-6	7-11	4-7	1.6-3.3	0.5 / 0.9 / 6	Light breeze	0.2	0.66	Small wavelets. Crests of glassy appearance, not breaking.	Wind felt on exposed skin. Leaves rustle.	
3	7-10	12-19	8-12	3.4-5.4	9 / 17 / 11	Gentle breeze	0.6	2	Large wavelets. Crests begin to break; scattered whitecaps.	Leaves and smaller twigs in constant motion.	
4	11-16	20-29	13-18	5.5-7.9	13 / 24 / 15	Moderate breeze	1	3.3	Small waves.	Dust and loose paper raised. Small branches begin to move.	
5	17-21	30-39	19-24	8.0-10.7	19 / 35 / 22	Fresh breeze	2	6.6	Moderate (1.2 m) longer waves. Some foam and spray.	Smaller trees sway.	
6	22-27	40-50	25-31	10.8-13.8	24 / 44 / 27	Strong breeze	3	9.9	Large waves with foam crests and some spray.	Large branches in motion. Whistling heard in overhead wires. Umbrella use becomes difficult.	
7	28-33	51-62	32-38	13.9-17.1	30 / 56 / 35	Near gale	4	13.1	Sea heaps up and foam begins to streak.	Whole trees in motion. Effort to walk against the wind.	
8	34-40	63-75	39-46	17.2-20.7	37 / 68 / 42	Gale	5.5	18	Moderately high waves with breaking crests forming spindrift. Streaks of foam.	Twigs broken from trees. Cars veer on road.	
9	41-47	76-87	47-54	20.8-24.4	44 / 81 / 50	Strong gale	7	23	High waves (2.75 m) with dense foam. Wave crests start to roll over. Considerable spray.	Light structure damage.	
10	48-55	88-102	55-63	24.5-28.4	52 / 96 / 60	Storm	9	29.5	Very high waves. The sea surface is white and there is considerable tumbling. Visibility is reduced.	Trees uprooted. Considerable structural damage.	
11	56-63	103-117	64-72	28.5-32.6	60 / 111 / 69	Violent storm	11.5	37.7	Exceptionally high waves.	Widespread structural damage.	
12	>63	>117	>72	>32.7	N/A	Hurricane	14+	46+	Huge waves. Air filled with foam and spray. Sea completely white with driving spray. Visibility very greatly reduced.	Massive and widespread damage to structures.	

Figure 13: Beaufort Scale –[59]

The Beaufort scale was introduced in 1838 and used by the British Navy to estimate the speed of winds at sea by interpreting the water surface or the sails of the ship. This empirical wind scale has a classification of thirteen wind strengths.

2.2 Eurocodes

The Eurocodes are a set of harmonized technical rules developed by the European Committee for Standardisation (CEN), that provide a general directive for the structural design of all construction works in terms of mechanical strength, stability and safety in concordance with the European Law. These European Norms replaced the existing national building codes of all European Union member states and are complemented by a national annex, containing national parameters, as is the case for wind loads.

The Eurocodes are generated as a set of separate *European Standards*, each composed of a number of parts. By 2002, the European Committee for Standardisation has developed and published ten Eurocode sections (EN1990 – 1999), with a total of 58 EN Eurocode parts.

Eurocode 0	“Basis of structural design”	EN 1990
Eurocode 1	“Actions on structures”	EN 1991
Eurocode 2	“Design of concrete structures”	EN 1992
Eurocode 3	“Design of steel structures”	EN 1993
Eurocode 4	“Design of composite steel and concrete structures”	EN 1994
Eurocode 5	“Design of timber structures”	EN 1995
Eurocode 6	“Design of masonry structures”	EN 1996
Eurocode 7	“Geotechnical design”	EN 1997
Eurocode 8	“Design of structures for earthquake resistance”	EN 1998
Eurocode 9	“Design of aluminium structures”	EN 1999

The Eurocodes focus mainly on the traditional, more conventional construction methods in concrete, steel and timber, but do not cover unusual forms of construction. From this perspective it would be recommended to extend the Eurocodes with an additional section for membrane structures. These kinds of structures increased popularity during the last decennia and are becoming more and more widely used.

EN 1991 Eurocode 1: ‘*Actions on structures*’ enucleates a comprehensive notice on all the actions and their corresponding calculation values that should be considered during the structural design calculations of a particular construction. This European Norm is constituted of four parts: ‘*General actions*’, ‘*Traffic loads on bridges*’, ‘*Actions induced by cranes and machinery*’ and ‘*Silos and tanks*’. The first part, ‘*General Actions*’, on its turn is subdivided into seven sub-parts that cover the variety of actions that should be considered during the structural design, ranging from densities over self-weight to imposed loads, actions due to fire, snow, wind and temperature differences.

EN 1991-1-1:2002	“General actions - Densities, self-weight, imposed loads for buildings”
EN 1991-1-2:2002	“General actions - Actions on structures exposed to fire”
EN 1991-1-3:2003	“General actions - Snow loads”
EN 1991-1-4:2005	“General actions - Wind actions”
EN 1991-1-5:2003	“General actions - Thermal actions”
EN 1991-1-6:2005	“General actions - Actions during execution”
EN 1991-1-7:2006	“General actions - Accidental actions”
EN 1991-2:2003	“Traffic loads on bridges”
EN 1991-3:2006	“Actions induced by cranes and machinery”
EN 1991-4: 2006	“Silos and tanks”

Depending on the nature of the structure EN 1991 has to be used in conjunction with EN 1992 to EN 1999 for the structural design. So it will be within this framework of EN 1991-1-4:2005: ‘*General actions – Wind actions*’ that the wind load characterisation for some typical membrane structures has to be investigated.



© 2005 CEN

EUROPEAN COMMITTEE FOR STANDARDIZATION
COMITÉ EUROPÉEN DE NORMALISATION
EUROPÄISCHES KOMITEE FÜR NORMUNG

2.2.1 Eurocode NBN EN 1991-1-4:2005

Eurocode 1: *Actions on structures - Part 1-4: General actions - Wind actions* [8] provides a general directive on predicting the characteristic natural wind actions that interact on a land-based structures with a height up to 200 m. The guidance is based on step-by-step modeling of the wind loads that will act on the components, surfaces and sub-surfaces of the considered structure. Through the calculation process the National Annex is often referred to, giving country specific values to model the wind actions that are function of the geographical and meteorological aspects of the location, such as wind climate, the terrain roughness and orography. In addition wind tunnel measurements and numerical methods such as Computational Fluid Dynamics can be used for specific information on unconventional design methods and situations.

In this section, the key concepts for the basic wind design as illustrated in the Eurocode will be introduced according to the chronological calculation steps and evaluated for membrane canopy structures. For a more elaborated overview including the structural background and the formulas is referred to Appendix A.

2.2.2 Modelling of wind actions

During the structural design process, the relevant wind actions have to be determined for each design situation in order to dimension the structure. Besides, one should also consider the different construction states and variable actions such as snow, ice, rain and service loads, which could modify the effects of the wind acting on the structure. Furthermore, the structure has to be checked on potential fatigue effects that may be initiated by the turbulent wind actions.

Wind is a fluctuating flow of air molecules, induced by the imbalance of forces acting on the air molecules. Consequently wind will interact with any object that influences its free stream flow by molecule-collisions between both interacting media. These collisions go along with energy transmissions, represented by forces or pressures on the separation faces. The amount of energy that is transmitted depends strongly on the collision orientation and consequently on the orientation of the separation faces, and thus in fact the shape and aerodynamic parameters of the object. In addition one should also consider the response of the structure itself, depending on its size, shape and dynamic properties. In the case of lightweight flexible membrane structures the aero-elastic response has to be evaluated. Flexible structures will deflect significant under wind loading causing changes in their aerodynamic properties. Modeling the wind loads that act on a structure starts with representing the fluctuating nature of wind by static values that cover, according to the European law with an annual probability of 98%, the extreme effects of turbulent wind for a return period of 50 years. Briefly outlined this procedure of representing the stochastic nature of wind loads (based on assumptions of wind profile, wind direction and wind strength) starts from the basic wind velocity, which is listed in the National Annex. Then, the mean wind velocity is calculated, followed by the peak velocity pressure. Finally, the associated wind pressures or forces acting on the corresponding surfaces are corrected by the aerodynamic pressure or force coefficients to take into account the aerodynamics of the structure.

2.2.3 Wind interaction

As mentioned earlier, the wind interacts with any object that influences or disturbs the free wind flow. Consequently every building, bridge or structure that is placed in open air will be loaded by the wind. The amount of kinetic energy that is transferred from the wind flow to the structure depends on aerodynamic parameters of the object. The associated wind pressures or forces acting on the structure are corrected by pressure or force coefficients taking into account the aerodynamics of the structure. The net wind pressure acting on an object is calculated as the vector summation of the simultaneous wind pressures acting on the different element faces. For the main building components, i.e. walls and roofs and other two dimensional plate shaped elements, the resulting wind pressure is simplified to the summation of the pressures acting on its opposing faces. From this point of view one should note that roof structures are loaded differently for canopies or enclosed buildings. An open canopy roof is directly loaded by the wind acting on the upper and lower face of the structure, while a roof of an enclosed building is directly loaded on its outer face and indirectly on its inner face. Consequently, canopy roofs are calculated directly by net wind pressures, while roofs of enclosed buildings are calculated by vector summation of the external and internal pressures. During the calculations, one has to carefully consider the direction of the pressure. Notwithstanding the fact that pressure is a scalar and therefore in essence has no direction, the orientation dependency is granted for the convenience of the interpretation. Pressure directed towards the surface is taken as positive, while suction directed away from the surface as negative.

2.2.4 Pressure coefficients

The last step in the modeling process of the wind actions is to determine appropriate aerodynamic coefficients for each structure. These aerodynamic parameters are defined in the Eurocode by pressure coefficient distributions, giving the effect of the wind per unit area for some common structures and building configurations. Most coefficients in EN 1991-1-4 are based on wind tunnel studies in a free flow field and are listed in tables for specified wind directions. All pressure distributions are given for standard rectangular ground plans and are based on geometrical proportions. In the case of unconventional structures sufficient safe assumptions have to be made while defining the pressure coefficients based on the provided data in the norm, or otherwise additional wind investigation is required. The discussion below is limited to the roof structures that will be tested during wind tunnel experiments in order to evaluate the fabrication techniques of the models, validate the accuracy and precision of the measurements and to create a reference testing field for the following research on membrane roof structures. The reference testing will be done on a flat and duo-pitch roof as part of an enclosed building envelope on the one hand and as fully open canopy structures without blockage on the other hand, resulting in a total of four test cases. This testing procedure will allow studying the presence of enclosing envelope walls on the external pressure coefficient distribution over the considered roof structure, where the Eurocode provides only internal and external pressure coefficients for an enclosed building situation and net pressure coefficients for a canopy structure and not the pressure coefficient distribution over the external face of the canopy roof itself. The internal and external pressure coefficients give respectively the effect of the wind on the internal and external building faces, while the net pressure coefficients account for the total effect of the wind on canopy surfaces. Besides, the Eurocode provides for each type of structure overall and local pressure coefficients, respectively for areas equal to or larger than 10 m^2 and smaller than 1 m^2 . It is observed that wind loads and corresponding pressure coefficients depend on the size of the loaded area. For surface areas between 1 m^2 and 10 m^2 a logarithmic interpolation is used (Figure 14). Nevertheless in most design cases the overall coefficients $c_{pe,10}$ are used for the overall load bearing calculation, while the local coefficients $c_{pe,1}$ are used to dimension small elements or fixings. The analysis below concentrates on the overall pressure coefficients, since the focus of this thesis lies on the general pressure distribution over the considered roof structure.

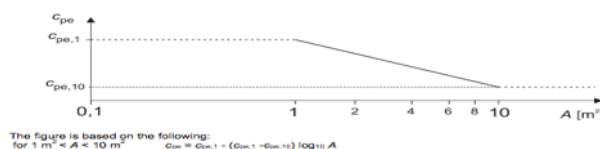


Figure 14: Logarithmic Interpolation overall and local pressure coefficients – [8]

For the wind tunnel experiments, a total of three roof structures were modeled: a flat roof structure with sharp edges and an inclination of approximately 0° (section 3.3.1), a duo-pitch roof structure with a positive pitch angle of 30° on both sides (section 3.3.2) and a hypar roof structure with a shape parameter of 11,3 (section 3.3.3). The roof structures have been equipped with removable walls allowing each roof to be tested as part of a building envelope and as a canopy itself.

2.2.5 Building roofs

A building roof is defined as the roof of a structure with permanent walls. The external pressure coefficients that are presented in EN 1991-1-4:2005 represent the maximal pressures for the considered orthogonal directions and cover the most unfavourable values within a range of 45° either side of the relevant orthogonal direction. As earlier mentioned shall any building interact with, and disturb the flow profile of wind. The way and the degree of distortion are mainly function of the aerodynamics or shape parameters of the considered building. In general is the undisturbed airflow upwind the building forced over and around the building envelope, resulting in pressure or suction areas acting on the building faces. Pressure or overpressure refers to air pressures above barometric pressure levels and is indicated by a positive sign, while suction or underpressure refers to air pressures below barometric pressure levels and is indicated by a negative sign. Intuitively it is clear to see that front faces blocking the airflow will be loaded by positive pressure, while rear faces in the generated wake zones tend to be loaded by suction. In addition it is observed that the wind flow accelerates around buildings edges, causing locally decreasing pressures near these face edges. This phenomenon is known as the Venturi effect, stating that a narrowing conic shaft induces acceleration of the wind flow, while a widening conic shaft reduces the wind speed. The increased wind speed will consequently increase the suction component, causing overpressures to decrease and underpressures to increase. Finally, roofs tend to be loaded mainly by suction, but the actual pressure distribution depends largely on the roof shape. The pressure distributions for a flat, a duo-pitch and a hypar roof, all part of an enclosed building envelope, are listed and discussed below.

2.2.5.1 Flat roof

- Flat roofs are defined as having a slope ranging from $-5^\circ < \alpha < 5^\circ$
- The reference height z_e should be taken as h ; see Figure 15
- The roof should be divided into zones; see Figure 15
- The pressure coefficients for each zone are listed for orthogonal directions; see Table 1

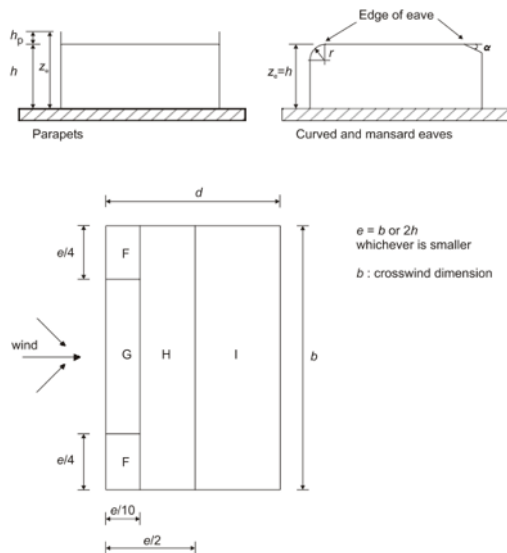


Figure 15: Geometrical specifications of flat roofs – [8]

Roof type	Zone								
	F		G		H		I		
	$C_{pe,10}$	$C_{pe,1}$	$C_{pe,10}$	$C_{pe,1}$	$C_{pe,10}$	$C_{pe,1}$	$C_{pe,10}$	$C_{pe,1}$	
Sharp eaves	-1,8	-2,5	-1,2	-2,0	-0,7	-1,2	+0,2 -0,2		
With Parapets	$h_p/h=0,025$	-1,6	-2,2	-1,1	-1,8	-0,7	-1,2	+0,2 -0,2	
	$h_p/h=0,05$	-1,4	-2,0	-0,9	-1,6	-0,7	-1,2	+0,2 -0,2	
	$h_p/h=0,10$	-1,2	-1,8	-0,8	-1,4	-0,7	-1,2	+0,2 -0,2	
Curved Eaves	$r/h = 0,05$	-1,0	-1,5	-1,2	-1,8	-0,4		+0,2 -0,2	
	$r/h = 0,10$	-0,7	-1,2	-0,8	-1,4	-0,3		+0,2 -0,2	
	$r/h = 0,20$	-0,5	-0,8	-0,5	-0,8	-0,3		+0,2 -0,2	
Mansard Eaves	$\alpha = 30^\circ$	-1,0	-1,5	-1,0	-1,5	-0,3		+0,2 -0,2	
	$\alpha = 45^\circ$	-1,2	-1,8	-1,3	-1,9	-0,4		+0,2 -0,2	
	$\alpha = 60^\circ$	-1,3	-1,9	-1,3	-1,9	-0,5		+0,2 -0,2	

NOTE 1 For roofs with parapets or curved eaves, linear interpolation may be used for intermediate values of h_p/h and r/h .

NOTE 2 For roofs with mansard eaves, linear interpolation between $\alpha = 30^\circ, 45^\circ$ and $\alpha = 60^\circ$ may be used. For $\alpha > 60^\circ$ linear interpolation between the values for $\alpha = 60^\circ$ and the values for flat roofs with sharp eaves may be used.

NOTE 3 In Zone I, where positive and negative values are given, both values shall be considered.

NOTE 4 For the mansard eave itself, the external pressure coefficients are given in Table 7.4 "External pressure coefficients for duopitch roofs: wind direction 0° ". Zone F and G, depending on the pitch angle of the mansard eave.

NOTE 5 For the curved eave itself, the external pressure coefficients are given by linear interpolation along the curve, between values on the wall and on the roof.

Table 1: External pressure coefficients for flat roofs – [8]

Buildings with a flat roof affect the wind profile to a limited extent, causing undisturbed wind passing above the roof. The rather high wind velocity of the air flowing over the horizontal roof generates mainly suction over the entire roof area. Upwind edge and corner areas are most heavily loaded by suction what could be contributed to the acceleration of wind flow around the windward building edges. For skew winds, extreme levels of suction may occur locally at the upwind corner. Consequently, suction is largest at the upwind areas and decreases downwind due to the reduced wind speed by the induced vortices, the roughness, and the viscosity and friction forces at the roof face. The generation of this kind of boundary layer above the roof in combination with a slightly positive inclination could even cause the downwind areas to be loaded with very low positive pressure.

Finally, one should consider the type of roof eaves as these have an undeniable impact on the pressure distribution. It is clear to see that the presence of parapets, mansard eaves, curved eaves or simply the aerodynamics of the building mainly influences the pressure coefficients at the windward areas of the roof. Sharp eaves will generally induce highest suction at the upwind roof edges. This suction results from the low-pressure area that is induced between the roof face and the accelerated wind that separates at the sharp roof edge. The size of wake will influence the pressure coefficient distribution. Parapets will redirect the flow higher over the roof compared to sharp edges, resulting in a larger separation of the redirected wind flow and therefore lower suction effects. The higher the parapet, the lower the suction. The improved aerodynamics of mansard eaves and curved edges will result in lowest suction. The larger the radius of curvature of the edge, the smoother the transition between wall and roof, and thus the smaller the acceleration and separation of wind and the lower the suction. The lower the degree of mansard inclination, the better the aerodynamics, and thus the smaller the acceleration and separation of wind and the lower the suction. For the corner zones this aerodynamic interaction is more complex, but generally similar conclusions can be drawn.

2.2.5.2 Monopitch roof

- Monopitch roofs are defined as having a slope ranging from $5^\circ < \alpha < 75^\circ$
- The reference height z_e should be taken as h ; see Figure 16
- The roof should be divided into zones; see Figure 16
- The pressure coefficients for each zone are listed for orthogonal directions; see Table 2

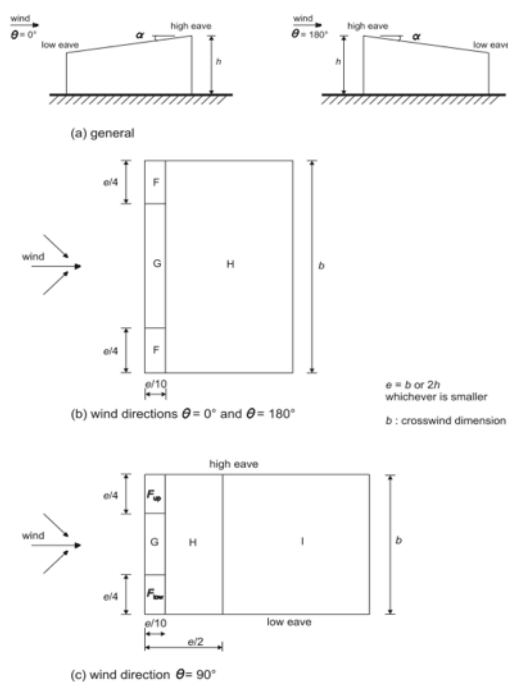


Figure 16: Geometrical specifications of monopitch roofs – [8]

Pitch Angle α	Zone for wind direction $\theta = 0^\circ$					Zone for wind direction $\theta = 180^\circ$						
	F		G		H	F		G		H		
	$C_{pe,10}$	$C_{pe,1}$	$C_{pe,10}$	$C_{pe,1}$	$C_{pe,1}$	$C_{pe,10}$	$C_{pe,1}$	$C_{pe,10}$	$C_{pe,1}$	$C_{pe,1}$		
5°	-1,7	-2,5	-1,2	-2,0	-0,6	-1,2	-2,3	-2,5	-1,3	-2,0	-0,8	-1,2
	+0,0		+0,0		+0,0	-2,3		-2,5		-1,3	-2,0	
15°	-0,9	-2,0	-0,8	-1,5	-0,3		-2,5	-2,8	-1,3	-2,0	-0,9	-1,2
	+0,2		+0,2		+0,2	-2,5		-2,8		-1,3	-2,0	
30°	-0,5	-1,5	-0,5	-1,5	-0,2		-1,1	-2,3	-0,8	-1,5	-0,8	
	+0,7		+0,7		+0,4	-1,1		-2,3		-0,8	-1,5	
45°	-0,0	-0,0	-0,0	-0,0	-0,0		-0,6	-1,3	-0,5		-0,7	
	+0,7		+0,7		+0,6	-0,6		-1,3		-0,5		-0,7
60°	+0,7	+0,7	+0,7	+0,7	+0,7		-0,5	-1,0	-0,5		-0,5	
75°	+0,8	+0,8	+0,8	+0,8	+0,8		-0,5	-1,0	-0,5		-0,5	

Pitch Angle α	Zone for wind direction $\theta = 90^\circ$									
	F_{up}		F_{low}		G		H		I	
	$C_{pe,10}$	$C_{pe,1}$	$C_{pe,10}$	$C_{pe,1}$	$C_{pe,10}$	$C_{pe,1}$	$C_{pe,10}$	$C_{pe,1}$	$C_{pe,10}$	$C_{pe,1}$
5°	-2,1	-2,6	-2,1	-2,4	-1,8	-2,0	-0,6	-1,2	-0,5	
15°	-2,4	-2,9	-1,6	-2,4	-1,9	-2,5	-0,8	-1,2	-0,7	-1,2
30°	-2,1	-2,9	-1,3	-2,0	-1,5	-2,0	-1,0	-1,3	-0,8	-1,2
45°	-1,5	-2,4	-1,3	-2,0	-1,4	-2,0	-1,0	-1,3	-0,9	-1,2
60°	-1,2	-2,0	-1,2	-2,0	-1,2	-2,0	-1,0	-1,3	-0,7	-1,2
75°	-1,2	-2,0	-1,2	-2,0	-1,2	-2,0	-1,0	-1,3	-0,5	

NOTE 1 At $\theta = 0^\circ$ (see table a)) the pressure changes rapidly between positive and negative values around a pitch angle of $\alpha = +5^\circ$ to $+45^\circ$, so both positive and negative values are given. For those roofs, two cases should be considered: one with all positive values, and one with all negative values. No mixing of positive and negative values is allowed on the same face.

NOTE 2 Linear interpolation for intermediate pitch angles may be used between values of the same sign. The values equal to 0.0 are given for interpolation purposes

Table 2: External pressure coefficients for monopitch roofs – [8]

For monopitch roofs, three cases have to be considered. The low eave under attack, the high eave under attack and the low and high eave parallel to the wind direction. For all three orientations rather similar conclusions could be drawn as for flat roofs. A monopitch roof with an inclination of 5° corresponds closely to a flat roof, loaded mainly in suction with very similar pressure coefficients. For all orientations, upwind roof corners will be loaded most heavily with decreasing values for the downwind areas.

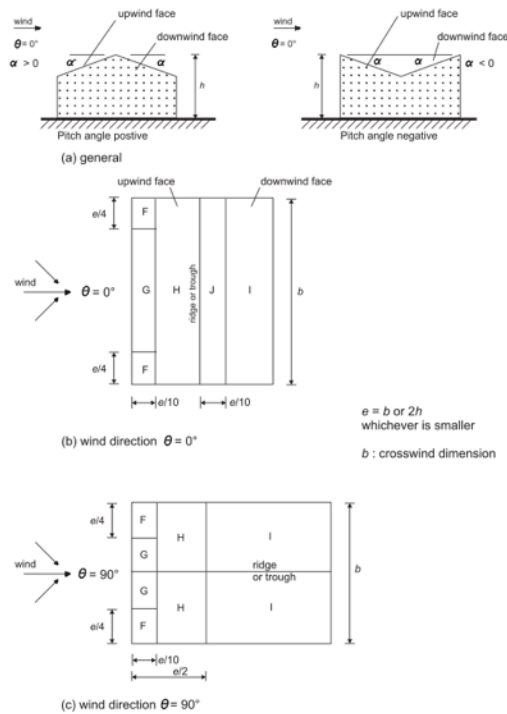
When the low eave of a monopitch roof is under attack, the roof is intuitively loaded by positive pressure acting on the roof face with increasing values for steeper roof inclinations. However, for inclinations less than 15° the roof is mainly loaded by suction as result of the rather high wind speeds of the air flowing over the aerodynamic roof, while for inclinations between 15° and 30° suction as well as pressure may occur.

For the high eave of a monopitch roof under attack, the entire roof is always loaded by suction as a direct result of the separation of flow at the wake of the structure. For this orientation an increasing inclination results in decreasing suction values, caused by the larger distance of the separation point at the wake of the roof.

Finally, the parallel wind direction causes mainly suction over the entire roof. For this parallel orientation an increasing roof inclination affects the pressure distribution rather complex, with decreasing C_{pe} -values at the upwind edge, increasing C_{pe} -values at the upwind areas close to this edge, and increasing C_{pe} -values followed by a decrease for the downwind areas with the transfer point at inclination of approximately 45° . This complex interaction is caused by the interplay of shape parameters, viscosity and friction forces inducing local accumulation and separation in the wind profile by acceleration and wake.

2.2.5.3 Duo-pitch roof

- Duo-pitch roofs are defined as having a slope ranging from $-45^\circ < \alpha < 75^\circ$
- The reference height z_e should be taken as h ; see Figure 17
- The roof should be divided into zones; see Figure 17
- The pressure coefficients for each zone are listed for orthogonal directions; see Table 3



Pitch Angle α	Zone for wind direction $\theta = 0^\circ$									
	F		G		H		I		J	
	$C_{pe,10}$	$C_{pe,1}$	$C_{pe,10}$	$C_{pe,1}$	$C_{pe,10}$	$C_{pe,1}$	$C_{pe,10}$	$C_{pe,1}$	$C_{pe,10}$	$C_{pe,1}$
-45°	-0,6		-0,6		-0,8		-0,7		-1,0	-1,5
-30°	-1,1	-2,0	-0,8	-1,5	-0,8		-0,6	-0,8	-0,8	-1,4
-15°	-2,5	-2,8	-1,3	-2,0	-0,9	-1,2	-0,5	-0,7	-0,7	-1,2
-5°	-2,3	-2,5	-1,2	-2,0	-0,8	-1,2	+0,2		+0,2	
5°	-1,7	-2,5	-1,2	-2,0	-0,6	-1,2	-0,6		+0,2	
	+0,0		+0,0		+0,0				-0,6	
15°	-0,9	-2,0	-0,8	-1,5	-0,3		-0,4	-1,0	-1,5	
	+0,2		+0,2		+0,2		+0,0	+0,0	+0,0	
30°	-0,5	-1,5	-0,5	-1,5	-0,2		-0,4		-0,5	
	+0,7		+0,7		+0,4		+0,4		+0,0	
45°	-0,0		-0,0		-0,0		-0,2		-0,3	
	+0,7		+0,7		+0,6		+0,0		+0,0	
60°	+0,7		+0,7		+0,7		-0,2		-0,3	
75°	+0,8		+0,8		+0,8		-0,2		-0,3	

NOTE 1 At $\theta = 0^\circ$ the pressure changes rapidly between positive and negative values on the windward face around a pitch angle of $\alpha = -5^\circ$ to $+45^\circ$, so both positive and negative values are given. For those roofs, four cases should be considered where the largest or smallest values of all areas F, G and H are combined with the largest or smallest values in areas I and J. No mixing of positive and negative values is allowed on the same face.

NOTE 2 Linear interpolation for intermediate pitch angles of the same sign may be used between values of the same sign. (Do not interpolate between $\alpha = +5^\circ$ and $\alpha = -5^\circ$, but use the data for flat roofs in 7.2.3). The values equal to 0,0 are given for interpolation purposes

Pitch angle α	Zone for wind direction $\theta = 90^\circ$							
	F		G		H		I	
	$C_{pe,10}$	$C_{pe,1}$	$C_{pe,10}$	$C_{pe,1}$	$C_{pe,10}$	$C_{pe,1}$	$C_{pe,10}$	$C_{pe,1}$
-45°	-1,4	-2,0	-1,2	-2,0	-1,0	-1,3	-0,9	-1,2
-30°	-1,5	-2,1	-1,2	-2,0	-1,0	-1,3	-0,9	-1,2
-15°	-1,9	-2,5	-1,2	-2,0	-0,8	-1,2	-0,8	-1,2
-5°	-1,8	-2,5	-1,2	-2,0	-0,7	-1,2	-0,6	-1,2
5°	-1,6	-2,2	-1,3	-2,0	-0,7	-1,2	-0,6	-1,2
15°	-1,3	-2,0	-1,3	-2,0	-0,6	-1,2	-0,5	-1,2
30°	-1,1	-1,5	-1,4	-2,0	-0,8	-1,2	-0,5	-1,2
45°	-1,1	-1,5	-1,4	-2,0	-0,9	-1,2	-0,5	-1,2
60°	-1,1	-1,5	-1,2	-2,0	-0,8	-1,0	-0,5	-1,2
75°	-1,1	-1,5	-1,2	-2,0	-0,8	-1,0	-0,5	-1,2

Figure 17: Geometrical specifications of duo-pitch roofs – [8]

Table 3: External pressure coefficients for duo-pitch roofs – [8]

For duo-pitch roofs, four cases have to be considered: two cases for positive pitch angles and two cases for negative pitch angles respectively with a ridge or trough, both for a wind direction perpendicular and parallel to the ridge or trough. Duo-pitch roofs can be seen as a combination of two intersecting monopitch roofs, with identical or different pitch angles. Consequently, for each pitch side similar conclusions could be drawn as for monopitch roofs.

For the perpendicular orientation, the pressure coefficient distributions for duo-pitch roofs and monopitch roofs have clear relations. For the windward pitch of a duo-pitch roof and for the corresponding monopitch roof rather identical pressure coefficient distributions and C_{pe} -values are presented, while for the leeward pitch larger variations are observed. The trough shaped roof is loaded entirely by suction, with decreasing C_{pe} -values downwind. The wake that is generated in the trough induces the highest suction on the leeward pitch near the centerline of the trough itself. The ridge shaped roof on the other hand is more complex and depending on the pitch inclinations. For an inclination larger than 30° the windward pitch will be loaded by positive pressure with increasing values for steeper roof inclinations, while the leeward pitch is loaded by suction. For pitched roofs with a slope of less than 15° suction affects the whole roof as result of the rather high wind speeds of the air flowing over the roof. Consequently, for inclinations between 15° and 30° suction as well as pressure may occur at the windward pitch. However, for all cases the ridge will be prone to considerable suction. The local acceleration of air flowing around the ridge and separating from the roof face results in permanent suction on the leeward pitch, induced by the generated wake.

For the parallel orientation, ridge- and trough shaped duo-pitch roofs are loaded entirely by suction, with decreasing values at downwind areas. The trough shaped roof, has rather identical pressure coefficient distributions to those of two intersecting monopitch roofs, except for the C_{pe} -values close to the windward edge that are lower because of the reduced wind speed in the trough itself. Besides, it is observed that these values are identical for all inclinations. The ridge shaped roof on the other hand, has slightly smaller C_{pe} -values over the entire pressure distribution compared to those of the corresponding monopitch roofs.

2.2.5.4 Hypar roof

For hypar roofs the Eurocode does not provide any information, which stipulates the need for investigation of these structures by wind tunnel experiments or numerical simulations. In specialised literature very limited information about the wind pressure distribution on these types of roof structures is available. The European Design Guide for Tensile Surface Structures solely presents the general pressure coefficient distribution for a specific hyperbolic roof with high and low corner points and a shape parameter of 4,7 (adopted and reproduced from Otto, F., Das Hängende Dach, 1954).

- Hypar roofs are defined by a shape parameter, being the ratio of the diagonal dimension to the vertical distance between the high and low corners
- The roof, should be divided into zones; see Figure 18
- The pressure coefficients for each zone are listed for orthogonal directions; see Table 4

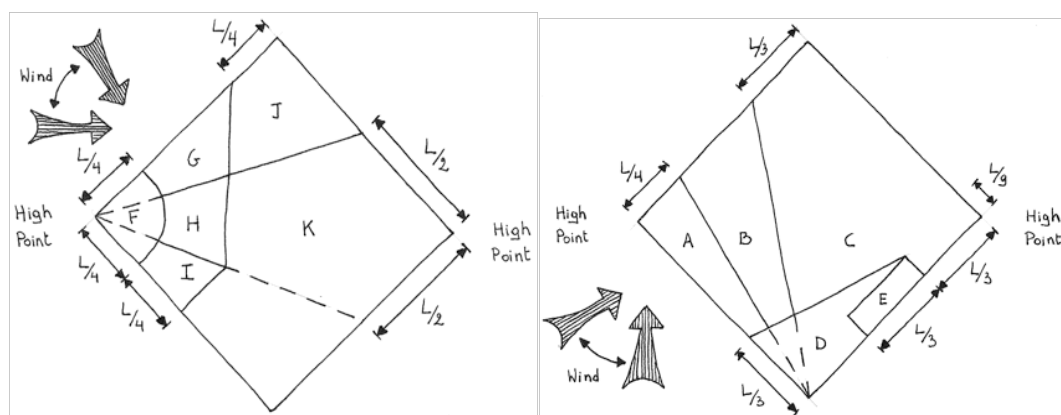


Figure 18: Geometrical specifications of a hypar roof with shape parameter of 4,7 – [47]

External Cp values	Zones										
	A	B	C	D	E	F	G	H	I	J	K
Positive	0	0	+0.3	+0.3	+0.3	0	0	+0.2	0	0	+0.2
Negative	-1.45	-0.9	-0.65	-0.70	-1.20	-1.80	-1.20	-0.9	-1.20	-0.65	-0.65

Table 4: External pressure coefficients for a hypar roof with shape parameter of 4,7 – [47]

For hypar or saddle shaped roofs with high and low corner points, two cases have to be considered: the low corner under attack and the high corner under attack. The aerodynamic character of this curved roof surfaces mainly causes suction over the entire roof. Intuitively higher suction values are expected for flatter hypar roofs. Small height difference between the high and low points leads to lower curvature and tends closer to a flat roof, having larger wind speeds of air flowing over the roof face. Large height differences on the other hand will reduce the wind speed by the smaller radii of curvature, allowing positive pressure to build up at the more vertical roof areas. Similar to all roof structures above does wind speed decreases downwind, resulting in lower C_{pe} -values for these areas.

When the low point of the hypar roof is under attack, most suction is generated at the inflection point close to the roof edge. For highly curved membranes small overpressure can be generated near the high point at the downwind area of the roof. The corresponding pressure coefficients for this orientation are most critical for the areas close to the low point under attack, but they are not judicial for membrane itself.

For the high point of the hypar roof under attack, most extreme suction coefficients are observed at areas close to this high point. Consequently, this critical orientation will be judicial for the dimensioning of the membrane itself. Besides, also for this orientation small overpressure can be generated near the high point located at the downwind area of the roof in case of sufficiently large curved membrane roofs.

2.2.6 Canopy roofs

A canopy roof is defined as the roof of a structure without permanent walls. Canopy roofs are loaded directly by the wind acting its upper and lower roof faces simultaneously (Figure 19), where building roofs are only directly loaded by wind acting on its outer face. The net pressure coefficients that are presented in EN 1991-1-4:2005 represent the maximal local pressures for all wind directions for a fully blocked or empty canopy. It is observed that these net pressures change rapidly between positive and negative values, causing the canopy to be loaded respectively by downward acting pressure or upward lifting. Intuitively it is clear to see that for open canopies, wind will generate usually suction on the bottom face of the canopy, while the upper face can be loaded by pressure or suction depending on the aerodynamic character and the orientation of the considered canopy. The degree of blockage φ under a canopy roof is the ratio of the area of feasible obstructions under the canopy divided by the cross sectional area under the canopy, both areas normal to the wind direction; $\varphi = 0$ represents an empty canopy and $\varphi = 1$ represents the canopy fully blocked to the downwind eaves, what is not to be mistaken as a fully closed building. Intermediate values may be found by linear interpolation, while downwind the position of maximum blockage $c_{p,net}$ values for $\varphi = 0$ should be used. Finally, the considered canopy roof should be able to support all load cases and combinations as defined in the Eurocode, and one should consider the friction forces especially for the angles of attack parallel to the main canopy direction. Remark that the Eurocode provides general directive for canopies, without going into detail as for building roofs, where more detailed pressure coefficient distributions are given for orthogonal directions. Presumably these simplifications have been introduced to deal with to the complex interaction of the wind acting simultaneously on both roof surfaces, and by the fact that this type of roof structures is being applied less commonly. The pressure distributions for a monopitch and a duo-pitch canopy are listed and discussed below. Hypar canopies are not discussed as neither the Eurocode nor specialised literature provides any information about wind loads on hyperbolic paraboloid canopies, which stipulates the need for expertise and investigation of these structures by wind tunnel experiments or numerical simulations.

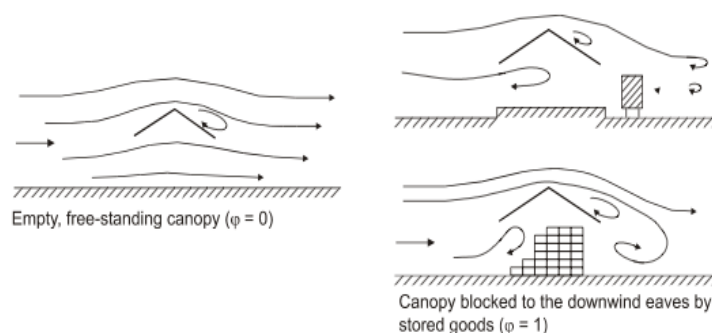
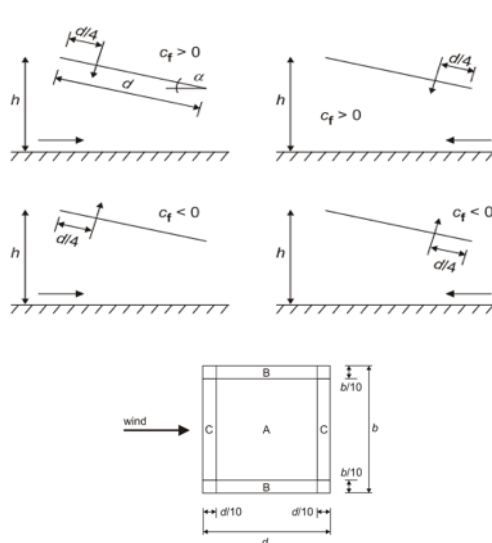


Figure 19: Airflow over and under canopy roofs – [8]

Canopy roofs are loaded directly by the wind acting its upper and lower roof faces simultaneously. The wind actions depend on the degree of blockage φ under a canopy roof. $\varphi = 0$ represents an empty canopy and $\varphi = 1$ represents the canopy fully blocked to the downwind eaves.

2.2.6.1 Monopitch canopy

- Monopitch canopy roofs are defined as having a slope ranging from $5^\circ < \alpha < 30^\circ$
- The reference height z_e should be taken as h ; see Figure 20
- The canopy roof should be divided into zones; see Figure 20
- The centre of pressure should be taken at $d/4$ from the windward edge; see Figure 20
- The net pressure coefficients for each zone are listed for $\varphi = 0$ and $\varphi = 1$; see Table 5



Roof angle α	Blockage φ	Overall Force Coefficients C_r	Zone A	Zone B	Zone C
0°	Maximum all φ	+ 0,2	+ 0,5	+ 1,8	+ 1,1
	Minimum $\varphi = 0$	- 0,5	- 0,6	- 1,3	- 1,4
	Minimum $\varphi = 1$	- 1,3	- 1,5	- 1,8	- 2,2
5°	Maximum all φ	+ 0,4	+ 0,8	+ 2,1	+ 1,3
	Minimum $\varphi = 0$	- 0,7	- 1,1	- 1,7	- 1,8
	Minimum $\varphi = 1$	- 1,4	- 1,6	- 2,2	- 2,5
10°	Maximum all φ	+ 0,5	+ 1,2	+ 2,4	+ 1,6
	Minimum $\varphi = 0$	- 0,9	- 1,5	- 2,0	- 2,1
	Minimum $\varphi = 1$	- 1,4	- 2,1	- 2,6	- 2,7
15°	Maximum all φ	+ 0,7	+ 1,4	+ 2,7	+ 1,8
	Minimum $\varphi = 0$	- 1,1	- 1,8	- 2,4	- 2,5
	Minimum $\varphi = 1$	- 1,4	- 1,6	- 2,9	- 3,0
20°	Maximum all φ	+ 0,8	+ 1,7	+ 2,9	+ 2,1
	Minimum $\varphi = 0$	- 1,3	- 2,2	- 2,8	- 2,9
	Minimum $\varphi = 1$	- 1,4	- 1,6	- 2,9	- 3,0
25°	Maximum all φ	+ 1,0	+ 2,0	+ 3,1	+ 2,3
	Minimum $\varphi = 0$	- 1,6	- 2,6	- 3,2	- 3,2
	Minimum $\varphi = 1$	- 1,4	- 1,5	- 2,5	- 2,8
30°	Maximum all φ	+ 1,2	+ 2,2	+ 3,2	+ 2,4
	Minimum $\varphi = 0$	- 1,8	- 3,0	- 3,8	- 3,6
	Minimum $\varphi = 1$	- 1,4	- 1,5	- 2,2	- 2,7

NOTE + values indicate a net downward acting wind action
- values represent a net upward acting wind action

Figure 20: Geometrical specifications of monopitch canopies – [8] Table 5: Net pressure coefficients for monopitch canopies – [8]

For monopitch canopy roofs, the Eurocode prescribes four load cases that have to be considered: two cases for the high eave under attack and two cases for low eave under attack, both for a net down acting and a net uplifting pressure. The case where the wind is parallel to the high and the low eave is not considered anymore, as it was the case for monopitch roofs. The net wind pressures acting on the canopy roof for this parallel orientation will be rather low, caused by the counteracting suction that is generated on upper and the lower face of the roof. For the remaining orientations similar conclusions could be drawn as for monopitch roofs, by considering the presence of varying wind pressure acting directly on the bottom face of the canopy, which is not the case for building roofs. A monopitch canopy with an inclination of 0° to 5° can be seen as a flat canopy roof loaded mainly by uplifting pressure with rather low C_p -values, as a result of the counteracting suction on both faces. However, downward acting net pressure can be induced as well, in case of pressure on the upper face in combination with suction on the lower face. Besides, it is observed that the edges are the most heavily loaded areas.

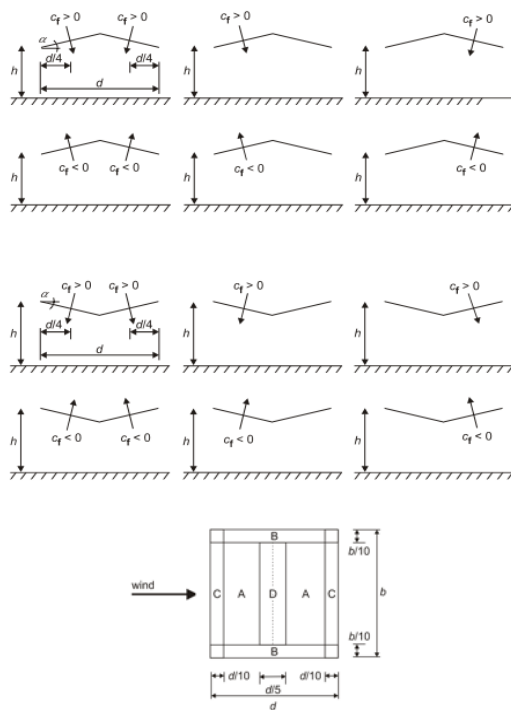
When the low eave of a monopitch canopy is under attack, the roof is intuitively loaded by downward acting net pressure with increasing values for steeper roof inclinations. However, the rather limited inclination of canopy roofs makes them vulnerable for uplifting net pressures as well. With the low eave under attack the lower face of the roof is always loaded by suction caused by the flow separation and generated wake at this face, while the upper face can be loaded by positive pressure or suction as result of the rather high wind speeds of the air flowing over the aerodynamic roof in analogy to monopitch roofs having a slope up to 30° . In addition, blockage under the canopy will give rise to positive pressure building up at the lower face of the roof.

For the high eave of a monopitch canopy under attack, the entire roof is intuitively loaded by uplifting net pressures with increasing values for steeper roof inclinations. However they are also vulnerable for rather limited downward acting net pressures as well. With the high eave under attack the upper face of the roof is always loaded by suction as a result of the flow separation and generated wake at this face, while the lower face can be loaded by positive pressure or suction caused by an interplay between inclination, blockage and the wind speeds of the air flowing under the aerodynamic roof.

Depending on the orientation and the inclination of the monopitch canopy roof, rather a fully open or a fully blocked canopy is loaded by highest uplifting net pressure upwind the location of blockage. For open canopies C_p -values increase with the inclination, while for fully blocked canopies C_p -values stay constant. Finally, for more detailed pressure distributions additional wind analysis is required.

2.2.6.2 Duo-pitch canopy

- Duo-pitch canopy roofs are defined as having a slope ranging from $-45^\circ < \alpha < 45^\circ$
- The reference height z_e should be taken as h ; see Figure 21
- The canopy roof should be divided into zones; see Figure 21
- The centre of pressure should be taken at the centre of each slope; see Figure 21
- A duo-pitch canopy should be able to support one pitch with the maximum or minimum load, the other pitch being unloaded; see Figure 21
- The net pressure coefficients for each zone are listed for $\varphi = 0$ and $\varphi = 1$; see Table 6



Roof angle α [°]	Blockage φ	Overall Force Coefficient c_f	Zone A	Zone B	Zone C	Zone D
-20	Maximum all φ	+0,7	+0,8	+1,6	+0,6	+1,7
	Minimum $\varphi = 0$	-0,7	-0,9	-1,3	-1,6	-0,6
	Minimum $\varphi = 1$	-1,3	-1,5	-2,4	-2,4	-0,6
-15	Maximum all φ	+0,5	+0,6	+1,5	+0,7	+1,4
	Minimum $\varphi = 0$	-0,6	-0,8	-1,3	-1,6	-0,6
	Minimum $\varphi = 1$	-1,4	-1,6	-2,7	-2,6	-0,6
-10	Maximum all φ	+0,4	+0,6	+1,4	+0,8	+1,1
	Minimum $\varphi = 0$	-0,6	-0,8	-1,3	-1,5	-0,6
	Minimum $\varphi = 1$	-1,4	-1,6	-2,7	-2,6	-0,6
-5	Maximum all φ	+0,3	+0,5	+1,5	+0,8	+0,8
	Minimum $\varphi = 0$	-0,5	-0,7	-1,3	-1,6	-0,6
	Minimum $\varphi = 1$	-1,3	-1,5	-2,4	-2,4	-0,6
+5	Maximum all φ	+0,3	+0,6	+1,8	+1,3	+0,4
	Minimum $\varphi = 0$	-0,6	-0,6	-1,4	-1,4	-1,1
	Minimum $\varphi = 1$	-1,3	-1,3	-2,0	-1,8	-1,5
+10	Maximum all φ	+0,4	+0,7	+1,8	+1,4	+0,4
	Minimum $\varphi = 0$	-0,7	-0,7	-1,5	-1,4	-1,4
	Minimum $\varphi = 1$	-1,3	-1,3	-2,0	-1,8	-1,8
+15	Maximum all φ	+0,4	+0,9	+1,9	+1,4	+0,4
	Minimum $\varphi = 0$	-0,8	-0,9	-1,7	-1,4	-1,8
	Minimum $\varphi = 1$	-1,3	-1,3	-2,2	-1,6	-2,1
+20	Maximum all φ	+0,6	+1,1	+1,9	+1,5	+0,4
	Minimum $\varphi = 0$	-0,9	-1,2	-1,8	-1,4	-2,0
	Minimum $\varphi = 1$	-1,3	-1,4	-2,2	-1,6	-2,1
+25	Maximum all φ	+0,7	+1,2	+1,9	+1,6	+0,5
	Minimum $\varphi = 0$	-1,0	-1,4	-1,9	-1,4	-2,0
	Minimum $\varphi = 1$	-1,3	-1,4	-2,0	-1,5	-2,0
+30	Maximum all φ	+0,9	+1,3	+1,9	+1,6	+0,7
	Minimum $\varphi = 0$	-1,0	-1,4	-1,9	-1,4	-2,0
	Minimum $\varphi = 1$	-1,3	-1,4	-1,8	-1,4	-2,0

Figure 21: Geometrical specifications of duo-pitch canopies – [8]

Table 6: Net pressure coefficients for duo-pitch canopies – [8]

For duo-pitch canopy roofs, trough or ridge shaped, the Eurocode prescribes six load cases to be considered: two cases with the entire roof loaded and four cases with only one pitch of the roof loaded, all for a net down acting and a net uplifting pressure. The case where the wind is parallel to the ridge or trough is not considered anymore, as it was the case for duo-pitch roofs. The net wind pressures acting on each pitch of the canopy roof will be rather low for this parallel orientation, as a result of the counteracting suction that is generated on both faces of the roof.

For the remaining orientations similar conclusions can be drawn as for duo-pitch roofs, by considering the presence of varying wind pressure acting directly on the bottom face of the canopy roof, in analogy to monopitch canopies. The pressure coefficient distributions for duo-pitch canopy roofs are very similar, with slightly lower C_p -values, to those of two intersecting monopitch canopy roofs. The trough shaped roof is intuitively loaded with upward lifting net pressure on the windward pitch and downward acting net pressure on the leeward pitch, while the ridge shaped roof is intuitively loaded with downward acting net pressure on the windward pitch and upward lifting net pressure on the leeward pitch, both with increasing C_p -values for steeper inclinations. Beside it is observed that the edges and the ridge are the most heavily loaded areas. However the rather limited inclination of canopy roofs makes them vulnerable for rapid changes of the net pressure orientation on both pitches, resulting in different possible load combinations. The different load cases and associated pressure distributions are function of a complex interplay between the approaching wind profile, the orientation, the pitch inclinations and the blockage under the canopy, generating zones of accumulation and separation or wake over the different roof faces. It is evident to see that it is very hard to predict which load case that will take place, since very slight changes of the above-mentioned parameters result in complete different pressure distributions. Consequently, the Eurocode prescribes a total of six load cases that have to be considered for the structural analysis of duo-pitch canopies to cover the most extreme and pernicious effects that may occur. Finally, for more detailed pressure distributions additional wind analysis is required.

3

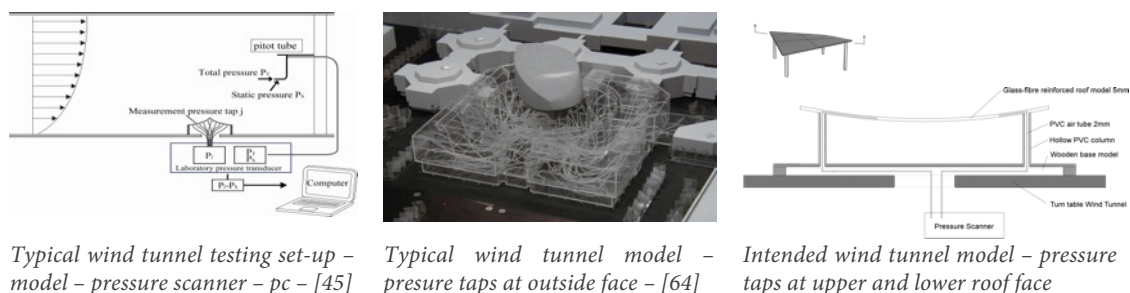
Wind Tunnel Models

3.1 Model Specifications

A large part of this master thesis is dedicated to the search for appropriate models for the intended wind tunnel experiments. The Eurocode nor specified literature provides any information about model or testing specifications in terms of testing height, thickness of the structure, wind speed and so on. They only focus on the pressure coefficient distribution for some typical standard structures with certain geometrical proportions. During this investigation the specifications for the models are defined as well as an appropriate fabrication process.

For the wind tunnel experiments, rigid models with a square ground plan are used. The dimensions are chosen in accordance to the maximum allowed degree of blockage for the wind tunnel as specified in section 4 Wind Tunnel Experiments. The thin-layered roof structures should allow simultaneous pressure measurement on both faces of the roof structure, where currently used wind tunnel models have solely pressure taps at the outside face of an enclosed volume (Figure 22). The measuring points on both faces should be aligned to the centreline of the structure to allow accurate summation of the net pressure coefficients for open canopy roofs. The models will be tested as a roof structure that is part of the building envelope and as a canopy structure itself, respectively with and without enclosing walls, for different angles of attack. The presence of walls will allow studying their influence on the pressure coefficient distribution on the external roof face, what can be expected by the redirection of the blocked airflow. Roof structures that are part of the building envelope will respond differently to the dynamic wind pressure compared to open canopy structures. The thickness of the testing models has to be reduced as much as possible to approximate the mainly single-layer very thin membrane structures, as the thickness of the roof boundaries will affect the airflow and thus the turbulence over the membrane. Nevertheless, the minimal dimensions are defined by the diameter of the used Polyvinylchloride (PVC) air tubes that connect to the measuring sensors of a pressure transducer. These tubes have an inner diameter of 1 mm and a wall thickness of 0,5 mm, which results in a 2 mm outer diameter. Moreover, the PVC tubes should connect perpendicular to the roof surface, referring to the nature of wind pressure acting perpendicular to surfaces. The tubes are then redirected through the tubular columns of the canopy structure to reduce the airflow disturbance as much as possible. Each column contains 15 or 16 of these PVC air tubes and is located at a corner of the canopy structure.

The use of rigid models is justified by the fact that the pressure distribution is function of geometrical factors, and thus in fact defines the pressure coefficients in concordance with the deflected mode of the membrane structure. This can be seen as considering the geometry of the deformed state. However it is very hard to define the deformed state of a membrane structure because the deformation is function of several interacting factors such as the membrane stiffness, the applied pre-stress, the supporting system, the applied loads, et cetera. In order to deal with these concerns, research has to be done on the parameters that mainly influence the deformation. Wind tunnel testing on properly scaled aero-elastic models of basic membrane structures could provide insights in the deformation behaviour of membrane structures in function of these parameters. However, due to the complexity of making and researching properly scaled aero-elastic models, this lies out of the scope of this master thesis.



Typical wind tunnel testing set-up – model – pressure scanner – pc – [45]

Typical wind tunnel model – pressure taps at outside face – [64]

Intended wind tunnel model – pressure taps at upper and lower roof face

Figure 22: Wind tunnel models – [45] [64]

3.2 Fabrication process

Nowadays the best-known and most common models for wind tunnel experiments in the field of aerodynamics and pressure distributions are enclosed rigid models that monitor pressure coefficients at the outer face (except for ventilation ducts where monitoring takes place at the inner face). In most cases the dimensions of the models allow incorporating the measuring device inside the model without disturbing the measurement. For the built environment these models are translated to a building envelope that encloses the measuring device and monitors the pressure distribution on the outer face of the envelope. For the intended wind tunnel experiments that monitor pressure coefficients simultaneously on both faces of a very thin roof structure it is impossible to implement the measuring device in the structure itself. Consequently, the measuring device should be placed outside the wind tunnel to ensure that the airflow, and therefore the measurements, will not be disturbed (Figure 22). To meet the requirements for this innovating measuring technique, research has been done for appropriate fabrication techniques and materials. A feasibility study in which different potential manufacturing techniques were compared was performed. The considered fabrication processes and techniques are briefly discussed for the most important requirements and directories.

3.2.1 Requirements

Production process

1. Model dimensions in relation to the wind tunnel section
2. Smooth and curved model surfaces
3. Design freedom for a large variety of roof shapes
4. Individual air channels for the pressure measurements
5. Position of pressure taps at predefined and fixed locations
6. Connection to the Scanivalve pressure sensors
7. Sufficiently accurate models (shape and measurements)
8. Ease of the fabrication process
9. Work hours, time is money
10. Production cost as low as possible
11. Technical feasibility of the production process

Material

12. High uniformity / low amount imperfections
13. Strength to withstand the wind actions during the wind tunnel experiments
14. Low brittleness to avoid cracking
15. Air tightness of the air channels for accurate pressure measurements
16. Design freedom for a large variety of shapes
17. Follow-up processability (rectify small flaws, polish surfaces...)
18. Material cost as low as possible

3.2.1.1 3D printing in ABS

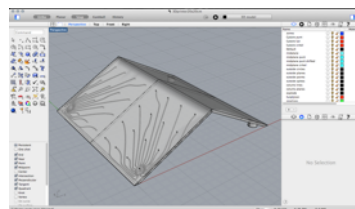
3D printing is an accurate (up to one fifth of a mm, depending on the printer resolution), but a very expensive way to produce almost any three-dimensional solid model from a digitally modelled shape. The basic principle of 3D printing is based on the addition of material, what is contrary to the more conventional machining techniques such as drilling, cutting and milling where you start from a solid block and remove material by subtraction. In fact a 3D printer starts from scratch and builds up the 3D model by computer controlled successive layering. Currently a lot of different types of 3D printers are for sale on the market, but the ones that are available at the university are based on fused deposit modelling (FDM). This kind of rapid prototyping extrusion-based 3D printers soften the thermoplastic acrylonitrile butadiene styrene (ABS) material that is fed to the machine on coiled cartridges and lays it down in successive layers on the printing plate where it cools down and hardens. ABS is a rather tough and impact resistant material.

The starting point for this production method (Figure 23) is virtually modelling the roof structure inclusive the internal air channels in Rhinoceros [52] and Inventor [2] and exporting the digital model to a 3D printable stl-file. This file is loaded into the CatalystEX 3D-print software of the Dimension 1200es 3D printer [61]. Here the support material is automatically added and the layer thickness is chosen at 0,1778 mm, after which the file is send to the 3D printer. The printer uses different material for the model itself and its supports. This allows dissolving the soluble support material away by submerging the printed model in a temperature and agitation controlled water-based solution of the SCA1200 support removal system

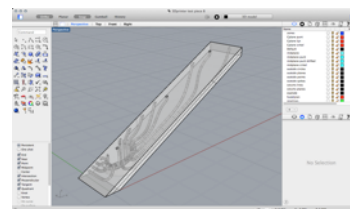
Nevertheless, after the production of some small test pieces it turned out that this production method is not suitable to fabricate the wind tunnel models. The 3D printer has been tested to its limits. The internal air channels of 1 mm in diameter are uncontrollable and clog up sometimes, what causes the impossibility to dissolve the internal support material away. Furthermore, these models will be very expensive and the maximal dimensions of the printable object are 254 mm x 254 mm x 305 mm, which only allows the production of rather small models. In addition, the printed models tend to be not fully airtight what could disturb the measurements.



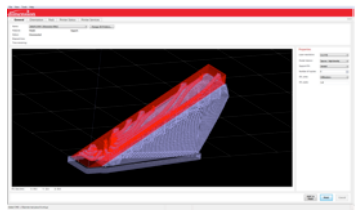
Dimension1200es 3D printer



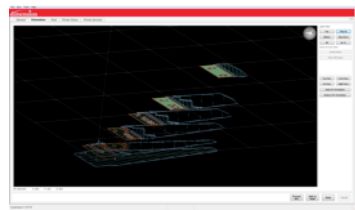
Pitch roof modelled in Rhinoceros with internal air channels



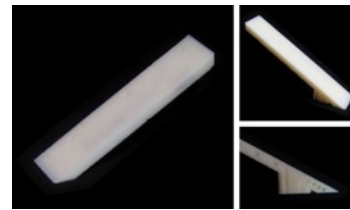
Detail of pitched roof for testing



Test piece of roof in catalystEX 3D-print software; red roof model; purple support material



Layered 3D-print model showing model and support material for some layers



3D printed test piece; internal air channels clog up; internal support can't dissolve away by submerging

Figure 23: 3D printing procedure

3.2.1.2 Male CNC milling

Milling is currently one of the most frequently used production processes for three-dimensional solid shapes and is based on subtraction processes. A milling machine removes material from a solid block or plate by rotating cutters that are fed through the material. Nowadays a wide variety of milling machines exists, ranging from manually controlled to computer numerical controlled (CNC) variants. A CNC milling machine works with very high accuracy and is operated by G-codes that define the tool paths for the milling process of a numerical or digital model. At the university a BZT gantry CNC milling machine [10] can be used. This computer-controlled type of milling machine with a workable area of 2500 mm by 1500 mm is particularly suitable for the processing of sheet material. The maximal thickness of the sheet material that can be handled is limited by the type of milling operation and cutter length that has to be used, as a result of the limited free height of 150 mm under the horizontal axis onto which the spindle head is mounted. The spindle head can only move horizontal over the working area along the X- and Y-direction and vertical along the Z-direction, thereby no rotation axes are available, nor on the workable area or on the spindle head itself. In addition, the cutting tools have to be changed manually by the absence of an automatic tool-changer.

The starting point for the procedure to CNC mill the male roof structure would be computer modelling the roof structure in Rhinoceros and Inventor. At a very early stage it became clear that positive milling of the roof structure would be very hard as it is impossible to mill the internal air channels of the roof structure. A solution could be to assemble the roof structure from an upper and a lower part that should be milled separately. Beside the large amount of material that has to be milled away, it is very hard to seal both faces perfectly onto each other by securing the airtightness of the internal air channels. However implementing PVC air tubes in between the upper and the lower part of the roof can solve this difficulty. The hardest part is the manual rotation and reconfiguring the null point of the work piece and to mill the extremely thin roof parts without damage or flaws. The only possibility for this technique would be the use of more advanced five-axis CNC milling machines, but sub-contracting this technique will be very expensive. Moreover, a manual assembly of the roof parts and the PVC air-tubes would be required, what amortises the potential of this concept.



BZT mill and computer actuator



BZT Spindle head

Figure 24: BZT portal CNC milling machine

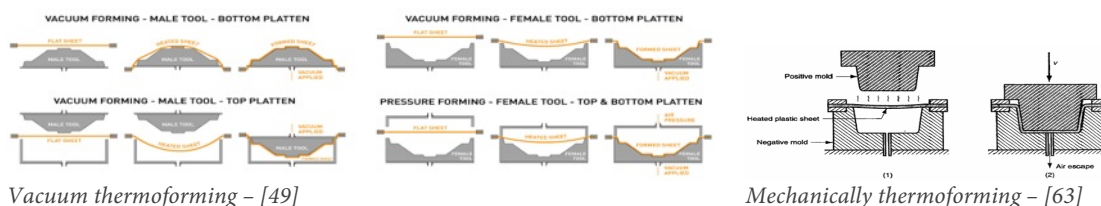
3.2.1.3 Thermoforming of thermoplastics

Continuing on the idea of assembling the roof from two parts while implementing the PVC air tubes, the concept of vacuum forming came up. This is a more advanced technique of thermoforming. In the process of vacuum forming, a sheet of thermoplastic material is heated up to its forming temperature after which it is stretched over a half-open male or female mould by applying a vacuum. When the thermoplastic has adopted the shape of the mould it is cooled down to harden and finally, the mould is removed. Despite the relatively ease of fabrication this production process is impossible to fulfil because there is no vacuum forming machine available at the University.

The starting point for this technique is virtually modelling a half open female mould for the roof structure in Rhinoceros and Inventor. This mould could be CNC-milled in a heat resistant and structurally stable material onto which the roof surfaces are vacuum formed in Plexiglas. Therefore, a thin sheet of Plexiglas is heated in an oven up to its forming temperature and vacuum formed over the female mould. After cooling down and hardening the measuring points should be placed and drilled by hand where the PVC air tubes should connect perpendicular to the roof surfaces. It is obvious that this manually performed step will lead to larger inaccuracies for more complex shaped roofs. In a last step the entire roof structure inclusive PVC air tubes should be assembled.

In the same sequence of vacuum forming lies the concept of mechanically thermoforming, with a very similar production process. In the process of mechanically thermoforming, the heated sheet of thermoplastic material is mechanically stretched over a half open or female mould. Besides, it is also possible to heat up the sheet of thermoplastic material close up to its reflux temperature to have gravity taking over the mechanically stretching.

This last principle brought up the idea to form the roof structure at ones with the implemented air channels. However, this concept is not suitable for vacuum forming or mechanically thermoforming because those channels will clog up. The concept was based on the idea of stacking three layers of 2 mm Plexiglas one on top another other and thermoform them at once. The middle layer would have laser cut openings into which the PVC air channels would be placed. However this concept has been amortised in the conceptual phase by the uncontrollable stretching during thermoforming. Especially for double curved surfaces where significant plastic deformation occurs by the absence of a cutting pattern this would result in uncontrolled thicknesses, mismatching of the locations of the air channels and the position of the measuring points in the final shape.



Vacuum thermoforming - [49]

Mechanically thermoforming - [63]

Figure 25: Thermoforming process - [49] [63]

3.2.1.4 Gypsum / IPC / Polyester composite on half-open mould

To counter the uncontrollable deformations and air channel locations in the case of thermoforming, manually laminating the roof structure on top of a half open female mould could be an alternative low-cost solution. At the very beginning, it was suggested to assemble the hypar mould from straight MDF laths and smoothen up the surface by removing material with sand paper or applying gypsum or other resins. It turned out rather quickly that it was very hard to assemble the laser cut MDF layers with high precision on one hand and to control the curvature of the mould during the manually smoothening process on the other. Therefore, the concept of CNC milling the mould became almost inevitable. After completion of the half open mould the manually forming process in gypsum, IPC or polyester could take place. Gypsum was the first material to be amortised because of its brittle behaviour and the breaking potential of the fragile thin roof structure during the wind tunnel experiments. Subsequently, Vubonite, a glass-fibre reinforced laminate that has been developed at the Vrije Universiteit Brussel was suggested to encounter the breaking potential of the thin roof structure. The process of lamination will allow better control on the positioning of the PVC air tubes inside the roof structure, but some new problems showed up. Firstly, Vubonite is not translucent which would make it very hard to locate and drill holes in the air channels or to penetrate them with needles after completion of the roof structure.

To encounter this problem the more translucent Polyester was suggested. In this case it would be possible to fill the air channels with a coloured fluid in order to make them visible after completion of the structure. Nevertheless, for these very small tubes complete removal of the fluid would be very difficult, once again raising the potential of clogging up the air channels and disturbing the pressure measurements. Finally, the problem of drilling holes or the penetration the PVC air tubes with needles was countered by the idea of implementing bended steel tubes that connect to the measuring points at the roof surface to the PVC air tubes. In this concept it is difficult to accurately place the measuring points on the free surface and to hold them in position during the drying process. The solution to deal with this inconvenience was to create a fully enclosed female mould that not only shapes the roof structure, but also fixes the measuring points in place at the same time. Additionally, the fully enclosed mould allows better control on the overall roof thickness and finishing. The steel bends were formed by a self-made apparatus that prevents the tubes from folding tight during the bending process by clamping the tube diameter at the bending position.

3.2.1.5 IPC composite in fully closed mould

The final models that were used for the wind tunnel experiments are made in Vubonite. First an appropriate fully enclosed female mould was made in which the male roof structure was formed. The mould can be assembled out of plane laser cut MDF surfaces or 3D CNC-milled out of high-density PUR foam, depending on the geometry of the considered roof structure. When the mould is finished, the glass-fibre reinforcement mats and PVC air tubes are put in place, where after the mould is sealed properly and filled up with the Inorganic Phosphate Cement (IPC) matrix on a vibration plate to remove the internal air bubbles. After drying and post curing in an oven at 50 °C, the mould is removed and the male roof structure is polished and posted on four hollow PVC columns.

3.2.1.6 Synthesis feasibility study

The outcome of the feasibility study showed that the most appropriate manufacturing technique for the intended wind tunnel models is based on the production of handmade Vubonite-laminates that are formed in a fully enclosed female CNC-milled mould.

Production process	Model specifications							Feasibility			
	1	2	3	4	5	6	7	8	9	10	11
	Dimensions	Smooth & curved surfaces	Design freedom	Individual air channels	Position of pressure taps	Connection Scanivalve	Overall accuracy	Fabrication process	Work hours	Production cost	Technical feasibility
Monomaterial model											
3D printing	-	+	+	0	+	0	+	+	+	-	0
Masculine milling - CNC	0	+	0	-	+	0	+	-	+	-	-
Thermoforming	0	+	0	0	-	0	0	-	0	0	-
Composite model + pvc air tubes											
Half-open mould - Lasercutter	+	-	-	+	0	+	0	0	0	+	0
Half-open mould - CNC	+	0	0	+	0	+	0	0	0	0	0
Fully enclose mould - CNC	+	+	+	+	+	+	+	+	0	0	+

Table 7: Synthesis feasibility study of the production process

Material	Characteristics				Fesability		
	12	13	14	15	16	17	18
	Uniformity / imperfections	Strength	Brittleness	Air tightness	Design freedom	Follow-up processability	Material cost
3D printed ABS	+	0	+	0	+	0	-
CNC-milled PUR High density	0	0	0	0	0	0	0
Handmade Gypsum	0	-	-	0	0	+	+
Thermoformed Plexi	0	0	+	+	0	-	0
Handmade Polyester-laminate	0	+	0	+	+	+	+
Handmade Vubonite-laminate	0	+	0	+	+	+	+

Table 8: Synthesis feasibility study of the material

3.3 Wind Tunnel Models production

The roof structures for the wind tunnel experiments are modelled in an IPC composite that is shaped in a fully enclosed female mould. The models have been made point symmetrical to simplify the overall geometry of the roof and to reduce the amount of PVC air tubes that have to be implemented in the thin-layered roof structures. Each model has a projected square ground plan measuring 400 mm by 400 mm and is founded on four circular PVC tube columns that are mounted onto a wooden base. This base can be secured on the bottom of the wind tunnel. The columns are placed at an offset of 25 mm from each roof edge and function as transition element between the roof structure and the wooden base. The columns transmit the wind loads that act on the roof faces to the base plate and at the same time the hollow inner core of the columns is used to redirect the PVC air tubes that are implemented in the roof structure to the void space that is provided in the base. This negative volume is created by gluing four mitred slats of 18 mm thick onto a square base plate of 500 mm by 500 mm. The void provides sufficient space to connect the redirected air tubes to a Scanivalve measuring device, which will be mounted under the wind tunnel. The Scanivalve has a maximum of 64 measuring channels, which results in a maximum of 16 air tubes that have to be redirected through each column. Consequently, the PVC columns have an inner diameter of 12 mm with a wall thickness of 2 mm, allowing 16 PVC air tubes of 2 mm in diameter to be redirected. The columns provide structural stability to the supported roof structure and are placed in four holes that are drilled into the base plate. The columns are glued in place by applying TEC 7 to ensure the load transmission of the connection. The wooden base on its turn can be secured in the bottom plate of the wind tunnel by screws and angle profiles to fix the model in place and dissipate the applied wind forces.

Depending on the overall geometry of the roof structure the mould is assembled from plane laser cut MDF surfaces or from 3D CNC-milled high-density PUR foam layers. For simple models with a small amount of straight faces it is possible to use the laser cutter and manually assemble the different plane faces, while for more complex and organic surfaces the CNC milling machine is used to mill sequential layers that have to be stacked one on top of another. For each of the following roof structures, the removable wall elements are laser cut and secured onto the wooden base by angle profiles and screws.

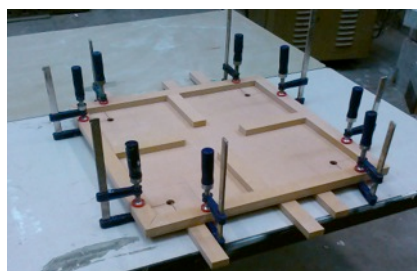


Figure 26: fabrication process wooden base

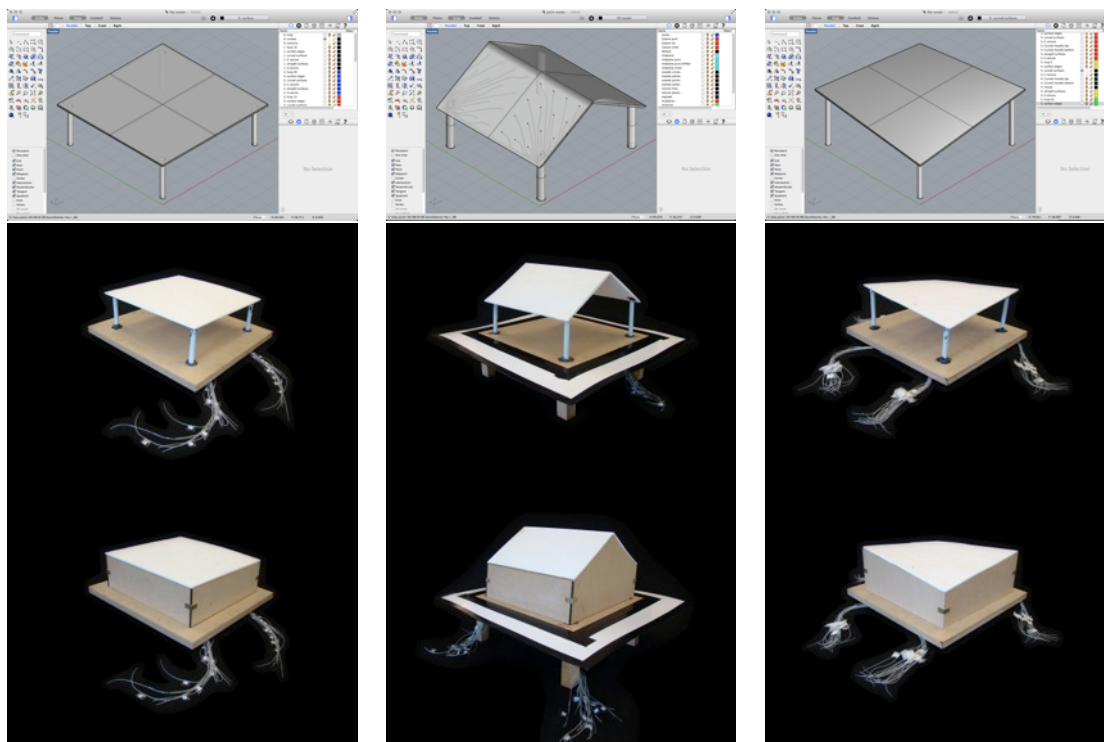


Figure 27: Virtual and scaled test models for wind tunnel experiments; flat, duo-pitch and hyper roof

3.3.1 Flat Roof Structure

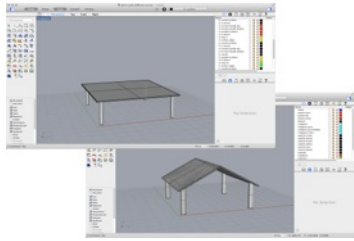
The flat roof structure has a square ground plan of 400 mm by 400 mm, a thickness of approximately 6 mm and is elevated on four columns of 125 mm high. The bisymmetry of the roof structure allowed reducing the number of measuring points and thus number of PVC air tubes that had to be implemented in the model, as the roof can be subdivided into four identical quarters. Each quarter has a smaller square surface of 200 mm by 200 mm in ground plan and contains one column in its outer corner of the roof structure. Consequently, it is sufficient to provide one quarter with measuring points at its upper face and one quarter with measuring points at its bottom face to cover the entire roof surface with pressure coefficients during the wind tunnel experiments for a 360° measuring sequence. Taking into account that the Scanivalve has a maximum of 64 measuring channels and that one column can redirect 16 PVC air tubes it is straightforward to provide 16 measuring points per quarter. The proposed layout of the maximal 64 measuring points is based on a grid structure that guarantees 16 measuring points per quarter while every measuring point covers an equally projected roof surface area. By dividing the roof structure into its different pressure zones as defined in the Eurocode, every zone is covered by minimum three measuring points.

The fabrication process is illustrated in Figure 28. The mould for this very simple structure has been assembled from three stacked 6 mm thick laser cut MDF surfaces. Two surfaces of 445 mm by 440 mm, one for the top layer and one for the bottom layer, and one u-form to seal the mould at three sides leaving one open to allow pouring and filling up the mould. The upper and lower surface are equipped with holes of 2 mm in diameter at the locations specified as measuring points, i.e. 16 on the top layer and 15 on the bottom layer (it is impossible to place the 16th measuring point at the bottom face because it interferes with the location of the column). Before closing the mould all elements are lacquered and greased with beeswax to make sure that the male roof model will release from the female mould after drying. Thereafter a layer of 300 gr/m² randomly oriented glass-fibres is applied onto the outer faces of the mould and impregnated with the IPC matrix, followed by placing the PVC air tubes. The air tubes are put through the provided holes in the upper and lower face of the mould to fix the measuring points during the pouring process. Afterwards, they are redirected through the columns in a sequence that avoids them folding tight or getting clenched when closing the mould. Subsequently, the mould is closed and sealed properly with clamps to prevent leaking during the pouring process. The mould is poured up with IPC matrix under continuous movement on the vibration plate to remove the air bubbles from the model and to improve the pouring process. When pouring has finished the roof structure is dried for one night at ambient temperature after which it is post-cured for six to twelve hours in an oven at 50 °C. After the post-curing process, the roof structure is released from its mould and the protruding air tubes are cut off on the level of the corresponding roof faces. Hereafter the roof edges and surfaces are polished and small flaws are manually concealed. Finally, the roof structure is mounted and glued onto the four columns of the base.

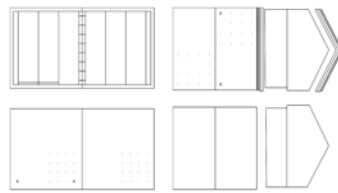
3.3.2 Duo-pitch Roof Structure

The duo-pitch roof structure has a square ground plan of 400 mm by 400 mm and a thickness of approximately 6 mm. Both roof sides have an inclination of 30° to the horizontal plane, generating a positive ridge in the middle of the structure. The low ends of the roof are elevated on four columns of 120 mm high, causing the ridge to be located at a height of 235 mm. Similar to the previous model this model is also bisymmetric, which allows applying the same reduction principle for the amount of measuring points as for the flat roof structure.

The production process for this duo-pitch roof is very similar to the one that has been used for the flat roof structure (Figure 28), except that this mould is a bit more complex. The mould is assembled of more surface elements that have to be mitred after laser cutting for perfect fit. After post curing, an additional 30 gr/m² glass-fibre mat is laminated on the outside faces to smoothen up the external surfaces of the model.



Virtual roof models in Rhinoceros; left: flat roof; right: pitch roof



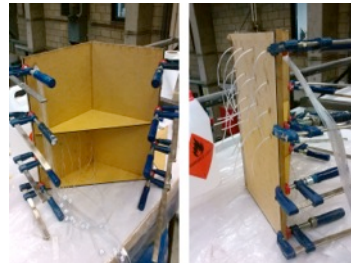
Dxf drawing to Laser cut the mould elements and walls; left: flat roof; right: pitch roof



Assemble mould from the laser cut faces and grease mould; pitch roof



Place and impregnate 300 gr/m² glass-fibre mat; place and redirect the PVC air-tubes; bend steel tubes at endpoints of some PVC air tubes; pitch roof



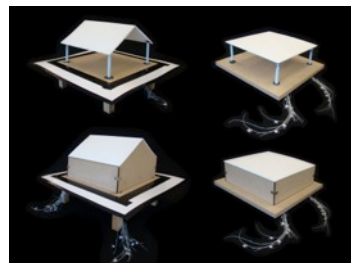
Close mould and secure from leakage by clamping; pitch roof



Pour up mould with IPC matrix on the vibration plate to remove internal air bubbles and improve the pouring process; left: pitch roof; right: flat roof



Remove mould after post curing; cut protruding PVC air tubes; polish model surfaces; additional glass-fibre membrane of 30 gr/m² to smoothen surfaces of pitch roof



Poste model onto wooden base structure; redirect PVC air tubes trough columns; fit walls in place; left: pitch roof; right: flat roof

Figure 28: Fabrication process flat and duo-pitch roof

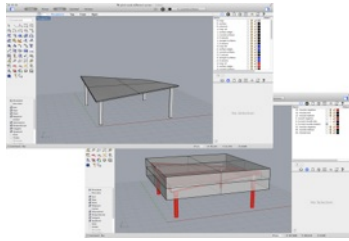
3.3.3 Hypar Roof Structure

A hypar is defined by its shape parameter, being the ratio of the diagonal dimension to the vertical distance between the high and low corners. For this hypar roof structure the shape parameter is set to 11,3, considering a square ground plan of 400 mm by 400 mm, a thickness of approximately 5 mm and a height difference of 50 mm between the two high points and the two low points. Once again the roof structure has a geometrical symmetry to reduce the total number of measuring points. The point symmetry of the roof structure allows defining the pressure distribution over the entire roof by the maximal 64 measuring points of the Scanivalve during the wind tunnel experiments for a 360° measuring sequence. Consequently, two neighbouring quarters of the roof structure (a high and a low one) will be provided with measuring points on the upper face of roof, while the other two quarters will have measuring points on the bottom face.

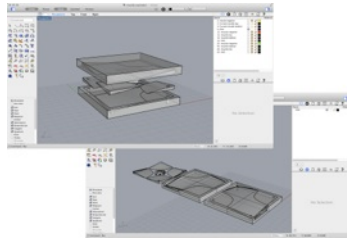
The fabrication process is illustrated in Figure 29. The production process for this anticlastic hypar roof structure is rather similar to the one of the flat roof and the duo-pitch roof, except for the production of the mould itself. The mould of this double curved hypar roof structure is assembled of three layers high-density PUR foam, which have been CNC-milled by using the BZT granty CNC milling machine. At first the female mould has been virtually modelled in Rhinoceros and Inventor. The mould is formed from two parts, a top and a bottom part, fitting perfectly one into another. For a three- or five-axis 3D CNC milling machine the modelling is finished here and both parts of the mould could be milled in one piece. Unfortunately, this was not possible with the BZT granty CNC milling machine, what resulted in assembling both mould parts from various layers that had to be stacked one on top another. Taking into account the thickness of the foam plates, which is 50 mm, the mould is assembled of 49 mm thick layers. The first mm of the plate has been milled away to ensure perfect matching of the stacked layers.

The virtual mould is subdivided in layers of 49 mm and exported as an stl-file. This file is imported in the Deskproto software [14] to simulate the milling process and write the corresponding nc-file that was sent to the CNC milling machine. In Deskproto the different milling operations and their corresponding tools, paths, diameters, feed rates and plunging rates are defined. To reduce the milling time, different subsequent milling operations were used as recommended. The milling process for each layer is composed of four milling operations. First a roughing operation that takes away large parts of material in a short amount of time, followed by two finishing operations to create a smooth surface and finally, a contouring operation to cut the mould layers loose. In the absence of an automatic tool changer the entire milling process is done with the same cutting tool, an 8 mm flat tip milling head, because manually changing the cutting tool goes hand in hand with manually reprogramming the null point of the work piece resulting inevitably in deviations and mismatches. This 8 mm flat tip milling head gives a good correlation between time consumption for milling and the surface finishing. It is possible to add more milling operations. An extra finishing operation could create a smoother surface, but at all times a proper balance should be considered between milling time and finishing details. For example, a thinner head or a ball tip head will improve the surface smoothness, but they will also need a smaller tool path distance, which on its turn will result in a significant longer tool path and a drastic increase of milling time. Once all milling parameters are set and the milling simulation is satisfactory, the nc-file is written. In this file, all these milling operations are translated into G-codes, which are read and executed line per line by the milling machine. When the milling process has finished, the last refinements are done by hand and the layers are glued one on top another. The two mould parts are sand down and polished by hand to remove some small flaws of the milling process and to achieve a satisfactory smoothness after which the moulds are lacquered. Finally, the 64 trenches are drilled by hand on the corresponding mould quarters to fix the PVC air tubes at the location of the measuring points during the pouring process. The trenches are drilled perpendicular to the surface, once again according to the nature of the wind load acting perpendicular to the surface.

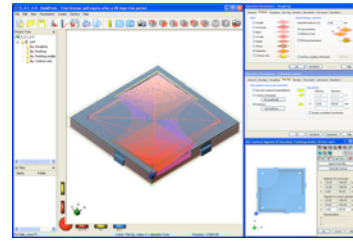
The rest of the production process is rather similar as discussed in the section of the flat roof structure. The mould is greased, where after the glass-fibre mats are placed and impregnated, followed by positioning the PVC air tubes in place. Mark that in this case at first a glass-fibre mat of 30 gr/m² is placed at the outside for a smoother surface finishing, followed by a 300 gr/m² glass-fibre mat to ensure the strength of the model. Then the mould is closed and secured by threaded rods and nuts before it is poured on top of the vibration plate. Subsequently, the model is dried, post cured, and finally, removed from its mould, polished and posted on top of the base structure. The low corners of the roof are elevated on two columns of 115 mm high, causing the high points to be elevated on two columns of 165 mm high.



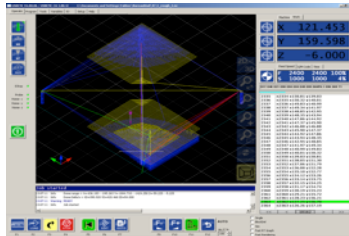
Virtual roof model and negative mould in Rhinoceros



Subdivide mould in layers and translate them to fit within the PUR foam plate for milling



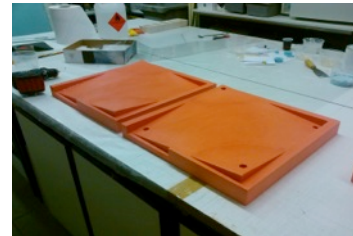
Define milling operations and toolpaths in DeskProto



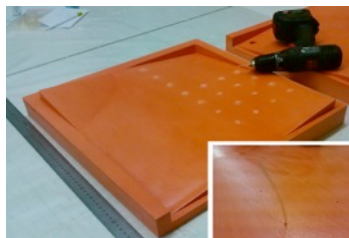
nc-file read by USBCNC4 software that operates the BZT granty CNC milling machine



CNC mill the mould layers; bottom layer after finishing operation; top layer at roughing operation



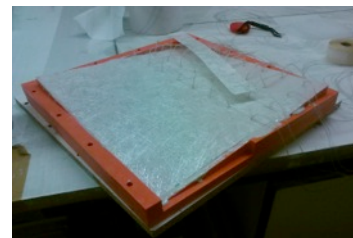
Glue the mould layers one on top another; polish surfaces; lacquer and grease the mould



Drill trenches to fix the PVC air tubes at the measuring points



Place and impregnate 30 gr/m² glass-fibre mat



Place and impregnate 300 gr/m² glass-fibre mat



Redirect PVC air tubes at the bottom side through the columns in a pattern that avoids cleching the tubes by closing the mould



Redirect PVC air tubes at the top side through the columns in a pattern that avoids cleching the tubes by closing the mould



Close the mould and secure from leakage by bolting both mould parts together; the wooden sheets prevent damaging the mould itself



Pour up the mould with IPC matrix on the vibration plate to remove internal air bubbles and improve the pouring process



Remove mould after post curing; cut protruding PVC air tubes; polish model surfaces; poste model onto wooden base and make walls

Figure 29: Fabrication process of the hypar roof with a shape parameter of 11,3

4

Wind Tunnel Experiments

4.1 Experimental set-up

The last main part of this thesis is the wind tunnel testing itself. Most pressure coefficient distributions presented in the Eurocode are based on extensive wind tunnel studies for specific design situations. Wind tunnel testing is used as an alternative for the existing codes where design situations fall outside the standard scope that is illustrated in these codes. Wind tunnel experiments are commonly used to study the wind loading with a higher degree of accuracy or for the validation of numerical methods such as CFD calculations. Moreover, the codes recommend the need of wind tunnel testing for cases that significantly differ from the standard situations. From this point of view wind tunnel testing is used in this thesis for validation in accordance to the codes and for fundamental research of data on new structural typologies that are introduced by the implementation of membrane structures.

In a first stage, wind tunnel testing was performed for some common roof structures that are presented in the Eurocode. These simple structures are used to validate the wind tunnel experiments and to create a reference-testing field for the tests on double curved hypar roofs, by confronting the experimentally obtained pressure coefficients with the ones that are illustrated in Eurocode 1. EC1 – part 1.4 defines for canopy roofs net pressure coefficients which are the vector summation of the pressure coefficients acting simultaneously on the external and internal roof faces, while for building roofs only the external pressure coefficients are defined with the internal pressure function of the present openings and leakages in the building envelope. The building forms defined in EC1 – part 1.4 and many other codes do not match with the more organic shapes of the doubly curved membrane structures. In a second stage the local pressure distribution is experimentally defined for doubly curved hypar roofs part of a building envelope, and as open canopies itself. These pressure distributions can only be compared superficially and with care to the limited amount of specified literature that is available.

4.1.1 Wind tunnel

At the department of Toegepaste Mechanica at the Vrije Univesiteit Brussel two industrial open return wind tunnels are available: a large section and a smaller one. Both wind tunnels are computer operated by the Labview software and are mainly used for student instruction and experimentation. An open return wind tunnel is open at both ends and draws air from the room in the test section at one end and exhausts the air after diffusing at the other end. The wind tunnel testing for this thesis is performed in the large wind tunnel, designed and manufactured by T.E.M. ENGINEERING LIMITED Crawley England (Figure 30 and Figure 31). This industrial wind tunnel has a total length of approximately 25 m and is designed especially for wind tunnel tests simulating the lower parts of the atmospheric boundary layer. A centrifugal flat tumble fan (a), which is operated by an electric motor, drives the wind tunnel. This type of fan has shown to be superior to axial fan types in reducing the turbulence and improving homogeneous wind flow as much as possible. The fan is connected to a stabilisation chamber (b) containing an effusor or fine meshed screen that stabilises and straightens the flow and reduces the turbulence. This chamber has a narrowing conic shaft to bundle and accelerate the wind flow that is generated by the fan up to a wind velocity of 20 m/s in the test section that connects to the stabilisation chamber. The test section (c) of 12 m long, 2 m wide and 1 m high, is equipped with transparent PVC windows allowing visual monitoring and the use of flow visualisation techniques such as smoke screens during testing. A turntable of 1,5 m in diameter is implemented in the rear part of the test section's floor, allowing manually rotating the test piece that is mounted on top of it. At the rear of the wind tunnel a vertical diffuser (d) with a widening conic shaft reduces the wind speed before exhausting the residual wind through the vertical outlet at the top of the diffuser.

Since an open wind tunnel is in direct contact with indoor climate of the room, which in turn is in contact with the outside environment, it is important to note that open wind tunnel experiments are weather and wind affected. In order to control these effects, the wind tunnel is equipped with a pitot-static tube near the top of the test section recording the flow and environmental conditions in the free field of the wind tunnel. The instruments

measure the flow velocity, the total air pressure, the temperature, the relative humidity and the air density in the test section of the wind tunnel. Besides, one has to consider a maximum degree of blockage of 5% up to 10% for accurate wind tunnel testing. Blockage refers to the ratio of the projected maximum blocked cross-sectional area to the total cross-sectional area of the test section. Consequently, blockage is the dedicating parameter for the dimensions of the wind tunnel test models and should be maximal 10% for adequate measuring conditions. For larger degrees of blockage additional corrections should be applied to the experimentally obtained test results, but depending on the aerodynamics slightly larger blockages are allowed without affecting the test results.



Figure 30: Large wind tunnel at the VUB

Large Wind Tunnel VUB

Type	Open Return Wind Tunnel
Manufacturer	T.E.M. ENGINEERING LIMITED Crawley England
Working cross section	2 m x 1 m
Maximum wind speed	20 m/s
Maximum blockage	5-10%

Table 9: Wind tunnel characteristics

The long test section is especially designed for atmospheric boundary layer wind tunnel testing. Ir. De Paepe W. has investigated in the context of a doctorate, the test set-up for the atmospheric boundary layer profile that is classified as terrain category III in EN 1991-1-4. The designed set-up is shown in Figure 32 containing the following typical features seen from upstream: a castellated barrier wall to generate large scale turbulences and to reduce the wind speed in the lower sections, followed by an array of four quarter ellipse shaped spires that generate vortexes, and about 7 m of cubic shaped roughness elements mounted on the floor of the test section to complete the boundary layer flow. Depending on the wind tunnel and the atmospheric boundary layer to be generated the geometrical dimensions and proportions of these typical features have to be investigated.

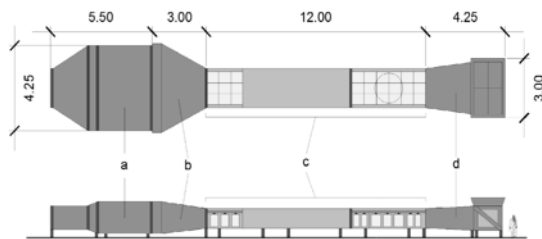


Figure 31: Top and side view of the large section open return wind tunnel at the VUB

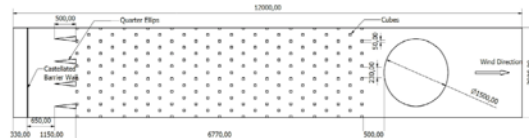


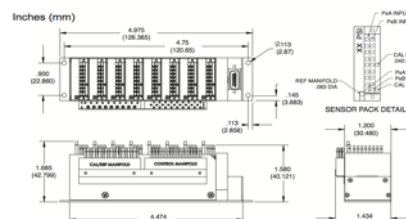
Figure 32: Top view of test section set-up for atmospheric boundary layer generation by Ir. De Paepe W.

4.1.2 Scanivalve

The pressure measurements are recorded by a computer controlled Scanivalve, type ZOC33/64 Px 10” H₂O, manufactured by SANIVALVE CORP. USA [56] (Figure 33). This electronic valveless pressure-scanning module has one reference pressure channel and 64 measuring channels, each having its individual silicon pressure sensor. The measuring channels have an inner diameter of approximately 1 mm and are grouped in eight arrays of eight channels, each array referenced individually to the reference pressure. Consequently, the Scanivalve can convert up to a maximum of 64 simultaneous pneumatic inputs into electronic signals with a frequency range from 1 Hz up to 500 Hz. The Scanivalve has an accuracy of 0,15% on its full-scale range of 10” H₂O (or 0,15% on 2490,82 Pa).



Figure 33: Scanivalve ZOC33/64Px – [56]



4.1.3 Measurement set-up

The measurement set-up is illustrated in Figure 34. The test models are placed in the middle of the turntable to allow rotation of the model and to minimize the influence of the boundary layer effects that are present near the walls of the wind tunnel. In the centre of the turntable a cylindrical hole is provided to redirect the PVC air-tubes, that end in the void wooden base of the model, to the outside of the wind tunnel. The Scanivalve is placed underneath the wind tunnel to not disturb the measurements. All redistributed PVC air tubes of the model are connected to the Scanivalve measuring channels. Mark that the boundary layer effect near the floor of the test section is present as the model is placed onto the bottom of the wind tunnel test section. The model is secured in place by screws fixing the model onto the turning table and preventing displacements of the model under the acting wind loads during the experiments. The flat bottom plate could be seen as the worst-case terrain category of the Eurocode (terrain category 0). All roof structures are stated on columns causing that the actual measurements can be assumed in the free flow field of the test section, where the flow is considered to be independent from the height and the mean wind speed to be equal over the height of the roof structure.

As earlier mentioned does the Scanivalve ZOC33/64Px record all pressure measurements in relation to a reference pressure. At the beginning of each testing sequence the Scanivalve is calibrated relative to a static reference pressure taken at the bottom of the wind tunnel test section in front of the turntable, causing all measurements to be pressure variations between the roof surface and the reference pressure. The pressure measurements are carried out with sufficiently high frequency and for a sufficiently long time to allow the use of mean values and to reduce the turbulence effect on the process of averaging. In addition, the flow and the environmental conditions in the free field of the wind tunnel are measured at the start of each individual wind tunnel test to define the framework for the running test. During the experimental testing sequence, the models will be tested for different building conditions, wind speeds and orientations to investigate their influence on the experimentally obtained data and the resulting pressure coefficient distributions. Finally, the measurements have been repeated several times to confirm consistency in the experimental results.



Wind tunnel experiment set-up, computer control, LabView software; pitot measurements; Motor drive; Scanivalve measurements



Model placed in the middle of the turn table and secured by angle profiles and screws; pitch roof



Scanivalve placed underneath the wind tunnel; connection of the redirected PVC air tubes to the Scanivalve pressure sensors

Figure 34: Measurement set-up

4.1.4 Measurement methodology

The wind tunnel testing has to be carried out in accordance to the bi-symmetrical pressure tap layout of the fabricated test models to account for a full pressure distribution profile over the considered structure. Each model will be tested under continuous rotation by hand to define the most critical angles of attack, and will be tested under specific incident wind angles. The discrete testing principle records the pressure measurements for azimuth angles varying over 180 degrees to account for the bi-symmetry of the model tap layout.

The recorded wind tunnel data and results have been converted into pressure coefficient distribution charts by considering the geometry and the pressure tap layout of the wind tunnel model (Figure 35). Pressure coefficient distribution charts are made for different wind orientations to facilitate their use in wind load calculations as presented in the Eurocode. The pressure coefficients are calculated from the exported testing data of the Scanivalve by the following formula, that translates the mean wind pressure in each tap recorded during the wind tunnel testing into a pressure coefficient that is independent from the wind velocity and air density. The obtained pressure coefficients are thus the dimensionless form of the recorded pressures over the considered structure.

$$C_p = \frac{P - P_0}{\frac{1}{2} * \rho * V^2} = 1 - \left(\frac{V}{V_0}\right)^2$$

with:

- C_p the local pressure coefficient for the considered tap
- P the wind pressure at the considered tap during testing
- P_0 the static reference wind pressure
- ρ the air density during testing
- V the wind velocity at the considered tap during testing
- V_0 the static reference wind velocity

The pressure coefficient equation shows that at locations where $P > P_0$ or $V < V_0$ accumulation of wind results in positive C_p -values and pressures, while for $P < P_0$ or $V > V_0$ efflux of wind results in negative C_p -values and pressures (suction), and if $P = P_0$ or $V = V_0$ the free stream of wind results in C_p -values and pressures equal to 0. The equation can be extended for mean and peak pressure coefficients as illustrated below. For this thesis is only focussed on the mean values there we are interested in the overall pressure distribution over the entire structure. Besides, does the calculation method as presented in the Eurocode already account for the peak loads by the turbulence intensity in the mathematical representation of the turbulent nature of wind.

$$C_{p,mean} = C_p = \frac{\Delta P_{mean}}{\frac{1}{2} * \rho * V_{mean}^2}$$

$$C_{p,peak} = G * C_p = \frac{\Delta P_{peak}}{\frac{1}{2} * \rho * V_{peak}^2}$$

The formula above clearly indicates the influence of aerodynamics on the pressure coefficient distributions around building structures. Air and wind pressure builds up at faces that obstruct the free flow of wind on the front surfaces. In addition, wind fails to flow around sharp edges and corners and separates consequently. It is difficult to predict the position of these separation points there they are function of several parameters, including the magnitude of viscosity forces that dominate the flow. These forces can be accounted by the Reynolds number, which allows describing a flow rather as laminar or turbulent.

$$R_r = \frac{\text{inertia forces}}{\text{viscous forces}}$$

Hereby, one can conclude that the pressure distribution and the wind loads acting on a structure are function of local variations in fluid velocity induced by the geometry of the structure, including the presence of Venturi effects and the location of the separation points.

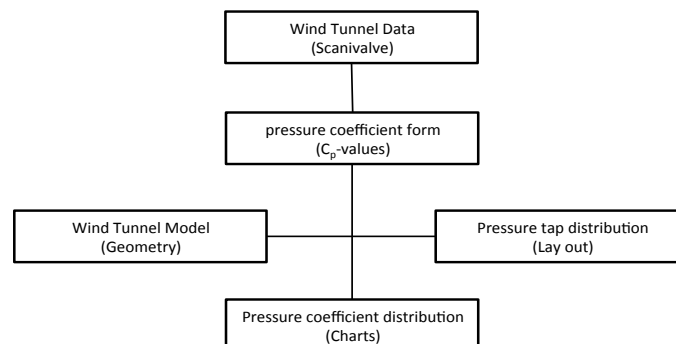


Figure 35: Flow chart measurement methodology

The recorded wind tunnel data of the Scanivalve is transformed into pressure coefficients (C_p -values). These pressure coefficients are then used to generate pressure coefficient distribution charts by considering the geometry and the pressure tap layout of the wind tunnel model.

4.2 Measurements

The wind tunnel experiments for each of the following six cases (flat roof, flat canopy, duo-pitch roof, duo-pitch canopy, hyper roof and hyper canopy) are performed under continuous manual rotation of the turntable and for discrete angles of attack. A detailed overview of the exact wind tunnel testing conditions is listed in the corresponding table for each test case. The recorded wind tunnel data for all experiments are processed and visualised in pressure graphs and pressure coefficient charts. By interpreting and processing the recorded wind tunnel data one has to consider the shift between the pressure measurements on the lower and the upper face of the considered model, respectively 90° for the flat and the duo-pitch roof structure and 180° for the hyper roof structure. This shift results from the model fabrication, where the two considered adjacent quarters, or halves, are equipped with pressure taps on the upper and the lower face respectively. Consequently, in order to calculate the net acting wind pressure one should translate the lower face pressure measurements to fit the upper face pressure measurements by taking into account the bi-symmetry of the model.

All wind tunnel tests are repeated several times to show consistency in the recorded results, and to exclude potential anomalies. In order to prevent the following analysis from overloading, only a limited amount of graphs and charts is presented in the discussion of the results. Nevertheless, all the experimentally obtained graphs and charts can be found in the corresponding appendices (Appendix B & C).

At first, three manual 360° -rotation sequences are performed for each structure in order to define the most critical orientation and the required angular resolution for the discrete angle test case. These tests recording the pressure data at the upper and lower face of the roof are performed at a wind speed of 5 m/s, with a sampling frequency of 10 Hz and for a sampling length of 100 s. These parameters have been chosen to obtain a rather detailed and continuous pressure measurement while minimising the effect of turbulence during the testing procedure. Higher wind speeds and faster model rotation could cause significant turbulence and will affect the wind profile close to model. Moreover, a sufficiently large sampling frequency is required to neutralise the turbulence effects and to obtain a rather continuous measurement for all orientations during this rotation sequence. The results of these testing sequences are visualised in graphs, showing the recorded pressures in the taps at the upper and the lower face of the roof respectively. To facilitate the interpretation of the experimentally obtained pressure graphs, the orthogonal orientations and corresponding pressure tap locations are applied onto the graphs. For each test case, the experimentally obtained pressure graphs for one single rotation sequence are presented in the discussion. A larger and higher resolution variant of each graph is listed in Appendix B.

A next series of wind tunnel tests is performed for discrete angles of attack at wind speeds of 5, 10 and 15 m/s, with a sampling frequency of 10 Hz and for a sampling length of 50 s. The results from these testing sequences are transformed into pressure coefficient distribution charts that are compared to the ones presented in the Eurocode. In order to compare the experimentally obtained pressure coefficient distributions with the ones from the Eurocode, both, the overall and local pressure coefficients of EN 1991-1-4:2005 are illustrated in the analysis. The $C_{pe,10}$ - and $C_{pe,1}$ -values are considered because in fact the recorded pressures are point-measurements at taps of 1 mm in diameter, regardless they are considered to represent a larger surface area. Besides, mark that for the geometrical proportions of the distributions from the Eurocode only the horizontal dimensions are considered. Normally one has to consider the elevation height of the roof as well, but if so, the experimentally obtained pressure distributions would deviate significantly in terms of geometrical proportions of the different roof zones. To facilitate the interpretation of the experimentally obtained pressure coefficient distribution charts a colour-scale is applied, ranging from red for the more negative values to green for the more positive values. Mark that this colour-scale is referenced individually for each testing sequence, causing similar colours between different experiments to have different values. The values coloured in grey should not be considered in the interpretation of the pressure coefficient distributions, because these values are abnormal or could not be calculated. For example, the net pressure values at the corner points could not be calculated. At this position pressure taps are only located at the upper face and not at the bottom face of the roof as a consequence of the supporting column that is connected to its bottom face. All experimentally obtained pressure coefficient distribution charts are listed in Appendix C.

4.2.1 Flat roof

Flat roof part of building envelope



Model	Flat roof
Walls	Yes
Number of pressure taps	31 (16 upper + 15 lower face)
Maximal tunnel blockage	3,25%
Wind direction	0° & 90°
Flow type	Free Field
Wind velocity	5, 10 & 15 m/s
Atmospheric pressure	101942,0 ± 3,81 Pa
Relative humidity	56 ± 0,0%
Temperature	24,4 ± 0,03 °C
Air density	1,20082 kg/m ³
Number of samples	500
Sampling frequency	10 Hz
Sampling length	50 s

Table 10: Wind tunnel testing conditions – flat roof

4.2.1.1 360°-rotation

For the flat building roof, the experimentally obtained pressure graphs of a single rotation sequence are presented in Figure 36. The graphs indicate that both faces of the roof are loaded by counteracting suction during the entire rotation process. The rather high wind velocity of the air flowing over the horizontal roof generates net suction over the entire roof. The suction on the upper face is about three times larger compared to the bottom face.

Highest suction is located at the upwind side of the roof (rotation of 270° up to 360°), induced by the wind flow that accelerates and separates around the windward edges and corners. The upwind walls of the building envelope blocking the airflow force the wind over the building roof and generate rather large wake areas close to the upwind roof edges and corners. Consequently, the recorded pressures on the upper face of the roof are higher for the angles of attack where the pressure taps are located on the upwind side of the roof (rotation of 270° up to 360°) with most extreme values for a rotation of approximately 315° whereby the pressure taps are located most upwind. The smallest pressure values are recorded when those taps are located on the downwind side of the roof (rotation of 90° up to 180°). In addition one can observe higher turbulence at the upwind areas (orientation 270° up to 360°).

Besides, it is observed that the global internal pressure is rather constant over the entire lower surface of the roof implying a quite uniform and constant internal pressure, which is to be expected in an enclosed building. The calculated average internal pressure coefficients range from -0,1 to -0,2 for the 360°-rotation. Since the building envelope does not contain any dominant openings, the small pressure variations that are observed are function of the background leakage variation relative to the considered angle of attack. Generally, for a background leakage ratio (surface area of leakage in the façade under attack to the area of leakage in the other façades) larger than one, a positive internal pressure will build up, while a ratio smaller than one will result in a negative internal pressure. This phenomenon is explained by the possibility of exhausting or draining the internal air at the rear of the building. More leakage at the rear side of the building, where the external surfaces are loaded by suction as a result of the generated wake, will allow better draining of the internal air. This will reduce the accumulation of air in the building, or even result in internal under pressure if the proportion of extracted air to incoming air is larger than one.

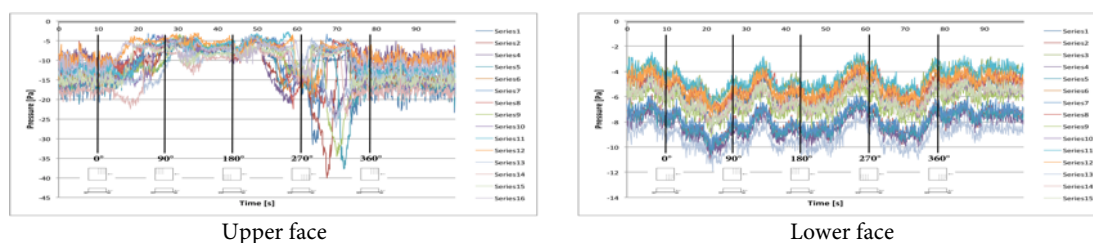


Figure 36: Wind tunnel pressure measurements – continuous rotation – flat roof

During the entire rotation process, both faces of the flat building roof are loaded by counteracting suction. The suction on the upper face is about three times larger compared to the lower face, causing the entire roof to be loaded by net suction. The external suction on the upper face is orientation depended. Largest suction and turbulence is located at the upwind side of the roof (rotation of 270° up to 360° — upper face). The global internal pressure is rather constant over the entire lower surface of the roof implying a quite uniform and constant internal pressure in the building.

Caution, while interpreting the graphs: the pressure measurements on the lower face shift -90° compared to the pressure measurements on the upper face and consider the bi-symmetry of the flat roof. (Larger resolution — Appendix B)

4.2.1.2 Discrete angles of attack

The external pressure coefficient distributions are generated for wind orientations of 0° and 90°. While interpreting the outcome, it is observed that the wind speed has a negligible influence on the generated pressure coefficient distributions. For the three investigated wind velocities of 5, 10 and 15 m/s the obtained distributions are almost identical, although slightly higher values are observed for the higher wind velocities. The rather identical values are explained by the wind speed independency of the pressure coefficients, while the slightly higher values result from the increased turbulence that is generated by higher wind speeds. Besides, it is seen that orientations of 0° and 90° give rather identical results, which was to be expected from the symmetry of the model. The small deviations that are observed can be attributed to the imperfections of the handmade test model and the slightly off axis orientations introduced by manually rotating the turntable.

By comparing the experimentally obtained external pressure coefficient distributions with the ones presented in the Eurocode for flat roofs (Figure 37), rather similar conclusions could be drawn as discussed in 2.2.5.1. The global pressure distributions of the experiments correspond well to the one presented by the Eurocode. For the main upwind area the experimentally obtained values fall within the range of overall and local pressure coefficients of the Eurocode, while for the downwind area the experimentally obtained values exceed those of the Eurocode. The wind tunnel testing shows a lower reduction of the wind velocity of the air that flows over the roof. The induced vortices, the roughness, and the viscosity and friction forces at this roof face generate a smaller boundary layer. This could possibly be assigned to the very smooth roof surface. Finally, it is observed that the upwind edge and corners areas are loaded by lower suction compared to the Eurocode, what on its turn could be explained by the rather large distance of the pressure tap locations from the edge and the detailing of the edge itself.

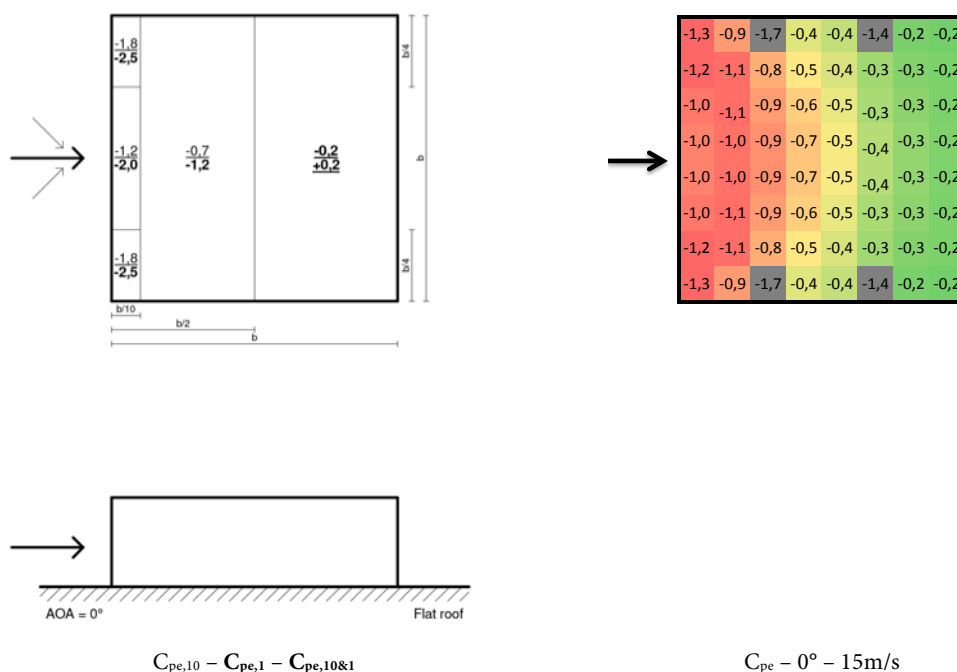


Figure 37: Analysis flat roof – external pressure coefficients
 Left: Eurocode – external pressure coefficients – flat roof
 Right: Wind tunnel measurements – flat roof

The experimentally obtained external pressure coefficient distributions for the flat building roof (right) are in good correlation to the one that is presented by the Eurocode (left). In general, the experimentally defined pressure coefficients fall within the range of overall and local pressure coefficients of the Eurocode. The local deviations such as smaller pressure coefficients near the upwind edge or larger pressure coefficients at the central area could be explained by situation specific parameters of the wind tunnel experiments. Parameters such as detailing of the edges, location of the pressure taps, surface finishing, off axis rotation, type of wind tunnel, et cetera, have significant influence on the experimental results. (All charts – Appendix C)

4.2.2 Flat canopy

Flat canopy structure



Model	Flat roof
Walls	No
Number of pressure taps	31 (16 upper + 15 lower face)
Maximal tunnel blockage	0,95%
Wind direction	0° & 45°
Flow type	Free Field
Wind velocity	15 m/s
Atmospheric pressure	101942,0 ± 3,81 Pa
Relative humidity	56 ± 0,0%
Temperature	24,4 ± 0,03 °C
Air density	1,20082 kg/m ³
Number of samples	500
Sampling frequency	10 Hz
Sampling length	50 s

Table 11: Wind tunnel testing conditions – flat canopy

4.2.2.1 360°-rotation

For the flat canopy roof, the experimentally obtained pressure graphs of a single rotation sequence are presented in Figure 38. The absence of walls allows the wind not only to flow over but also to flow underneath the flat canopy roof. Consequently, the wind interacts directly onto the upper and the lower face of the canopy, where the wind could only interact directly onto the upper face of the building roof. The graphs indicate that also for this case both faces of the roof are loaded by counteracting suction during the entire rotation process. The wind pressure acting on the upper face of the flat canopy roof has reduced by a factor of three compared to the flat building roof of section 4.2.1. This phenomenon is explained by the absence of walls. The amount of blocked air is reduced drastically by removing the walls, causing a very small acceleration and separation of the wind that is forced around the thin roof edge. The reduced velocity of the air flowing over the horizontal roof face results in very small suction values. Moreover, the redistribution is quite equally to the upper and lower side of the canopy, resulting in very similar levels of counteracting suction on both faces of the flat canopy roof. However, the lower face tends to be vulnerable for higher turbulence and slightly smaller suction what can be explained by the restricted opening under the canopy compared to the free field above. Furthermore, the graphs show that the pressure barely changes during the rotation sequence, which indicates the rather identical wind pressures acting on the upwind and downwind areas except for some local extreme values recorded at the upwind edges of the upper face (rotation of 270° up to 360°).

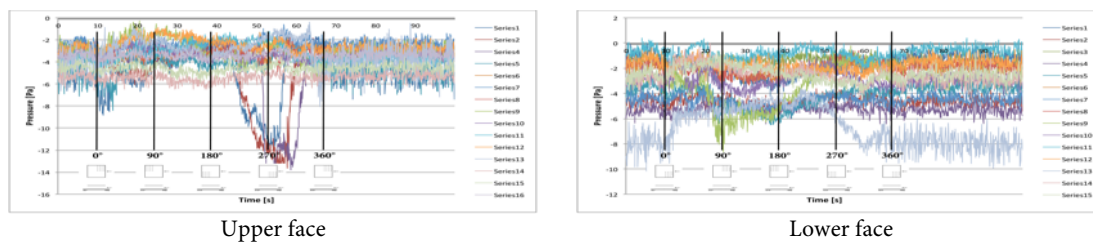


Figure 38: Wind tunnel pressure measurements – continuous rotation – flat canopy

During the entire rotation process, both faces of the flat canopy roof are loaded by similar counteracting suction levels. The absence of walls allows the wind to interact directly onto the upper and the lower face of the canopy. The reduced amount of blocked air that is redirected over and under the flat canopy roof results in very low suction values on both faces of the roof. Locally some extreme suction values are recorded at the upwind edges of the upper face (rotation of 270° up to 360° — upper face), while the lower face tends to be vulnerable for higher turbulence and slightly smaller suction as a result of the restricted opening under the canopy. Compared to the flat building roof of section 4.2.1 the wind pressure acting on the upper face of the flat canopy roof has reduced by a factor of three.

Caution, while interpreting the graphs: the pressure measurements on the lower face shift -90° compared to the pressure measurements on the upper face and consider the bi-symmetry of the flat canopy. (Larger resolution — Appendix B)

4.2.2.2 Discrete angles of attack

The net pressure coefficient distributions are generated for wind orientations of 0° and 45°. While interpreting the outcome, it is observed that the pressure coefficients of both distributions have the same magnitude. Notwithstanding the 45° orientation, with a corner under direct wind attack, shows slightly higher suction values. This could be attributed to a complex interplay of improved aerodynamics of the structure relative to the wind and imperfections in the handmade model. Besides, results show that the edges are loaded by little higher suction, especially close to the upwind edge, while central area of the roof is almost unloaded with pressure coefficients close to 0. The wind accelerates and separates slightly while it is forced over and under the roof edge, and slows down towards the central and rear areas as a result of the boundary layer that builds up by interaction with the roof face. This could be expected by the similarity between a flat canopy roof and a flat plate that is placed along the wind flow.

By comparing the experimentally obtained net pressure coefficient distributions with the ones presented in the Eurocode for monopitch canopies with an inclination of 0° (Figure 39), rather similar conclusions could be drawn as discussed in 2.2.6.1 by considering the variations and differences. The edge areas are loaded almost twice as heavily compared to the central areas for both cases, but the magnitude of the experimentally obtained net pressure coefficients is significantly smaller compared to those presented by the Eurocode. This difference could be attributed to a complex interplay of structural thickness, roof inclination, elevation height, et cetera. Increasing the structural thickness of the roof will result in higher suction values. The increased accumulation zone of the blocking upwind roof edge, could lead to more acceleration and separation of the air flowing over the upper and lower roof faces. The inclination of the roof relative to the wind angle of attack has a significant influence on the aerodynamics of the roof. Depending on the inclination rather larger or smaller wake zones will be generated at the upper and lower face of the roof causing differential suction on both faces. In analogy to the discussion in 2.2.6.1, a positive inclination will result in rather net downward acting pressure, while a negative inclination will result in net upward acting suction. In addition, the differential pressure on both faces is highly depended on the elevation height of the canopy roof itself. The lower the height of the roof the larger the pressure difference will be. Lower canopy roofs allow less wind to flow underneath the roof and on top of that with a reduced wind velocity as a result of the interacting boundary layers building up upwards from the ground and downwards from the lower face of the roof. The lower wind speed under the canopy would result on its turn in lower suction on the lower face of the canopy.

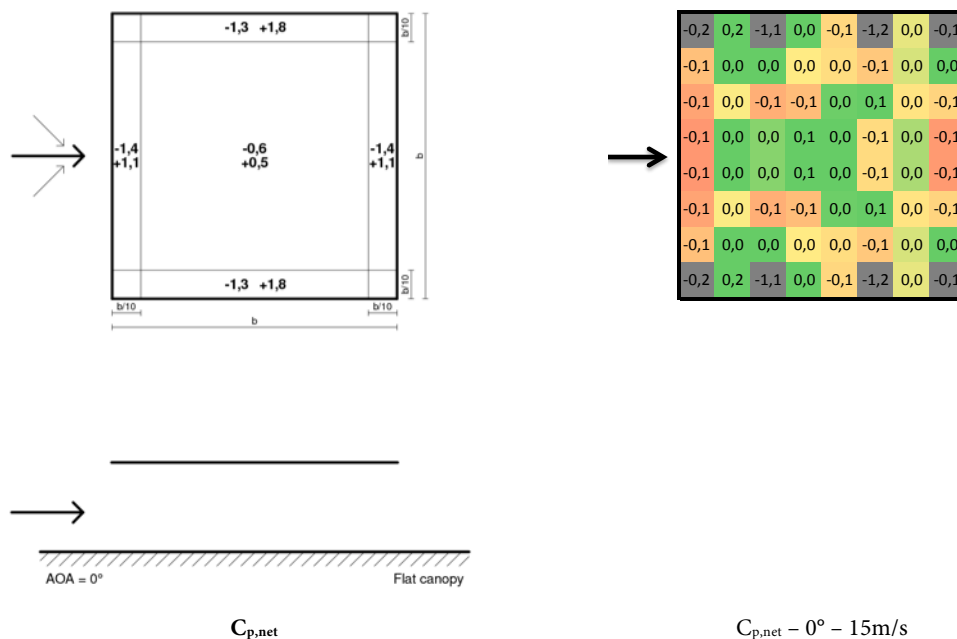


Figure 39: Analysis flat canopy – net pressure coefficients
 Left: Eurocode – net pressure coefficients – flat canopy
 Right: Wind tunnel measurements – flat canopy

The experimentally obtained net pressure coefficients for the flat canopy roof (right) are significantly smaller compared to the ones that are presented by the Eurocode (left). This could be attributed to a complex interplay of structural thickness, roof inclination, elevation height, et cetera (situation specific parameters of the wind tunnel experiments). The flat canopy roof could be seen as a flat plate that is placed along the wind flow. (All charts — Appendix C)

4.2.3 Duo-pitch roof

Duo-pitch roof part of building envelope



Model	Duo-pitch roof
Walls	Yes
Number of pressure taps	31 (16 upper + 15 lower face)
Maximal tunnel blockage	5,33%
Wind direction	0° & 90°
Flow type	Free Field
Wind velocity	5, 10 & 15 m/s
Atmospheric pressure	102147,8 ± 1,74 Pa
Relative humidity	56 ± 0,0%
Temperature	24,5 ± 0,0 °C
Air density	1,20323 kg/m ³
Number of samples	500
Sampling frequency	10 Hz
Sampling length	50 s

Table 12: Wind tunnel testing conditions – duo-pitch roof with pitch inclinations of 30°

4.2.3.1 360°-rotation

For the duo-pitch building roof, the experimentally obtained pressure graphs of a single rotation sequence are presented in Figure 40. The graphs clearly illustrate the orientation dependency of the pressure measurements during the rotation process, especially for the upper face that is subjected to direct interaction of the wind. During the rotation sequence the upper face of the roof is loaded by significantly variable pressure and suction values, while the lower face is always loaded by a similar magnitude of suction.

The external pressure distribution over a duo-pitch building roof can be assessed mainly by two cases: with the ridge perpendicular and with the ridge parallel to the wind. When the ridge is oriented perpendicular to the wind angle of attack, the duo-pitch roof can be seen as two intersecting monopitch roofs, by taking into account the influence of one onto another. The upwind pitch that blocks the airflow (rotation of 0° and 360°) is loaded by positive pressure and suction, while the downwind pitch at the rear side (rotation of 180°) is loaded completely by suction. The highest positive pressure values are observed for a rotation of approximately 315° whereby the pressure taps are located most upwind. For the parallel orientation (rotation of 90° and 270°) the entire roof is loaded by suction, with similar characteristics as discussed for enclosed flat building roofs. Most extreme suction values are observed for an orientation of approximately 270°, whereby the pressure taps are located at the upwind side of the roof. Finally, one can observe highest turbulence at the upwind areas (rotation of 270° up to 360°).

For the recorded internal pressures similar conclusions can be drawn as for the enclosed flat roof structure. The calculated average internal pressure coefficients range from -0,2 to -0,3 for the 360°-rotation, with a quite uniform and constant distribution over the entire lower surface of the roof. The variations are function of the differential background leakage ratio relative to the considered angle of attack. The lowest under pressure is observed when the ridge is oriented parallel to the wind direction. For this orientation is the background leakage ratio largest but still smaller than one (illustrated by the two peaks in the graph with small negative pressure values).

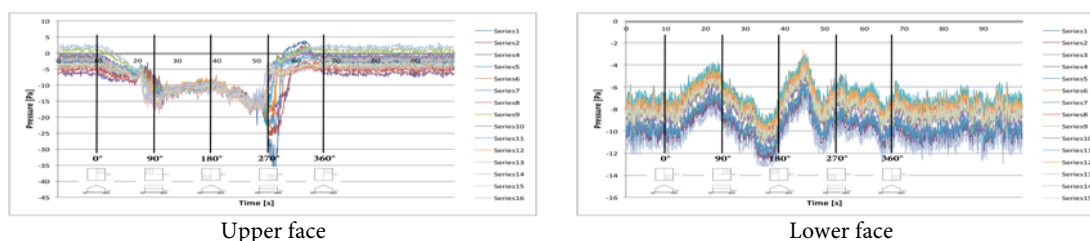


Figure 40: Wind tunnel pressure measurements – continuous rotation – duo-pitch roof with pitch inclinations of 30°

During the rotation process, both faces of the duo-pitch building roof are mainly loaded by suction, except for some small pressure values locally on the upper face. The external pressure measurements on the upper face are orientation depended, while the lower face is always loaded by a similar magnitude of suction. Largest pressure coefficients and turbulence is located at the upwind side of the roof (rotation of 270° up to 360° — upper face). The internal pressure is rather constant over the entire lower surface of the roof. The small variations are function of the differential background leakage relative to the considered angle of attack (peaks for parallel orientations — lower face).

Caution, while interpreting the graphs: the pressure measurements on the lower face shift -90° compared to the pressure measurements on the upper face and consider the bi-symmetry of the duo-pitch roof. (Larger resolution — Appendix B)

4.2.3.2 Discrete angles of attack

The external pressure coefficient distributions are generated for wind orientations of 0° and 90° . The wind speed independency of the pressure coefficients is illustrated by the almost identical pressure distributions that are obtained for the investigated wind velocities of 5, 10 and 15 m/s. Although, slightly higher values are observed for the higher wind velocities, resulting from the increased turbulence that is generated at this wind speeds. As earlier mentioned, the wind loading on duo-pitch roofs can be mainly assessed by two cases, respectively with the ridge perpendicular and parallel to the wind angle of attack.

By comparing the experimentally obtained external pressure coefficient distributions with the ones presented in the Eurocode for duo-pitch roofs with an inclination of 30° (Figure 41 and Figure 42), rather similar conclusions could be drawn as discussed in 2.2.5.3 by considering the 30° inclination. For each of the considered cases, the global pressure distributions of the experiments correspond well to the ones presented by the Eurocode.

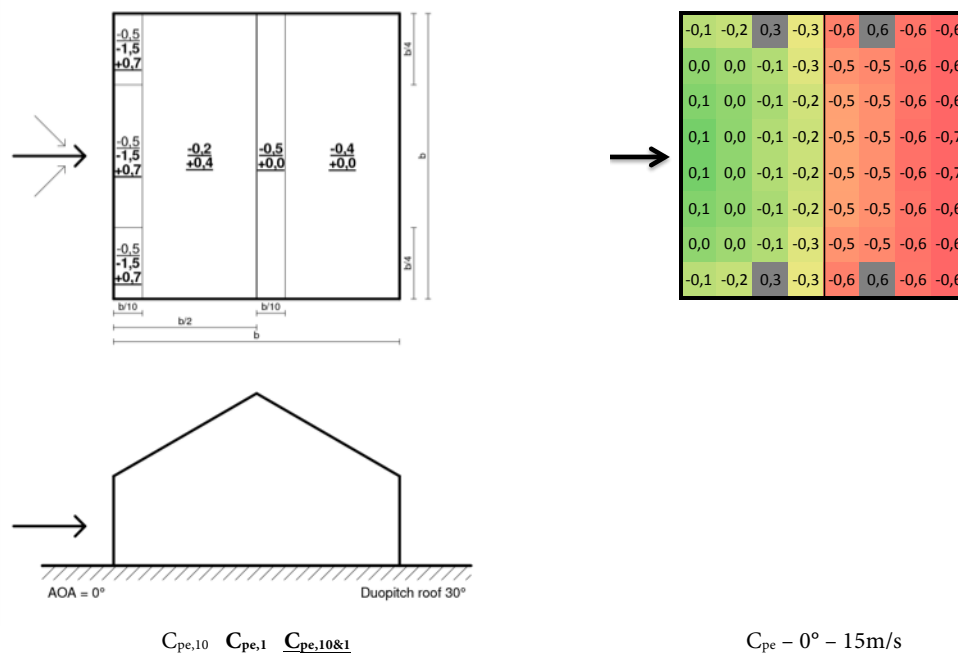


Figure 41: Analysis duo-pitch roof – external pressure coefficients for perpendicular angle of attack

Left: Eurocode – external pressure coefficients – duo-pitch roof with pitch inclinations of 30°

Right: Wind tunnel measurements – duo-pitch roof with pitch inclinations of 30°

The experimentally obtained external pressure coefficient distributions for the perpendicular orientation of the duo-pitch building roof (right) are in good correlation to the one that is presented by the Eurocode (left). The experimentally defined pressure coefficients for the upwind pitch fall within the range of overall and local pressure coefficients of the Eurocode, but for the downwind pitch the values of the Eurocode are exceeded. The small positive downward acting pressure at the upwind edge transforms into suction that builds up towards the ridge. Just behind the ridge suction increases instantaneously, followed by increasing suction values where the Eurocode prescribes a decrease of suction.

While interpreting the results one has to be aware of the situation specific parameters of the wind tunnel experiments, because these parameters will have significant influence on the experimental results. (All charts — Appendix C)

When the ridge is oriented perpendicular to the wind angle of attack (Figure 41), the experimentally obtained pressure coefficients for the upwind pitch fall within the range of overall and local pressure coefficients of the Eurocode, while for the downwind pitch the experimentally obtained values exceed those of the Eurocode. The approaching wind is blocked at the front façade and redirected over the roof. Despite the acceleration of the wind that flows around the roof edge, a small positive downward pressure loads the zones of the roof close to the upwind edge. The wind then accelerates as a result of the Venturi effect over the positively inclined upwind pitch of the roof. The increasing wind speed causes the slight positive pressure near the edge to diminish and transform into suction that builds up towards the ridge of the roof. The wind that flows around the ridge separates from the roof and creates a wake zone above the downwind pitch of the roof. This wake results in a drastic and instantaneous increase (by doubling) of suction just behind the ridge. Up to here, the experimentally obtained pressure coefficients fall within the ranges defined by the Eurocode. But then from the ridge towards the downwind edge of the roof

increasing suction is observed, where the Eurocode prescribes a decrease of suction towards the rear edge of the downwind pitch. Beside it is observed that the experimentally obtained pressure coefficients near the upwind edge are significantly smaller compared to the coefficients presented by the Eurocode, which could be explained by the rather large distance of the pressure tap locations from the roof edge and the detailing of the edge itself. Closer to the edge possibly larger pressure coefficients could be observed. Furthermore, close to the parallel edges higher suction values are observed in comparison to the more central areas. The wind flowing next to parallel building walls contributes to the suction locally at these edges. Mark that by considering the results of the duo-pitch canopy presented in section 4.2.4, skew winds could give rise to pressure distributions in closer accordance with the pressure coefficient distributions presented by the Eurocode. Skew winds could induce more extreme wind loads locally near the edges and the ridge and could give rise to decreasing suction values towards the rear edge of the downwind pitch. These phenomena could occur as a consequence of the shape and the aerodynamics of the duo-pitch roof relative to a changing angle of attack.

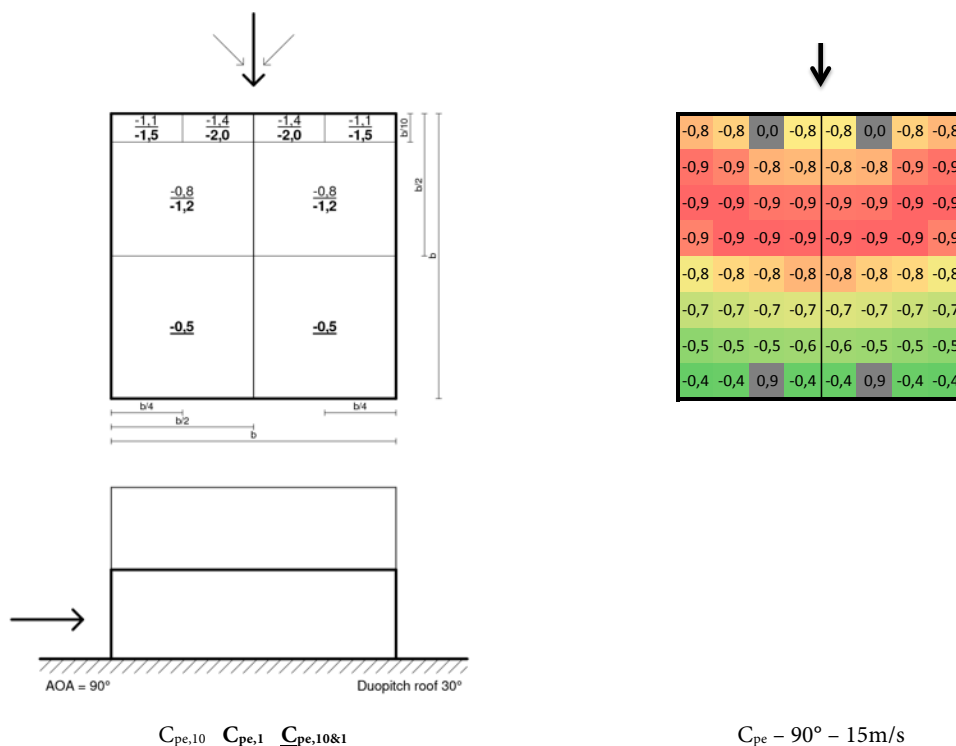


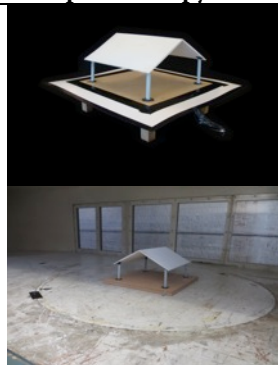
Figure 42: Analysis duo-pitch roof – external pressure coefficients for parallel angle of attack
 Left: Eurocode – external pressure coefficients – duo-pitch roof with pitch inclinations of 30°
 Right: Wind tunnel measurements – duo-pitch roof with pitch inclinations of 30°

The experimentally obtained external pressure coefficient distributions for the parallel orientation of the duo-pitch building roof (right) are in good correlation to the one that is presented by the Eurocode (left). The entire roof is loaded by suction, with decreasing values downwind. The reduction of suction is lower for the experimentally obtained results, what could be attributed to the very smooth roof surface. The smaller suction values close to the upwind edge are function of the situation specific parameters of the wind tunnel experiments. (All charts — Appendix C)

When the ridge is oriented parallel to the wind angle of attack (Figure 42), the entire roof is loaded by suction, with decreasing values downwind. The Eurocode presents a rather similar pressure coefficient distribution as observed for a flat roof, which is to be expected by the aerodynamics of the roof relative to the wind angle of attack, and is confirmed by the experimentally obtained results. The experimentally obtained pressure coefficients for the main upwind zone fall within the range of overall and local pressure coefficients of the Eurocode, while for the downwind zone the experimentally obtained values slightly exceed those of the Eurocode. Consequently rather similar conclusions could be drawn as for the results of the flat roof in section 4.2.1. Considering the recorded wind tunnel data, a lower reduction of suction is observed towards the downwind areas at the rear of the roof, what could be attributed to the very smooth roof surface that results in its turn in lower viscosity and friction forces and consequently a lower reduction of wind velocity at the roof surface. Finally, also for this case, smaller suction values are observed close to the upwind edge and corners areas what could be attributed once again to the rather large distance of the pressure tap locations from the edge and the detailing of the edge itself.

4.2.4 Duo-pitch canopy

Duo-pitch canopy structure



Model	Duo-pitch roof
Walls	No
Number of pressure taps	31 (16 upper + 15 lower face)
Maximal tunnel blockage	3,12%
Wind direction	0°, 30°, 45°, 60° & 90°
Flow type	Free Field
Wind velocity	5, 10 & 15 m/s
Atmospheric pressure	100039,3 ± 1,89 Pa
Relative humidity	58 ± 0,0%
Temperature	20,03 ± 0,02 °C
Air density	1,19388 kg/m ³
Number of samples	500
Sampling frequency	10 Hz
Sampling length	50 s

Table 13: Wind tunnel testing conditions – duo-pitch canopy with pitch inclinations of 30°

4.2.4.1 360°-rotation

For the duo-pitch canopy roof, the experimentally obtained pressure graphs of a single rotation sequence are presented in Figure 43. For the duo-pitch open canopy roof structure, combined conclusions can be drawn as for the duo-pitch building roof of section 4.2.3 and the flat open canopy structure of section 4.2.2. The graphs clearly illustrate the orientation dependency of the pressure measurements for both, the upper and the lower face of the canopy roof. The recorded pressures depend on the degree of blockage accompanying the orientation of the duo-pitch canopy roof relative to the wind angle of attack. Besides, it is observed that during the rotation process the lower face pressure measurements turn inversely compared to the upper face pressure measurements. This phenomenon is a natural consequence of the duo-pitch roof shape, there the opposing faces of each inclined pitch have a supplemental orientation relative to the wind angle of attack.

The absence of walls reduces the degree of blockage drastically, allowing the wind not only to flow over but also underneath the roof and interact directly onto its lower face as well. The reduced amount of blocked air is redirected to the upper and lower face, causing less acceleration and separation of the wind flow. Compared to the duo-pitch building roof of section 4.2.3, the recorded wind pressure on the upper face of the canopy roof is affected up to a certain extend. For the ridge perpendicular to the wind angle of attack the pressure on the upwind pitch (rotation of 0° up to 45° and 315° up to 360°) is about four times larger for positive downward acting pressure and about one and a half times smaller for suction values, while for the downwind pitch (rotation of 135° up to 225°) pressure values nearly changed. For the parallel orientation (rotation of 45° up to 135° and 225° up to 315°) the suction is reduced by a factor of four, except for the upwind edge where suction remained more or less constant. Beside, most extreme pressure values are observed under different orientation compared to the enclosed state. Highest positive pressure values are observed for a rotation of approximately 0° or 360° where it was before approximately 315°, and highest suction is now observed for an orientation of approximately 225° where it was before approximately 270°. Furthermore, it is clear to see that in analogy to the observed pressure changes, turbulence has changed as well. For the perpendicular orientations turbulence has increased for the upwind zones (rotation of 0° up to 45° and 315° up to 360°), while it stayed constant for the downwind zones (rotation of 135° up to 225°). For the parallel orientations (rotation of 45° up to 135° and 225° up to 315°) turbulence has decreased over the entire roof, except locally at the upwind edge (rotation 225° up to 315°).

The established pressure measurements on the lower face of the duo-pitch canopy roof clearly indicate their orientation dependency and their inverse development compared to the recorded upper face pressures. For the perpendicular orientation highest pressure and suction values are recorded. The upwind pitch blocks and redirects the incoming air mainly over the roof, causing a wake zone to develop in the attic space of the roof. Suction is observed on the lower face of the upwind pitch (rotation of 0° up to 45° and 315° up to 360°), with most extreme values locally at orientations close to 0° or 360°. Positive upward acting pressure is observed on the downwind pitch (rotation of 135° up to 225°), with highest values close to but not at an orientation of 180°. For these orientations the wind blows directly onto the lower face of the downwind pitch, causing positive pressure to develop. At an orientation of 180°, the wind is mainly blocked at the upwind pitch and redirected over the roof, wherefore the wind is solely able to interact with the lower face of the downwind pitch by the suction that is induced by the wake in the attic space of the roof (illustrated by the depression in the graph). For the parallel orientation (rotation of 45° up to 135° and 225° up to 315°) rather low suction values are observed, which was to be expected by the large

similarity between the duo-pitch canopy and the flat canopy for this orientation. Both intersecting pitches of the duo-pitch canopy are aligned along the wind direction causing very little blockage at their upwind edges, and to behave more or less as a flat plate that is placed along the wind flow.

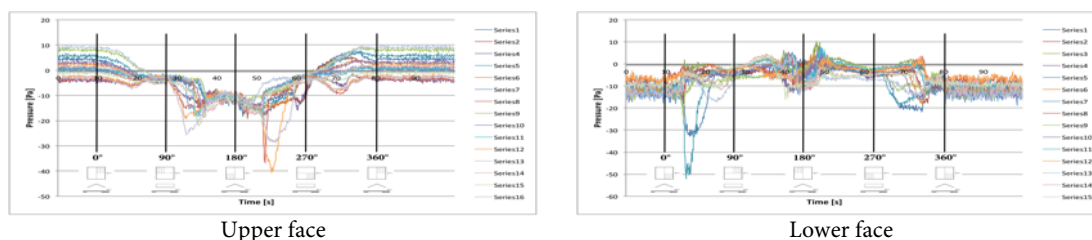


Figure 43: Wind tunnel pressure measurements – continuous rotation – duo-pitch canopy with pitch inclinations of 30°

During the rotation process, both faces of the duo-pitch canopy roof are loaded by variable pressure and suction. Moreover, the lower face pressure measurements turn inversely compared to the upper face pressure measurements. The significantly changing pressure measurements on both faces of the roof clearly illustrate the orientation dependency of the duo-pitch canopy. Compared to the duo-pitch building roof of section 4.2.3, the magnitude of the recorded wind pressures, as well as the turbulence has changed for the upper face. Furthermore, the most extreme pressure and turbulence values have shifted for 45° as a result of the more complex aerodynamics of the open duo-pitch canopy.

Caution, while interpreting the graphs: the pressure measurements on the lower face shift -90° compared to the pressure measurements on the upper face and consider the bi-symmetry of the duo-pitch canopy. (Larger resolution — Appendix B)

4.2.4.2 Discrete angles of attack

The net pressure coefficient distributions for the duo-pitch canopy roof are generated for wind orientations of 0°, 30°, 45°, 60° and 90°. The wind speed independency of the pressure coefficient distributions is also observed for this test case. Intuitively, a duo-pitch canopy is mainly assessed with the ridge perpendicular and parallel to the wind angle of attack, in analogy to the assessment of duo-pitch building roofs. Nevertheless, the Eurocode considers only one case for duo-pitch canopies by taking into account all maximal pressure and suction values of any possible orientation. Furthermore, the Eurocode prescribes a total of six load cases that have to be considered for the wind design of duo-pitch canopy roofs.

The sequence of experimentally obtained net pressure coefficient distributions for wind orientations ranging between 0° and 90° is presented in Figure 44. The aerodynamics and thus the orientation of the duo-pitch canopy roof relative to the wind angle of attack has a significant influence on the pressure distributions. Most extreme pressure coefficients are observed locally at different roof zones for different orientations. A clear relationship between the increment in orientation and the shift of these extreme coefficients is observed. For the perpendicular orientation the central parts of both pitches are loaded higher than the zones near the parallel edges. For the skew orientations rather extreme values are observed near the edges and the ridge, with lower values at the central area of each pitch. For the parallel orientation rather low suction values are observed over the entire roof, with larger values near the upwind edge. This last pressure coefficient distribution with the duo-pitch canopy parallel to the wind is in close analogy to the experimentally obtained pressure coefficient distributions for the flat canopy roof of section 4.2.2.

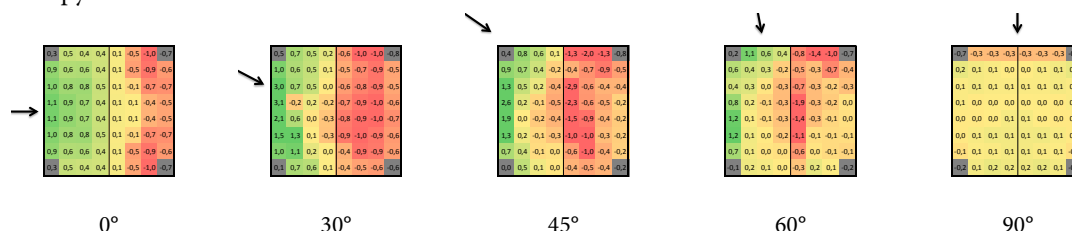


Figure 44: Wind tunnel net pressure coefficient distributions – discrete angles – duo-pitch canopy with pitch inclinations of 30°

The aerodynamics and thus orientation of the duo-pitch canopy roof relative to the wind angle of attack has a significant influence on the net pressure distributions. Most extreme pressure coefficients are observed locally at different zones for different orientations. A clear relationship between the increment in orientation and the shift of the pressure coefficient distribution is recorded. However, for the duo-pitch canopy roof most extreme net pressure coefficients are observed for the skew orientations (rotation of 30°, 45° and 60°), while lowest pressure coefficients are observed for the parallel orientation (rotation of 90°) and intermediate values for the perpendicular orientation (rotation of 0°).

Furthermore, the position of the pressure taps and the orientation of the model relative to the wind angle of attack show significant influence on the recorded pressures. Different pressures are recorded at the same tap for different orientations, or between neighbouring taps for the same orientation. Consequently, moving a pressure tap a few mm or rotating the model a few degrees could give rise to significant changes in the pressure measurements, which cannot be neglected and should be considered while interpreting the results.

By comparing the experimentally obtained net pressure coefficient distributions with the one presented in the Eurocode for duo-pitch canopies with an inclination of 30° (Figure 45), rather similar conclusions could be drawn as discussed in 2.2.6.2 by considering the 30° inclination. By taking into account the local maxima over all orientations, the global net pressure distribution of the experiments correspond well to the one presented by the Eurocode. The maximal values covering nearly all roof zones are recorded for a combination of perpendicular and skew winds, but most extreme values are observed locally for the skew orientations.

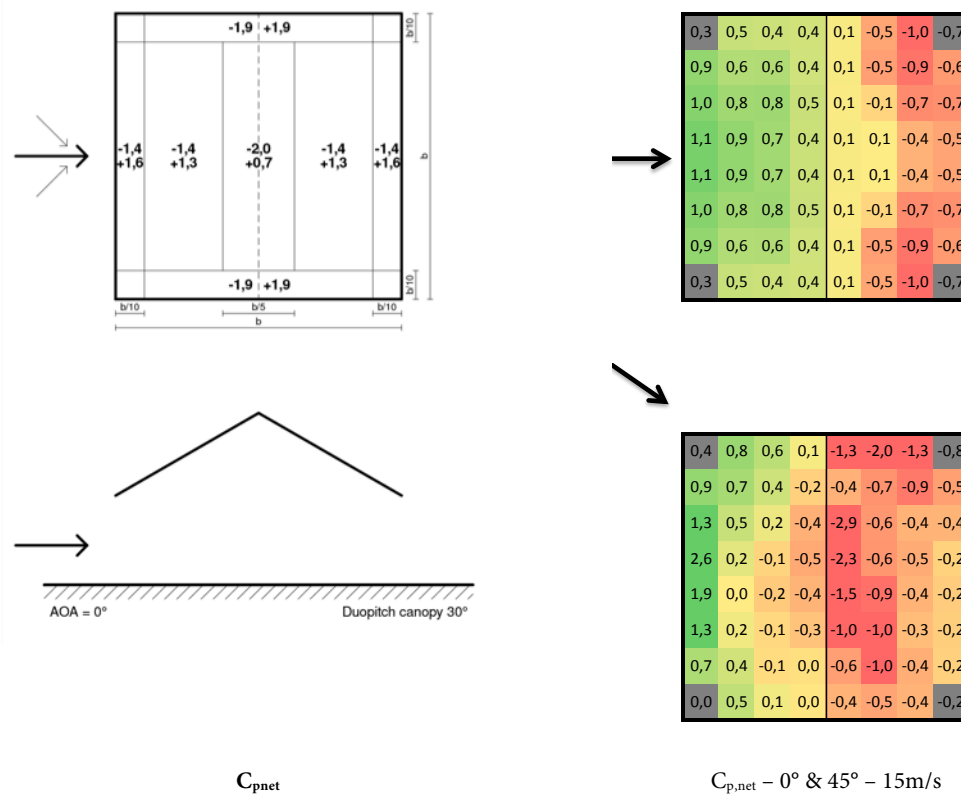


Figure 45: Analysis duo-pitch canopy – net pressure coefficients for parallel and perpendicular angle of attack
 Left: Eurocode – net pressure coefficients – duo-pitch canopy with pitch inclinations of 30°
 Right: Wind tunnel measurements – duo-pitch canopy with pitch inclinations of 30°

The experimentally obtained net pressure coefficient distributions for the duo-pitch canopy roof (right) are in good correlation to the one that is presented by the Eurocode (left). The experimentally defined pressure coefficients for the central zones of the upwind and the downwind pitch fall within the range of overall and local pressure coefficients of the Eurocode, but for the edge and the ridge zones (skew winds) the values of the Eurocode are exceeded locally. Most extreme pressure coefficients are observed for skew orientations, with a large variation of pressure and suction over each pitch of the duo-pitch canopy. (All charts — Appendix C)

The experimentally obtained pressure coefficients for the main area of the upwind and downwind pitch fall within the range of overall and local pressure coefficients of the Eurocode, while for the edge and ridge zones the experimentally obtained values locally exceed those of the Eurocode. Furthermore, a large variation of pressure and suction is observed over each pitch of the roof, what induces significant internal forces in the duo-pitch canopy itself. The approaching wind generates a significant downward acting pressure that loads the zones of the roof close to the upwind edge. For the perpendicular orientation these values fall within the range of the Eurocode, but with almost double values they are exceeded for skew winds. The wind then accelerates towards the ridge as a result of the Venturi effect over the positively inclined upwind pitch. The increasing wind speed causes the net pressure to decrease by a factor of three for the perpendicular orientation, and causes net suction to develop for skew winds. The

wind that flows around the ridge induces a drastic and instantaneous increase of the net suction just behind the ridge. For the perpendicular orientation this increase is mainly attributed to the wind that separates from the roof and the wake zone above the downwind pitch. For skew winds the increase of net suction is significantly larger and exceeds the values of the Eurocode. This significant increase of net suction is caused by the additional contribution of the upward acting pressure, that develops from the direct interaction of the wind onto the lower face of the downwind pitch. Up to here, the main concepts are rather similar for the perpendicular and the skew orientations, but a significant difference is observed from the ridge towards the rear edge of the downwind pitch. For the perpendicular winds an increase of suction is recorded in analogy to the results of the duo-pitch building roof of section 4.2.3, while for skew winds a decrease of suction is observed. This phenomenon could be explained by the complex aerodynamics of the duo-pitch canopy relative to the wind angle of attack. The generated wake above the downwind pitch is the determining factor for the perpendicular orientation and causes the net suction to develop. For the skew orientation, the wind accelerates over the lower face of the downwind pitch by the present Venturi effect and causes the net suction to develop further.

Finally, it is important to mark that the experimentally obtained pressure coefficient distributions have to be considered as specific test cases. While interpreting the results, one has to consider a complex interplay of the situation specific parameters of the wind tunnel experiments. Parameters such as locations and the amount of the pressure taps, imperfections in the handmade model, surface finishing of the model, detailing of the edges and the ridge, slightly off axis orientations, type of wind tunnel, et cetera. These situation specific parameters have significant influence on the experimentally obtained results and could explain differences in the results between several test cases and between experiments and literature. Consequently, a small variation of one of the situation specific parameters could result in significant changes of the experimental results.

4.2.4.3 Discrete angles of attack – Free flow field

The duo-pitch canopy roof is also tested in a higher section of the wind tunnel for wind orientations of 0° and 90° at a wind speed of 15 m/s. This additional experiment is performed to check the possible influence of the intrinsic boundary layer of the wind tunnel, which could cause a lower wind velocity at the bottom face of the canopy roof compared to its upper face. The model is stated on four additional wooden columns of 150 mm high, to be sure that the entire roof structure is elevated in the free flow field of the test section. Furthermore, an aerodynamic wing shaped platform is attached around the wooden base plate to minimise the distortion of the wind flow and the measurements as much as possible (Figure 46).



Duo-pitch canopy placed directly onto the turntable of the wind tunnel (boundary layer test case; section 4.2.4.1 and 4.2.4.2)



Duo-pitch canopy elevated on four columns of 150 mm; addition of an aerodynamic wing (free flow field test case)

Figure 46: Duo-pitch canopy wind tunnel model – boundary layer and free flow field test case

The recorded wind tunnel data for this higher position verified the expected influence of the boundary that is generated close to the bottom surface of the wind tunnel. If a fully open canopy is placed in the free flow field of the wind tunnel, differential wind speed of air flowing above and underneath the canopy roof is solely attributed to the aerodynamics of the roof and especially to the aerodynamics of the upwind edge that forces the approaching wind over and under the roof. If the canopy is placed in the boundary layer of the wind tunnel, the differential wind speed is also affected by the presence of this boundary layer. The with the height increasing wind velocity of this boundary layer results in a lower wind speed flowing under the canopy, what on its turn reduces the wind loads on the lower face of the canopy roof. This phenomenon is observed while comparing the experimentally obtained pressure coefficient distributions for the higher position (in the free flow field of the wind tunnel) with the ones of section 4.2.4.2 (in the boundary layer of the wind tunnel) (Figure 47).

For the parallel orientation nearly identical net and external pressure coefficient distributions are observed for the higher and the lower test position. For this parallel orientation, the duo-pitch canopy roof could be considered as a thin plate that is placed along the wind flow. The very low thickness of the canopy roof results in rather similar wind speeds at the upper and lower face of the canopy, regardless the considered elevation height of the model (located within the boundary layer or not). The with the height increasing wind velocity of the boundary layer is not observed for this very small thickness of the canopy roof. Consequently, the recorded wind pressures are solely function of the aerodynamics of the roof and especially depending on the detailing of the upwind edge.

For the perpendicular orientation on the other hand, the influence of the wind tunnel boundary layer is clearly illustrated. The experimentally obtained net pressure coefficient distribution changed by altering the testing height, while the external distribution remained the same. From these results can be conclude that for the lower position, the canopy roof itself is located at the transition zone between the boundary layer and the free flow field of the wind tunnel. Accordingly, for this lower position, the wind speed under the canopy is reduced by the presence of the boundary layer. By elevating the canopy roof outside the boundary layer, the wind speed under the canopy has increased, what on its turn resulted in higher suction on the lower face of the roof. The pressure coefficients at the lower face of the roof have increased by a value of approximately 0,1. This additional suction contributes to the downward acting pressure on the upwind pitch, while it counteracts the uplifting suction on the downwind pitch. Consequently, the upwind pitch is loaded most heavily for the lower position, while the downwind pitch is loaded most heavily for the elevated position.

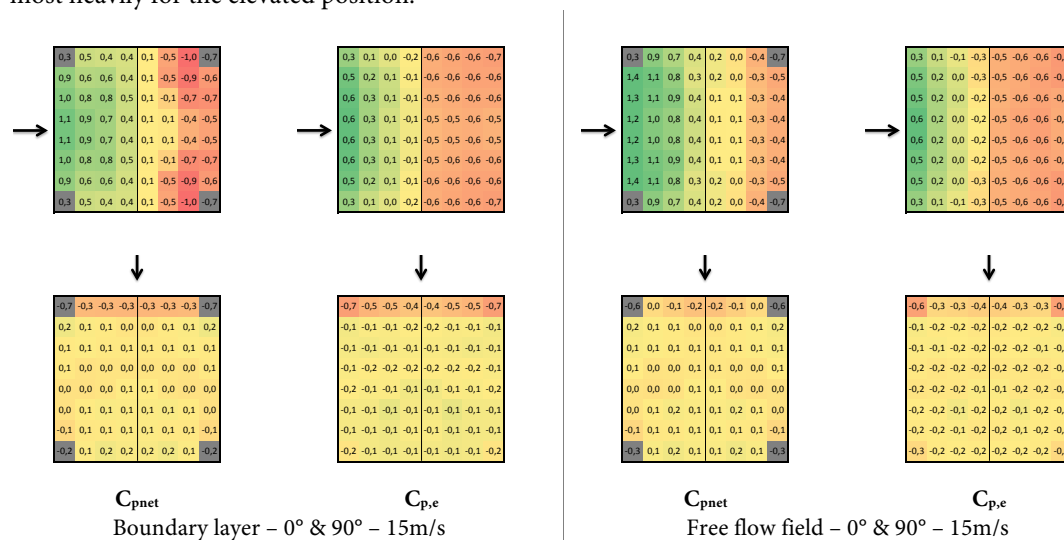


Figure 47: Analysis duo-pitch canopy – net and external pressure coefficients for parallel and perpendicular angle of attack
 Left: Wind tunnel measurements – duo-pitch canopy with pitch inclinations of 30° – boundary layer (low position; 4.2.4.2)
 Right: Wind tunnel measurements – duo-pitch canopy with pitch inclinations of 30° – free flow field (high position)

For the perpendicular orientation of the duo-pitch canopy roof (first row of charts), the influence of the wind tunnel boundary layer is clearly illustrated by altering the testing height. The net pressure coefficient distribution changed, while the external distribution remained the same. For the higher test position, the pressure coefficients on the lower face of the roof have increased by a value of approximately 0,1. Consequently, the upwind pitch is loaded most heavily for the lower position (left), while the downwind pitch is loaded most heavily for the elevated position (right). For the parallel orientation of the duo-pitch canopy (second row of charts), nearly identical net and external pressure coefficient distributions are observed for both test positions. For this orientation, the recorded wind pressures are solely function of the aerodynamics of the roof and especially depending on the detailing of the upwind edge. (All charts — Appendix C)

For the structural wind analysis of canopy roofs, the Eurocode provides net pressure coefficients that account for the simultaneous wind actions on the upper and lower face. The Eurocode and almost all other standards adopt the assumption of identical wind speeds acting on both faces of the canopy. This approach is generally accepted by the very small height difference between upper and lower face of most canopy roofs. Furthermore, it would be interesting to consider also the effect of the boundary layer for the wind design these structures. Most built canopies are land based, with a rather low elevation height of the roof. Consequently, canopy roofs tend to be loaded by lower wind speeds acting on the lower face compared to the upper face, which could cause significant changes in the net pressure distribution over the canopy roof. However, for membrane canopies, the very thin membranes and the good aerodynamics of these structures will cause rather identical wind speeds acting on the upper and lower face of the canopy roof. Although, the surrounding environment could induce significant varying wind speeds to load both faces of the canopy structures.

4.2.5 Hypar roof

Hypar roof part of building envelope



Model	Hypar roof
Walls	Yes
Number of pressure taps	62 (32 upper + 30 lower face)
Maximal tunnel blockage	3,75%
Wind direction	0° - 180°, steps of 15°
Flow type	Free Field
Wind velocity	15 m/s
Atmospheric pressure	100146,3 ± 5,66 Pa
Relative humidity	63 ± 0,1%
Temperature	21,9 ± 0,04 °C
Air density	1,18992 kg/m ³
Number of samples	500
Sampling frequency	10 Hz
Sampling length	50 s

Table 14: Wind tunnel testing conditions – hypar roof with a shape parameter of 11,3

4.2.5.1 360°-rotation

For the hypar building roof, the experimentally obtained pressure graphs of a single rotation sequence are presented in Figure 48. The graphs are subdivided for measurements near the high and the low corner to account for the locally different orientation of each quarter of the hypar roof. The hypar roof can be subdivided in four quarters by accounting for the local curvature, i.e. convex or concave. The graphs clearly illustrate the orientation dependency of the pressure measurements during the rotation process, especially for the upper face. Both faces of the roof are loaded by counteracting suction during the entire rotation process. Depending on the considered roof zone and the wind angle of attack, the inner or outer suction will be larger, resulting respectively in a net downward acting pressure or a net upward acting suction for the considered roof zone.

The external pressure distribution over a hypar building roof can be assessed mainly by two cases: with a high corner and a low corner under attack. The rather high wind velocity of the air flowing over the aerodynamic hypar roof generates suction over the entire external roof surface, regardless the wind angle of attack. The highest suction is located at the upwind side of the roof, induced by the generated wake above these zones as a result of the wind flow that accelerates and separates around the windward edges and corners. The recorded external suction on the upper face of the roof is higher for the angles of attack where the pressure taps are located on the upwind side of the roof (rotation of 0° up to 90° for the high corner and 270° up to 360° for the low corner). Most extreme values are observed for a rotation of approximately 45° and 315° whereby the pressure taps are located most upwind with respectively the high corner and the low corner under attack. Besides, it is observed that suction generally decreases towards the downwind zones as a result of the induced vortices, the roughness, and the viscosity and friction forces at the roof surface. Nevertheless, a local increase of suction is observed near the downwind low corner at a rotation of approximately 135°. This increased suction is a result of the local separation of the wind flow and the generated wake above the downwind low corner. Finally, higher turbulence is also recorded at the upwind areas with most extreme values for respectively the high and the low corner under attack (rotation of 0° up to 90° for the high corner and 270° up to 360° for the low corner).

For the recorded internal pressures similar conclusions can be drawn as for the flat and duo-pitch building roofs of sections 4.2.1 and 4.2.3. For the hypar roof, the calculated average internal pressure coefficients range from -0,1 to -0,3 for the 360°-rotation, with a rather uniform and constant distribution over the entire lower face of the roof. However, the pressure variations are more significant for different orientations compared to the flat and duo-pitch roof. These variations could be attributed to a larger differential background leakage of the different walls and to the higher testing wind speed compared to the previous cases.

The wind characteristics of the lowly curved hypar roof tend more towards those of a flat roof, which was to be expected by the very good aerodynamics of both. For a more highly curved variant on the other hand, the wind characteristics would tend more towards those of a duo-pitch roof (respectively ridge shaped when the low corner of the hypar is under attack and trough shaped when the high corner is under attack). However, one should always consider the complex interplay of the better aerodynamics of a hypar roof compared to a duo-pitch roof.

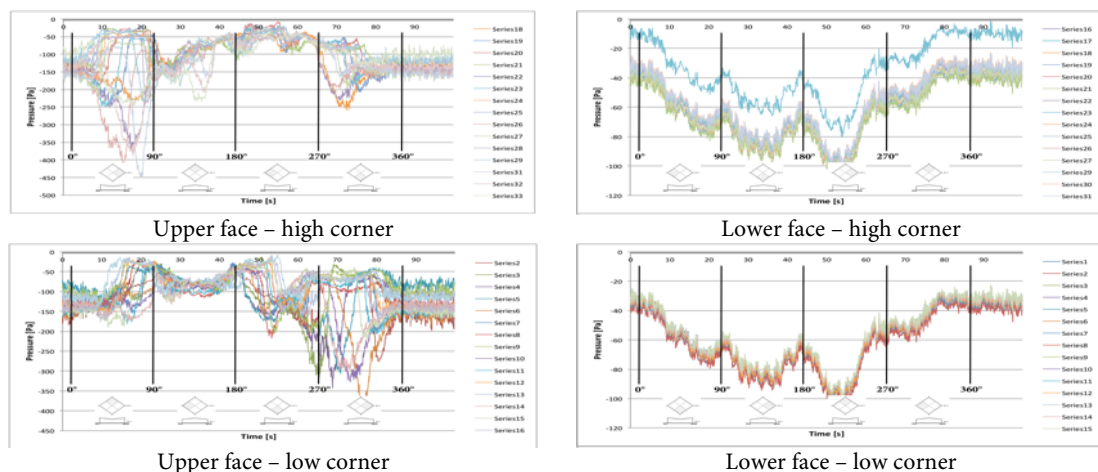


Figure 48: Wind tunnel pressure measurements – continuous rotation – hypar roof with a shape parameter of 11,3

During the rotation process, both faces of the hypar building roof are loaded by counteracting suction. Generally the suction on the upper face is larger compared to the lower face, causing the entire roof to be loaded mainly by net suction. The external suction on the upper face is orientation depended. Largest suction and turbulence is located at the upwind side of the roof (rotation of 0° up to 90° for the high corner and 270° up to 360° for the low corner — upper face). The internal pressure is rather constant over the entire lower surface of the roof. The small variations are function of the differential background leakage relative to the considered angle of attack.

Caution, while interpreting the graphs: the pressure measurements on the lower face shift -180° compared to the pressure measurements on the upper face, the high corner shifts -90° compared to the low corner, and consider the bi-symmetry of the hypar roof. (Larger resolution — Appendix B)

4.2.5.2 Discrete angles of attack

The external pressure coefficient distributions for the hypar building roof are generated for wind orientations of 0° up to 180°, with increments of 15°. The wind loading on a hypar building roof is mainly assessed by two cases, respectively with a high corner and a low corner under attack. These two cases were also identified by Otto F. in ‘Das Hängende Dach’, and considered as the two critic orientations for wind design on hypar roofs.

The sequence of experimentally obtained external pressure coefficient distributions for wind orientations ranging between 45° and 135° is presented in Figure 49. The range from 0° up to 45° and from 135° up to 180° is excluded from the sequence as a consequence of the diagonal bisymmetry of the hypar roof. The aerodynamics and thus the orientation of the hypar building roof relative to the wind angle of attack has a significant influence on the pressure distributions. Most extreme pressure coefficients are observed locally at different zones for different orientations. A clear relationship between the increment in orientation and the shift of these extreme coefficients is observed. Highest suction coefficients are observe locally close to the upwind corner and edge areas, with most extreme values for the high corner under attack (rotation of 45°) and slightly lower values for the low corner under attack (rotation of 135°). In addition it is clear to see that suction generally reduces towards the central and downwind areas of the hypar roof, except with the low corner under attack where suction remains more or less constant over the central and downwind areas.

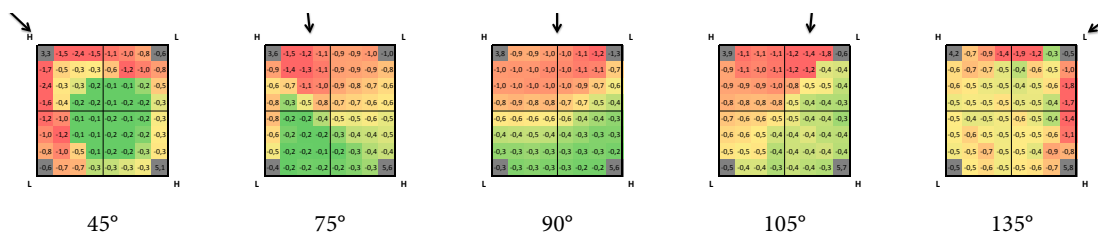


Figure 49: Wind tunnel external pressure coefficient distributions – discrete angles – hypar roof with a shape parameter of 11,3

The aerodynamics and thus orientation of the hypar building roof relative to the wind angle of attack has a significant influence on the external pressure distributions. Most extreme pressure coefficients are observed locally at different zones for different orientations. A clear relationship between the increment in orientation and the shift of the pressure coefficient distribution is recorded. Highest suction coefficients are observe locally close to the upwind corner and edge areas, with most extreme values for the high corner under attack (rotation of 45°) and slightly lower values for the low corner under attack (rotation of 135°). Furthermore, the suction generally reduces towards the central and downwind areas.

By comparing the experimentally obtained external pressure coefficient distributions with the ones presented in ‘Das Hängende Dach’ for a hypar roof with a shape parameter of 4,7 (Figure 50 and Figure 51), rather similar conclusions could be drawn as discussed in 2.2.5.4 by considering a shape parameter of 11,3 instead of 4,7. By taking into account the current shape parameter of 11,3, the global pressure distributions of the experiments correspond well to the ones presented in ‘Das Hängende Dach’. The experimentally obtained pressure coefficients exceed those of ‘Das Hängende Dach’, but the overall distribution is very similar. This phenomenon was to be expected in analogy to duo-pitch roofs that are presented in the Eurocode. For the duopitch roofs, the pressure coefficients are function of the pitch angles (with increasing suction values for decreasing inclinations), while the geometry of the pressure coefficient distribution is expected to be independent from these pitch angles. The geometrical similarity of the pressure coefficient distribution is the natural consequence of the identical building typology. For the hypar roof, the magnitude of the pressure coefficients differs as a result of the different shape parameter. In ‘Das Hängende Dach’ a hypar roof with a shape parameter of 4,7 is presented, while the wind tunnel experiments are performed on a hypar roof with a shape parameter if 11,3. Consequently, the experimentally obtained pressure coefficients are larger compared to the ones presented in ‘Das Hängende Dach’. This evolution was to be expected for the less curved hypar roof with an almost double shape parameter.

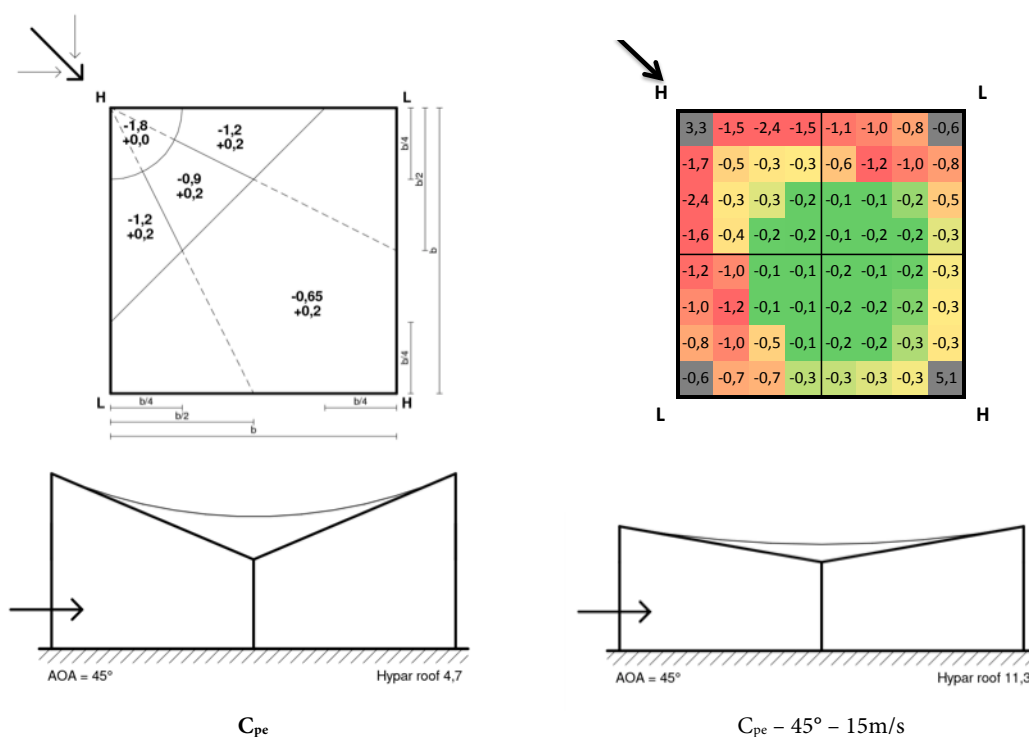


Figure 50: Analysis hypar roof – external pressure coefficients with high corner under attack
 Left: Literature - Otto, F., Das Hängende Dach, 1954 –hypar roof with a shape parameter of 4,7
 Right: Wind tunnel measurements – hypar roof with a shape parameter of 11,3

The experimentally obtained external pressure coefficient distributions for the high corner under attack of the hypar building roof (right) are in good correlation to the one that is presented in ‘Das Hängende Dach’ (left). The experimentally defined pressure coefficients are for almost each roof zone about 1,5 times larger compared to the ones presented in ‘Das Hängende Dach’. Highest suction values are recorded at the upwind high corner and edges, with decreasing values towards the downwind zones. To improve the accuracy of the simplified pressure coefficient distribution, the large downwind area could be subdivided into the three suggested subzones. (All charts – Appendix C)

With the high corner under attack (Figure 50), the experimentally obtained pressure coefficients are for almost each roof zone about 1,5 times larger compared to the ones presented in ‘Das Hängende Dach’. The radial pressure coefficient distribution (with its centre at the upwind high corner) as presented in ‘Das Hängende Dach’, illustrates the experimentally obtained prevailing suction values at the upwind corner and edges, with decreasing values towards the downwind zones. By interpreting the experimentally obtained results at the downwind zones, it would be recommended to subdivide the large downwind area into the three suggested subzones (in line with the radial pattern, illustrated by the dotted lines) to improve the accuracy of the simplified pressure coefficient distribution. The two additionally created subzones close to the low corners should be equipped with intermediate values, lower than the upwind adjacent zones and higher than the central downwind zone.

In general, the approaching wind is blocked at the upwind façades and redirected over and around the building envelope. Depending on the aerodynamics of the building relative to the wind angle of attack, this redirection will be rather over the roof or sideways around the walls. The redirected wind that accelerates around the upwind roof edge separates from the roof and causes suction to develop close to the upwind edges and corners. Most extreme suction values are observed for the high corner under attack, as a result of the local orientation of the roof and the larger amount of blocked air that is redirected over the roof. Close to the high corner, the normal on the external roof surface is locally orientated rather along the wind flow, and the walls are here locally higher, causing more of the approaching wind to be blocked. Consequently, larger separation of the wind and thus a larger wake zone are induced, resulting in higher suction close to the upwind high corner of the roof. Then suction decreases towards the central and downwind areas of the roof due to the reduced wind speed, as result of the induced vortices, the roughness, and the viscosity and friction forces at the roof surface. Besides, one should consider the local inclination of the roof surface towards the downwind high corner, because a possible increase of wind speed and suction could be induced by the Venturi effect. However, for this case, the reduction in wind speed is mainly larger than the contribution of the Venturi effect. However, slightly higher suction values are observed locally at the downwind edges, which could be attributed to a complex interplay of the downwind aerodynamics of the building relative to wind angle of attack.

For highly curved hypar roofs with a very small shape parameter, the roof could be loaded by upward acting suction at the upwind zones and by downward acting pressure at the downwind zones (cfr. trough shaped duo-pitch roof). The downward acting pressure could develop at the downwind areas as a result of the locally positive inclination of the roof close to the high corner. However, the differential pressure over the main upwind and downwind areas is limited by the good aerodynamics of the hypar roof relative to the wind angle of attack.

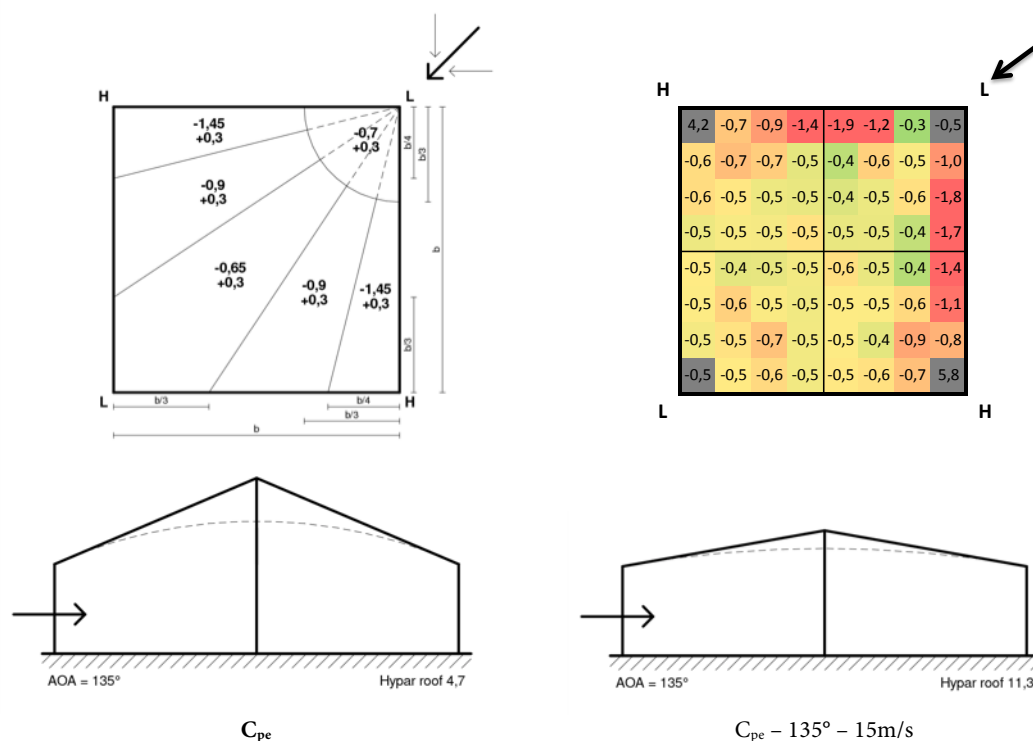


Figure 51: Analysis hypar roof – external pressure coefficients with low corner under attack
 Left: Literature - Otto, F., *Das Hängende Dach*, 1954 –hypar roof with a shape parameter of 4,7
 Right: Wind tunnel measurements – hypar roof with a shape parameter of 11,3

The experimentally obtained external pressure coefficient distributions for the low corner under attack of the hypar building roof (right) are in good correlation to the one that is presented in ‘Das Hängende Dach’ (left). The experimentally defined pressure coefficients are for almost each roof zone slightly larger compared to the ones presented in ‘Das Hängende Dach’. The roof is loaded by constant suction over the central and downwind areas, with significantly larger values at the upwind low corner and edges. The radial pattern of the simplified pressure coefficient distribution could be reduced from five radial zones up to three, in analogy to the high corner under attack. (All charts — Appendix C)

With the low corner under attack (Figure 51), the experimentally obtained pressure coefficients are for almost each roof zone slightly larger compared to the ones presented in 'Das Hängende Dach'. except for the zone close to the upwind low corner where they are two, up to three times larger. The radial pressure coefficient distribution (with its centre at the upwind low corner) as presented in 'Das Hängende Dach', illustrates the experimentally obtained higher suction values at the upwind edges and the rather constant values towards the downwind zones. Mark that for this orientation, the simplified distribution has a narrower radial subdivision compared to the one that is presented for the high corner under attack. By interpreting the experimentally obtained results, it would be recommended to reduce the five radial zones up to three. By considering three zones, the pressure variation between the considered subzones would be more in analogy to the high corner under attack. On the other hand, the accuracy for the high corner under attack could be improved by increasing the radial subdivision up to five. However, one has to make a trade off between higher accuracy and reduced ease of use.

Also with the low corner under attack, prevailing suction is generated near the upwind corner and edges, as a result of the acceleration and separation of the redirected wind that flows around the upwind roof edge. However, the recorded pressure coefficients have slightly lower values than for the high corner under attack. Just behind these prevailing suction values a significant decrease in suction is observed, as a result of the reduced wind speed that flows over the positively inclined roof. Thereafter, suction remains rather constant for the central and downwind areas of the roof. The preservation of constant suction is the result of a complex interplay between the wind interaction at the roof surface and the separation of the wind at the downwind zone of the roof. The negative inclination at the downwind low corner induces this separation that initiates progressively from the central inflection point (in the middle of the roof) onwards.

For highly curved hypar roofs with a very small shape parameter, the roof could be loaded by downward acting pressure at the upwind zones and by upward acting suction at the downwind zones (cfr. ridge shaped duo-pitch roof). The downward acting pressure could develop upwind, close to the low corner under attack, as a result of the locally positive inclination of the roof. Thereafter, the downward acting pressure reduces towards the central areas of the roof, as a result of the reduced wind speed that flows over the inclined roof surface. And finally, upward acting suction could develop at the downwind areas, as a result of the generated wake above the negative inclination of roof at the downwind low corner. However, compared to a referential ridge shaped duo-pitch roof, the differential pressure over the main upwind and downwind areas is limited by the good aerodynamics of the hypar roof relative to the wind angle of attack.

4.2.6 Hypar canopy

Hypar canopy structure



Model	Hypar roof
Walls	No
Number of pressure taps	62 (32 upper + 30 lower face)
Maximal tunnel blockage	1,36%
Wind direction	0° - 180°, steps of 15°
Flow type	Free Field
Wind velocity	15 m/s
Atmospheric pressure	100110,3 ± 5,63 Pa
Relative humidity	62 ± 0,1%
Temperature	23,1 ± 0,04 °C
Air density	1,18476 kg/m ³
Number of samples	500
Sampling frequency	10 Hz
Sampling length	50 s

Table 15: Wind tunnel testing conditions – hypar canopy with a shape parameter of 11,3

4.2.6.1 360°-rotation

For the hypar canopy roof, the experimentally obtained pressure graphs of a single rotation sequence are presented in Figure 52. Also for this case the graphs are subdivided for measurements near the high and the low corner to account for the locally different orientation of each quarter of the hypar roof. For the hypar canopy structure, combined conclusions can be drawn as for the hypar building roof of section 4.2.5 and the flat and duo-pitch canopy structures of sections 4.2.2 and 4.2.4. The graphs clearly illustrate the orientation dependency of the pressure measurements for the upper and the lower face of the canopy roof. In analogy to the duo-pitch canopy, the lower face pressure measurements develop inversely compared to the upper face pressure measurements as a natural consequence of the supplemental orientation of both roof faces relative to the wind angle of attack. Depending on the considered roof zone and the wind angle of attack, a net downward acting pressure or a net upward acting suction will develop and load the considered roof zone. Mark that for a more highly curved hypar canopy the orientation dependency of the pressure measurements would become even more significant.

The absence of walls drastically reduces the amount of blocked air and allows the wind to interact directly on the upper and the lower face of the canopy roof. The rather similar pressure measurements observed for the upper and lower face are attributed to the quite equally redistribution of the blocked air over and underneath the canopy. However, the lower face tends to be vulnerable for higher turbulence and slightly smaller suction, what could be explained by the restricted opening under the canopy roof in comparison to the free field above.

Compared to the hypar building roof of section 4.2.5, the recorded pressure measurements on the upper face have changed significantly. In general, the suction at the upper face is reduced by a factor of five, and locally even slightly downward acting pressures initiate. These slight positive pressures develop for specific orientations as a result of the positive roof inclination relative to the wind angle of attack. Prevalent upper face suction at the high and low corner is observed with the low corner under attack. These suction values develop simultaneously on the downwind low quarter and on the side oriented high quarters (rotation of 90° up to 180° for the low corner; rotation of 90° up to 180° and 270° up to 360° for the high corner). However, most extreme suction is observed locally at the vertex of the high corner under attack (rotation of approximately 45°), whereby the pressure taps at the high corner are located most upwind. Furthermore, suction generally decreases towards the downwind zones as a result of the induced vortices, the roughness, and the viscosity and friction forces at the roof surface. Nevertheless, a local increase of suction is observed near the downwind low corner at a rotation of approximately 135°. This increase of suction results from the local separation of the wind flow and the generated wake above the downwind low corner. Finally, highest turbulence is observed at the upwind areas with most extreme values for respectively the high and the low corner under attack (rotation of 0° up to 90° for the low corner and 270° up to 360° for the high corner).

The established pressure measurements on the lower face of the hypar canopy roof clearly indicate their orientation dependency and their inverse development compared to the recorded upper face pressures. The lower face is mainly loaded by suction, with locally slightly positive pressures as a result of the locally negative roof inclination relative to the wind angle of attack. Prevalent suction is observed with the high corner under attack. This suction values develop simultaneously at the downwind high quarter and at the side oriented low quarters (rotation of 180° up to 270° for the high corner; rotation of 0° up to 90° and 180° up to 270° for the low corner). The recorded suction decreases towards the downwind zones as a result of the induced vortices, the roughness, and the viscosity and friction forces at the roof surface. Finally, a rather constant amount of turbulence is observed during the entire rotation process, where generally higher turbulence is recorded at the upwind zones. This phenomenon could be attributed to a complex interplay of the good aerodynamics of the hypar canopy roof and the restricted opening under the canopy itself.

In analogy to the hypar roof, the lowly curved hypar canopy tends to behave as a flat canopy, while a more highly curved variant would tend more towards of a duo-pitch canopy (ridge shaped when the low corner of the hypar is under attack and trough shaped when the high corner is under attack). However, one should always consider the complex interplay of the better aerodynamics of a hypar canopy compared to a duo-pitch canopy.

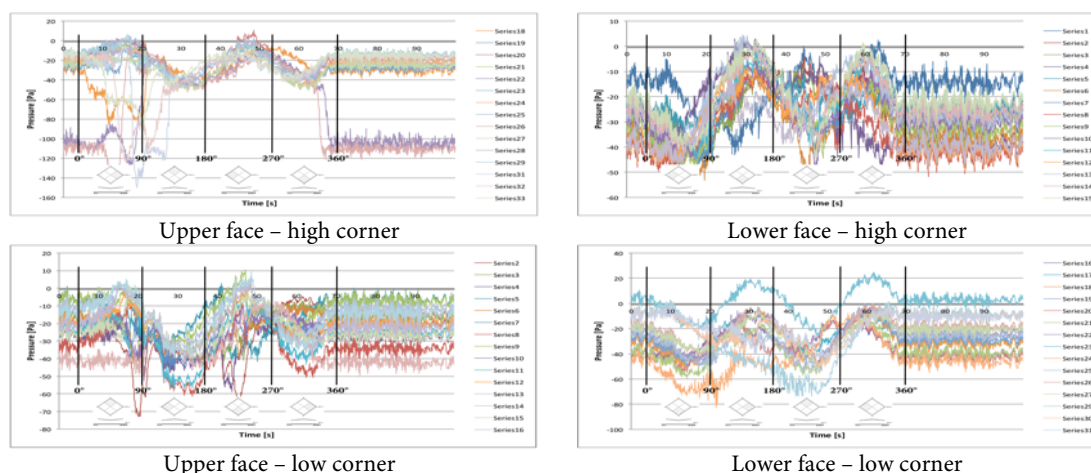


Figure 52: Wind tunnel pressure measurements – continuous rotation – hypar canopy with a shape parameter of 11,3

During the rotation process, both faces of the hypar canopy roof are mainly loaded by counteracting suction, except for some small pressure values locally. The changing pressure measurements on both faces of the roof clearly illustrate the orientation dependency of the hypar canopy. Moreover, the development of the lower face pressure measurements is inversely compared to the upper face pressure measurements, with slightly lower suction values. Compared to the hypar building roof of section 4.2.5, the recorded wind pressures on the upper face have decreased by a factor of five. Prevalent suction on the upper face is observed with the low corner under attack (rotation of 90° up to 180° for the low corner; rotation of 90° up to 180° and 270° up to 360° for the high corner — upper face). However, most extreme suction and highest turbulence is observed locally at the vertex of the high corner under attack (rotation of 45° — upper face). Prevalent suction on the lower face is observed with the high corner under attack (rotation of 180° up to 270° for the high corner; rotation of 0° up to 90° and 180° up to 270° for the low corner — lower face).

Caution, while interpreting the graphs: the pressure measurements on the lower face shift -180° compared to the pressure measurements on the upper face, the high corner shifts -90° compared to the low corner, and consider the bi-symmetry of the hypar canopy. (Larger resolution — Appendix B)

4.2.6.2 Discrete angles of attack

The net pressure coefficient distributions for the hypar canopy roof are generated for wind orientations of 0° up to 180° , with increments of 15° . By the lack of codes and literature studies for this type of structures, the hypar canopy is assessed in analogy to hypar building roof of section 4.2.5.

The sequence of experimentally obtained net pressure coefficient distributions for wind orientations ranging between 45° and 135° is presented in Figure 53. Also for this case, the range from 0° up to 45° and from 135° up to 180° is excluded from the presented sequence as a consequence of the diagonal bisymmetry of the hypar canopy roof. The orientation of the hypar canopy relative to the wind angle of attack has a rather limited influence on the net pressure distributions. In most cases the counteracting suction on the upper and lower roof face neutralise one another. This phenomenon illustrates the good aerodynamics of the hypar canopy roof, which behaves rather as a flat plate or a flat canopy roof. Nevertheless, a logical relationship between the change in orientation and the shift of the extreme pressure coefficients is still observed. The extreme pressure coefficients are recorded locally close to the upwind corner and edge areas, with most extreme net suction for the high corner under attack (rotation of 45°), and most extreme net pressure for the low corner under attack (rotation of 135°). Besides, pressure coefficient values remain more or less constant over the central and downwind areas. Notwithstanding, the orientation dependency has to be considered, especially for the more highly curved hypar roofs. The higher the curvature of the roof, the more orientation dependent the net pressure distribution will become.

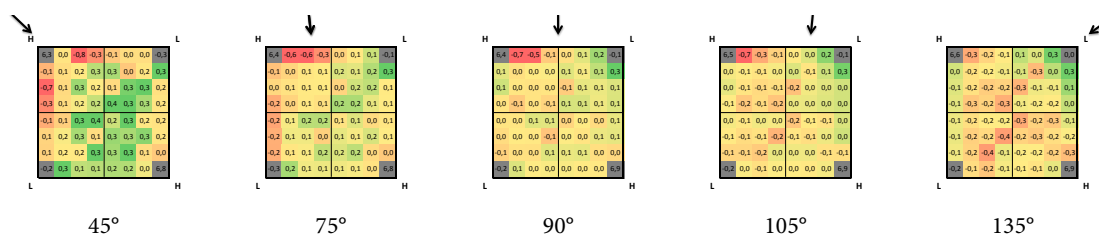
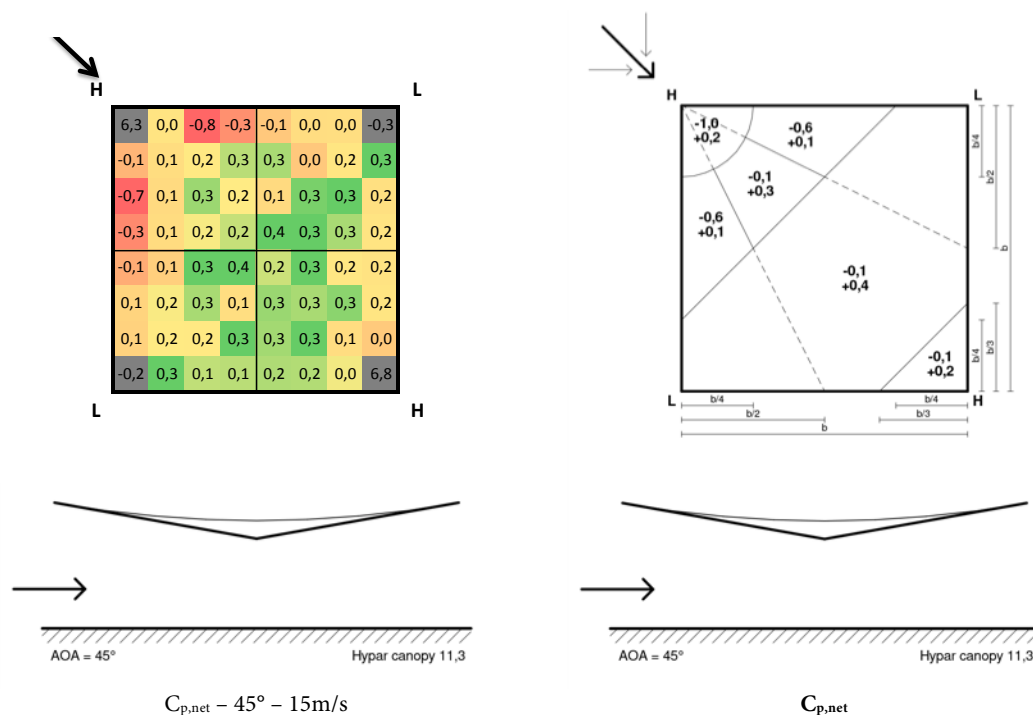


Figure 53: Wind tunnel net pressure coefficient distributions – discrete angles – hypar canopy with a shape parameter of 11,3

The orientation of the hypar building roof relative to the wind angle of attack has a rather limited influence on the net pressure distributions. In most cases the counteracting suction on the upper and lower roof face neutralise one another. The extreme pressure coefficients are recorded locally close to the upwind corner and edge areas, with most extreme net suction for the high corner under attack (rotation of 45°), and most extreme net pressure for the low corner under attack (rotation of 135°). Besides, pressure coefficient values remain more or less constant over the central and downwind areas.

For the analysis of the experimentally obtained net pressure coefficient distributions for different angles of attack, a simplified distribution has been created (Figure 54 and Figure 55). In analogy to the hypar building roof of section 4.2.5, the hypar canopy structure is assessed with the high and the low corner under attack. From the sequence of experimentally obtained net pressure coefficient distributions (Figure 53), it was observed that by accounting for these two diagonal cases within a range of 45° either side, the critical wind load distributions are considered. Furthermore, a symmetrical development of pressure towards these two orientations is recorded, with most extreme pressure values close to the upwind corner and edges. Consequently, the two simplified net pressure coefficient distributions are based on the ones that are presented in ‘Das Hängende Dach’ for the external pressure coefficients over a hypar building roof. The adopted distributions are adjusted by considering a trade off between the accuracy and the ease of use. Furthermore, the simplified distributions should at least contain a symmetrically subdivision along the diagonal bisymmetry of the hypar canopy and should account for the locally extreme wind loads 45° either side of the considered orientation, in accordance to the experimentally obtained insights. These two principles are also observed in the pressure coefficient distributions that are presented by the Eurocode for the conventional building typologies.



$C_{p,net} - 45^\circ - 15m/s$ $C_{p,net}$
 Figure 54: Analysis hypar canopy – net pressure coefficients with high corner under attack
 Left: Wind tunnel measurements – hypar canopy with a shape parameter of 11,3
 Right: Simplified net pressure coefficient distribution – hypar roof with a shape parameter of 11,3

The simplified net pressure coefficient distribution for the high corner under attack of the hypar canopy roof (right) is based on the distribution for the hypar building roof of ‘Das Hängende Dach’, with an additional subzone near the vertex of the downwind high corner. The upwind high corner is loaded by highest net suction, followed by slightly lower values close to the upwind edges. The slightly net pressure just behind the upwind high corner develops further towards the central and main downwind areas, and reduces locally near the vertex of the downwind high corner. (All charts — Appendix C)

With the high corner under attack (Figure 54), the simplified net pressure coefficient distribution is based on the distribution for the hypar building roof of ‘Das Hängende Dach’. The radial pattern with its centre at the upwind high corner is preserved, with an additional subzone near the vertex of the downwind high corner.

The upwind high corner is loaded by highest net suction, followed by slightly lower values close to the upwind edges. The development of this net suction is mainly attributed to the locally negative inclination of the canopy roof relative to the wind angle of attack. The wind that is redirected over the canopy accelerates around the upwind roof edges and separates from the upper face of the roof, causing prevailing suction to develop on the upper face. For this zone, suction values on the upper face are significantly larger compared to the lower face, causing the net suction to develop. The zone just behind the upwind high corner is loaded by slightly net pressure, as a result of the higher suction on the lower face compared to the upper face. The prevailing suction on the lower face could be attributed to the Venturi effect, while the lower suction on the upper face is induced by the generated wake near the upwind high corner. The net pressure increases further towards the central and main downwind areas, as a result of the positive inclination of the roof at the downwind corner. The suction on the upper face reduces further, with even locally some positive pressure to develop, while the suction on the lower face increases as a result of the wind that separates from the central inflection points onwards. Finally, a reduction of the net pressure is observed near the vertex of the downwind high corner. This decrease of net pressure could be mainly attributed to the downwind aerodynamics of the hypar canopy relative to wind angle of attack, causing a local increase of suction on the upper face close to the vertex of the downwind high corner.

For highly curved hypar canopies with a very small shape parameter, the net pressure distribution would be more explicitly pronounced (cfr. trough shaped duo-pitch canopies). The higher inclination of the roof will locally affect the pressure coefficients. Close to the upwind high corner the negatively inclined roof would cause higher net suction to develop, while close to the downwind high corner the positively inclined roof would cause higher net pressure to develop. At the same time, it could be expected that the pressure values at the side oriented low quarters will remain more or less constant. The side oriented quarters would behave rather as a flat plate, as a result of their orientation relative to the wind angle of attack (more or less along the wind flow). These two zones are suggested by the dotted lines in the simplified pressure coefficient distribution.

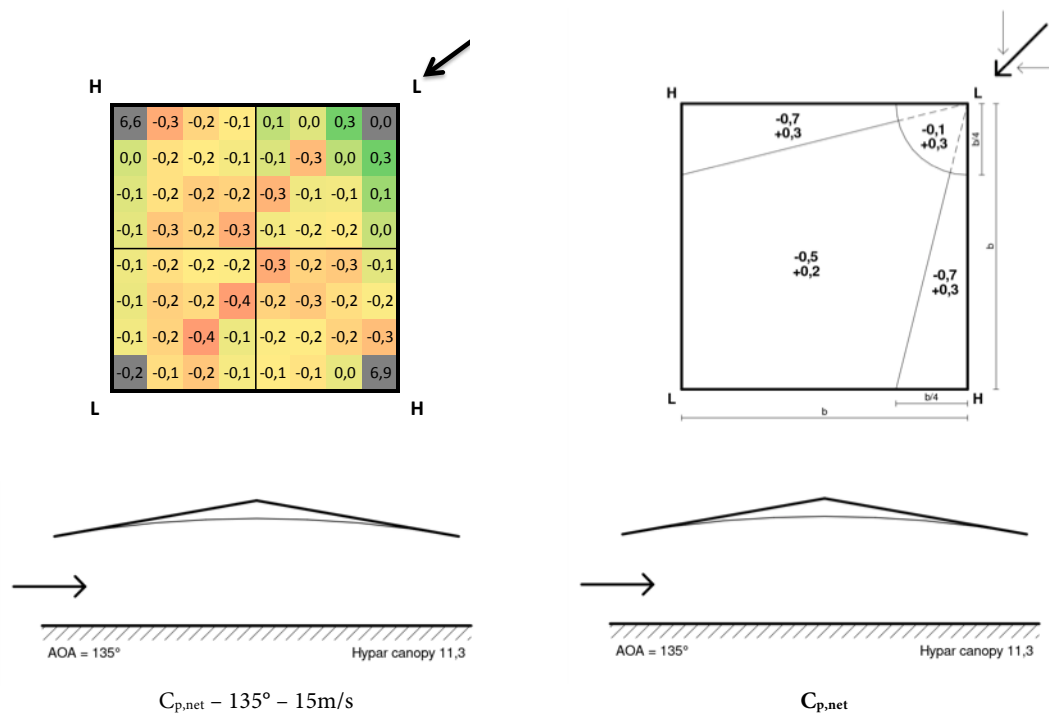


Figure 55: Analysis hypar canopy – net pressure coefficients with low corner under attack

Left: Wind tunnel measurements – hypar canopy with a shape parameter of 11,3

Right: Simplified net pressure coefficient distribution – hypar roof with a shape parameter of 11,3

The simplified net pressure coefficient distribution for the low corner under attack of the hypar canopy roof (right) is based on the distribution for the hypar building roof of 'Das Hängende Dach', with three radial zones instead of five. The upwind low corner is loaded by highest net suction, followed by slightly lower values close to the upwind edges, while the central and main downwind areas are loaded by net suction. (All charts – Appendix C)

With the low corner under attack (Figure 55), the simplified net pressure coefficient distribution is based on the distribution for the hypar building roof of 'Das Hängende Dach'. The radial pattern with its centre at the low corner has three subzones instead of five, and the proportion of the zone at the upwind low corner is reduced.

The upwind low corner is loaded by highest net pressure, as a result of the locally positive inclination of the canopy roof relative to the wind angle of attack. The wind that is redirected underneath the canopy accelerates around the upwind roof edges and separates from the lower face of the roof, causing prevailing suction to develop on the lower face. For this area, suction values on the lower face are larger compared to the upper face where even slight positive pressure could be generated. This net pressure turns rapidly into net suction further away from the upwind corner, where it tends to stay constant for the central and downwind area of the canopy roof. At this large zone, the suction is larger at the upper face compared to the lower face. The prevailing suction on the upper face could be attributed to the high wind speed flowing over the rather aerodynamic roof, while the lower suction on the lower face could be attributed to the Venturi effect. Furthermore, locally higher suction values are recorded near the upwind edges of the side oriented high quarters. Finally, also for this case, suction decreases close to the downwind edges, as a result of the downwind aerodynamics of the hypar canopy relative to wind angle of attack. However this reduction is less significant than for the high corner under attack.

For highly curved hypar canopies with a very small shape parameter, the net pressure distribution would be more explicitly pronounced (cfr. ridge shaped duo-pitch canopies). Close to the positively inclined upwind low corner higher net pressure would develop, while close to the negatively inclined downwind low corner higher net suction would develop. Also for this case, the side oriented quarters would behave rather as a flat plate, what would cause the suction values at the side oriented high quarters to remain more or less constant.

Finally, it is important to mark that each wind tunnel experiment is defined by its own situation specific parameters and has to be considered as a specific test case. Parameters such as detailing of the edges, location of the pressure taps, surface finishing, off axis rotation, type of wind tunnel, et cetera, have significant influence on the experimental results. A minor change of one of these parameters could cause significant changes in the pressure measurements, which cannot be neglected and should be considered while interpreting the results.

5

Conclusion

During the last decades, the use of tensile surface structures has increased significantly. Compared to the more conventional medium to heavy weight building structures, these lightweight membrane structures are more sensitive to external loading, as a result of their high load-to-self-weight-ratio. Among them, the increased vulnerability to external wind loading has been stipulated by the collapse of several tensile surface structures around the world (due to failure of the membranes, failure of the supporting system, failure of the connections between membranes and supporting structure, failure of the foundations...). Consequently, to ensure the safety for these structures without going into uneconomic over dimensioning, the need for extensive wind analysis has been stressed. In general, conventional codes on wind design give upper bound values for the majority of structures, but the level of uncertainties increases as the building configuration deviates from the codified norms. From this point of view a lot of research on the wind loading of membrane structures is still required, ranging from overall pressure coefficient distributions for typical membrane geometries, to local effects, dynamic or aero-elastic responses, and so on. Hereby, a general reference wind tunnel testing field (specifying some standard geometries, dimensional proportions and testing conditions) could form a significant step forward in the generalization of wind loading on this type of structures, especially in the scope of the current Eurocode.

Within this scope, this master thesis forms a first step in the experimental wind tunnel analysis on tensile membrane structures, and more specific for the wind loading on hyperbolic paraboloid roof and canopy structures.

5.1 Fabrication process of the wind tunnel models

Before wind tunnel testing could initiate, adequate wind tunnel models had to be fabricated. By the absence of reference literature and the need of very thin roof structures allowing pressure measurements to take place simultaneously at the upper and lower face of the roof, extensive research has been performed for adequate production techniques and materials. The technical feasibility study, based on the model requirements and directories (dimensions, cost, curvature, accuracy...), resulted in the fabrication of glass-fibre reinforced composite models in a CNC-milled female mould. This innovating production process allows the fabrication of very thin-shelled rigid roof structures with a large freedom of curved shapes, while preserving sufficient resistance to the wind loads during wind tunnel testing.

For this thesis, three different roof structures have been fabricated: a flat roof, a duo-pitch roof with pitch inclinations of 30° and a hypar roof with a shape parameter of 11,3). The models are equipped with removable walls to allow investigating the wind loads on each model as a building roof and as an open canopy structure.

5.2 Wind tunnel experiments

In a first stage, wind tunnel experiments are performed on the flat and the duo-pitch roof structure to validate the wind tunnel experiments and to create a reference-testing field for the second stage of tests on the hypar roof structure. The conformity between the experimentally obtained pressure coefficient distributions for the flat and the duo-pitch roof and the ones illustrated in Eurocode 1 (EC1 – part 1.4) approves the accuracy of the fabricated wind tunnel models and the wind tunnel testing set-up. The general pressure coefficient distributions correspond well, except for some local deviations which could be attributed to minor anomalies in the models (amount and location of the pressure taps, detailing of the edge, thickness of the roof, smoothness of the surfaces, imperfections...) and the testing conditions (slightly off axis orientations, model elevation height, local turbulences, experimental flaws...). Consequently, while interpreting the experimentally recorded wind tunnel data it is important to consider the situation specific parameters for each wind tunnel experiment, because a minor chance of one of these parameters could cause significant changes in the pressure measurements.

The recorded wind tunnel data indicates a significant variation in pressure values for the open and enclosed building situations. In case of rather aerodynamic roof shapes, the net and external wind loads tend to be lower for open canopies compared to the enclosed buildings. A significant reduction in suction, even up to positive pressure,

is recorded at the upper face of the canopy roof, as a result of the reduced amount of blocked air that is redirected over the roof. For less aerodynamic roof shapes, the wind-structure interaction is more complex. For these cases, higher wind loads could develop, depending on the accumulation and separation zones over the structure.

For hypar building roofs and canopies with high and low corners, two orientations have to be considered: respectively with a high and a low corner under attack. Highest suction is observed locally near the high corner under attack, while highest pressure is observed locally near the low corner under attack. Generally, for these two skew orientations, rather similar conclusions could be drawn as for the perpendicularly oriented ridge and trough shaped duo-pitch roofs, although by considering the improved aerodynamics of the hypar roof relative to the wind angle of attack. Furthermore, the pressure coefficient distribution geometry is expected to be independent from the shape parameter of hypar roofs and canopies (in analogy to the pitch angle independency for duo-pitch roofs and canopies). The geometrical similarity of the pressure coefficient distributions is a natural consequence of the identical building typology. For highly curved hypars with a very small shape parameter, the pressure distribution is expected to be pronounced more explicitly (with more extreme pressure values and more differential pressure over the upwind and downwind zones), while the pressure values at the side oriented low quarters will remain more or less constant. However, to confirm these hypotheses, additional research is required on hypar roof structures with different shape ratios. For the investigated hypar roof structure with a shape parameter of 11,3, simplified pressure coefficient distributions are presented. These distributions could be used in the wind load calculations as presented by the Eurocode for the conventional building typologies. The accuracy of the simplified pressure coefficient distributions could be improved by increasing the radial subdivision, but this will cause the usability to reduce. Consequently, a trade off between the accuracy and the usability of the simplified pressure coefficient distributions has to be made.

5.3 Future scope

Since this master thesis performs a first step in the field of wind analysis on tensile membrane structures, lots of research is still required. The performed investigation of the wind loads on the hypar roof structure forms a first attempt towards an additional Eurocode section on the wind design of tensile surface structures. Wind tunnel testing on more hypar roof structures, with different shape parameters, is required to verify the currently proposed pressure coefficient distributions. Besides, pressure coefficient tables containing overall and local coefficients for different shape parameters have to be examined (in analogy to those presented in the Eurocode for different roof inclinations of conventional building typologies). Furthermore, this investigation has to be extrapolated for a series of 'typical' membrane shapes (not only for hyperbolic paraboloids, but also for cones, arch forms and wave types) to form a fundamental basis for a more general Eurocode on designing membrane structures.

Considering the significance of the upwind edges on the pressure coefficient distributions, additional wind analysis close to the membrane edges and corners should be performed. In general, the better the aerodynamics of the edge, the lower the degree of blockage and thus the lower the separation of wind. From this point of view it is important to consider the typical membrane edge conditions (free membrane edge, cable or belt reinforced edge, strut or bar reinforced edge...) and their structural thicknesses.

Furthermore, extensive investigation on dynamic wind interactions of the flexible membrane structures is required. In many cases, membrane structures will deform significantly under wind loading, causing modifications in the flow regime that lead to different interactions between the fluid and the structure. It is difficult to predict these dynamic interactions and to estimate their impact. Wind tunnel testing on properly scaled aero-elastic models of basic membrane structures could provide insights in the deformation behaviour of flexible membrane structures. In addition, real scale experiments in outdoor situations should be used to verify the wind tunnel experiments and to counter the limitations of scaled wind tunnel tests. Furthermore, wind tunnel testing and real scale experiments should be used to optimise numerical simulations and Computational Fluid Dynamics for tensile membrane structures. The use of these techniques is growing and already an approved alternative to wind tunnel experiments for conventional building structures and much civil engineering works, but in the field of membrane structures encoding the numerical coupling of fluid-structure interaction is vital for these techniques.

6

Bibliography

- [1] Alcaniglia. (2010). *Rock me like a Hurricane part II*. Retrieved June 3, 2014 from http://alcaniglia.blogspot.be/2010_10_01_archive.html
- [2] Autodesk. (2014). <http://www.autodesk.nl/products/autodesk-inventor-family/>. Retrieved May 13, 2014
- [3] Baglin, P. (2002). *ARIES canopy wind tunnel test results*. tensARC Ltd., Munich.
- [4] Balz, M., & Fildhuth, T., Schlaich Bergermann and Partners. (2004). Wind Loading on Stadia Roof Structures. In M. Mollaert, J. Haase, J. Chilton, E. Moncieff, M. Dencher, & M. Barnes (Ed.), *TensiNet Symposium 2003 – Designing Tensile Architecture* (pp. 140-149). Brussels: VUB.
- [5] BBC News Northern Ireland. (2011). *Northern Ireland still being hit by Hurricane Katia*. Retrieved June 3, 2014 from <http://www.bbc.co.uk/news/uk-northern-ireland-14879075>
- [6] Belgian Building Research Institute. (2013). http://www.bbri.be/antenne_norm/eurocodes/. Retrieved March 8, 2014
- [7] Belgisch instituut voor normalisatie. (2002). *Eurocode 0: Basis of Structural Design*. NBN EN 1990: 2002. Brussels: BIN.
- [8] Belgisch instituut voor normalisatie. (2005). *Eurocode 1: Actions on structures - Part 1-4: General Actions - Wind actions*. NBN EN 1991-1-4: 2005. Brussels: BIN.
- [9] Burton, J., & Gosling, P. (2003). Wind Tunnel Pressure Measurements on Conic Shaped Membrane Roof Arrangements. *International conference on textile composites and inflatable structures - structural membranes* (pp. 427-432). Barcelona: CIMNE.
- [10] BZT. (2014). <http://www.bzt-cnc.de/>. Retrieved May 13, 2014
- [11] Carradine, D. M. (1998). *Experiments on the Response of Arch-Supported Membrane Shelters to Snow and Wind Loading*. Master Thesis, Virginia Polytechnic Institute and State University, Blacksburg.
- [12] Cook, M. J. (1981). *Wind Tunnel Tests for a Large Surface Stressed Structure in Kuwait*. Buro Happold Engineers Ltd.
- [13] Counihan, J. (1975). Adiabatic Atmospheric Boundary Layers: A Review and Analysis of Data from the Period 1880-1972. *Atmospheric Environment*, 9, 871-905.
- [14] Deskproto. (2014). <http://www.deskproto.com/>. Retrieved May 13, 2014
- [15] Dirnberger, J. M., Kennesaw State University. (2008). *Biological Oceanography Lecture: Basic Physical Processes of the Water Column*. Retrieved May 2, 2014 from <http://science.kennesaw.edu/~jdirnber/BioOceanography/Lectures/LecPhysicalOcean/LecPhysicalOcean.html>
- [16] Dyrbye, C., & Hansen, S. O. (1997). *Wind Loads on Structures*. Chichester: Wiley.
- [17] Elnokaly, A., Chilton, J., & Wilson, R. (2004). CFD investigation of airflow around conic tensile membrane structures [printed extended abstract; conference paper on CD-ROM]. *International Symposium on Shell and Spatial Structures from Model to Realization* (pp. 138-139). Montpellier: IASS.
- [18] Fabritec Structures. (2014). <http://www.fabritecstructures.com/>. Retrieved June 3, 2014
- [19] Fabritecture. (2014). <http://www.fabritecture.com/>. Retrieved June 3, 2014
- [20] Forster, B., & Mollaert, M. (2004). *European Design Guide for Tensile Surface Structures*. TensiNet. Brussels: VUB.
- [21] Frech, J., The StarPhoenix. (2014). *Extreme wind in Saskatchewan*. Retrieved June 3, 2104 from http://live.thestarphoenix.com/Event/Extreme_wind_in_Saskatchewan
- [22] Geurts, C., & van Bentum, C. (2007). Wind Loading on Buildings: Eurocode and Experimental Approach. In T. Stathopoulos, & C. C. Baniotopoulos (Eds.), *International Centre for Mechanical Sciences - Wind Effects on Buildings and Design of Wind-Sensitive Structures* (Vol. 493, pp. 31-65). Montreal: CISM.

- [23] Gill, T., Fayetteville Flyer. (2012). *Strong winds cause damage at Arkansas Music Pavilion*. Retrieved June 3, 2014 from <http://www.fayettevilleflyer.com/2012/07/08/strong-winds-damage-at-arkansas-music-pavilion/>
- [24] Gorlin, W. B. (2009). Wind Loads for Temporary Structures: Making the Case for Industrywide Standards. *Journal of Architectural Engineering*, 15 (2), 35-36.
- [25] Gorlin, W. B. (2009). Temporary Structures Need Wind-Load Standards. *Structure Magazine*, January, pp. 23-25.
- [26] Gosling, P., & Zhang, L. (2010). A non-safety factor approach to the design of membrane structures. In M. Mollaert, & H. Bögner-Balz (Ed.), *TensiNet Symposium 2010 - Textile Architecture: Connecting Past and Future* (pp. 13-22). Sofia: Sofin.
- [27] Hart, R., Birchall, M., Fisher, A., & Williams, C. (2010). SMART Particles: Dynamic Wind-Structure Interaction Analysis for Tensile Structures. In H. Bögner-Balz, & M. Mollaert (Ed.), *TensiNet Symposium 2010 - Tensile Architecture: Connecting Past and Future* (pp. 69-77). Sofia: Sofin.
- [28] Hasler, J. P., Popular Mechanics. (2010). *What went wrong: How the Dallas Cowboy's Field House Collapsed*. Retrieved June 3, 2014 from <http://www.popularmechanics.com/outdoors/sports/football/how-the-dallas-cowboys-field-house-collapsed>
- [29] Hasler, J. P., Popular Mechanics. (2011). *Why Are So Many Outdoor Concert Stages Collapsing?* Retrieved June 3, 2014 from <http://www.popularmechanics.com/technology/engineering/why-are-so-many-outdoor-concert-stages-collapsing>
- [30] Heslop, A. (2002). Developing a fuller understanding of wind Loads on Membrane Structures. In M. Mollaert, S. Hebbelinck, & J. Haase (Ed.), *VUB Symposium 2000 - The Design of membrane and lightweight structures* (pp. 227-235). Brussels: VUB.
- [31] Heslop, A., Architen Landrell. (2004). Conical structure wind tunnel test data, Landrell Architecten. In B. Forster, & M. Mollaert (Eds.), *European Design Guide for Tensile Surface Structures*. Brussels: VUB.
- [32] Heslop, A., Architen Landrell. (2010). *Basic Theories of Tensile Membrane Architecture*. Retrieved May 13, 2014 from <http://www.architen.com/articles/basic-theories-of-tensile-membrane-architecture/>.
- [33] Iyengar, A. K., & Farell, C. (2001). Experimental issues in atmospheric boundary layer simulations: roughness length and integral scale determination. *Journal of Wind Engineering and Industrial Aerodynamics*, 89, 1059-1080.
- [34] Jacoby, M. (1988). *Pressure coefficients for basic tensioned-membrane structure forms*. Naval Civil Engineering Laboratory. Port Heuneme: NTIS GRA&I.
- [35] Joint Research Centre. (2014). <http://eurocodes.jrc.ec.europa.eu/>. Retrieved March 8, 2014
- [36] Kiel, N., Webjournaal. (2012). *Tent komt effe aanwaaien....* Retrieved June 3, 2014 from <http://nankokiel.wordpress.com/2012/08/31/tent-komt-effe-aanwaaien/>
- [37] Locke. (1828). *The First Book of Ovid's Metamorphoses with a Literal Interlinear Translation, and Illustrative Notes*. London: Littlewood & Co., Old Bailey.
- [38] Lutgens, F. K., & Tarbuck, J. E. (2001). *The Atmosphere* (8th edition). Upper Saddle River: Prentice Hall.
- [39] Ma, J., Zhou, D., Li, H., Zhu, Z., & Dong, S. (2006). Numerical simulation and visualization of wind field and wind load on space structure. *International Symposium on New Olympic, New Shell and Spatial Structures* (pp. 344-345). Beijing: IASS.
- [40] McKinley, J. C. JR., The New York Times. (2012). *Stage Collapses Before Toronto Radiohead Concert*. Retrieved June 3, 2014 from http://artsbeat.blogs.nytimes.com/2012/06/16/stage-collapses-before-toronto-radiohead-concert/?_php=true&_type=blogs&_php=true&_type=blogs&_r=1
- [41] Maes, M., Nieuwsblad. (2013). *Loodzware tenten Boatshow maken geen kans tegen storm*. Retrieved June 3, 2014 from http://www.nieuwsblad.be/article/detail.aspx?articleid=DMF20131028_00813635
- [42] Malinowsky, M., Club de la Structure Textile. (2004). Conical structure wind tunnel test data. In B. Forster, & M. Mollaert (Eds.), *European Design Guide for Tensile Surface Structures*. Brussels: VUB.
- [43] Michalski, A., Kermel, P. D., Haug, E., Löhner, R., Wüchner, R., & Bletzinger, K.-U. (2011). Validation of the computational fluid-structure interaction simulation at real-scale tests of a flexible 29 m umbrella in natural wind flow. *Journal of Wind Engineering and Industrial Aerodynamics*, 99, 400-413.
- [44] Monjó-Carrió, J. (2007). Common Tensile Roof Pathology and Basic Preventive Actions. In A. Zanelli, H. Bögner-Balz, & L. Rutter (Eds.), *TensiNet Symposium 2007 - Ephemeral Architecture Time and Textiles* (pp. 249-260). Milano: Libreria CLUP.

- [45] Nagai, Y., Okada, A., Miyasato, N., & Saitoh, M. (2011). Wind Tunnel Tests on the Horn-Shaped Membrane Roof. In J. C. Lerner (Ed.), *Wind Tunnels and Experimental Fluid Dynamics Research* (pp. 325-348). Shanghai: InTech.
- [46] Nagai, Y., Okada, A., Miyasato, N., & Saitoh, M. (2012). Wind Response of Horn-Shaped Membrane Roof and Proposal of Gust Factor for Membrane Structures. *Journal of the International Association for Shell and Spatial Structures*, 53 (3), 169-176.
- [47] Otto, F. (1954). *Das hängende Dach*. Dissertation, Technische Universität Berlin, Berlin.
- [48] Otto, F. (1969). *Tensile Structures: Cables, Nets and Membranes* (Vol. 2). Cambridge: MIT Press.
- [49] Plastics Warringah. (2013). *Vacuum Forming*. Retrieved April 10, 2014 from <http://warringah-plastics.com.au/root-wplastics/wp-content/uploads/2011/02/vacuum-forming-process-diagram1.jpg>
- [50] Rank, E., Halfmann, A., Scholz, D., Glück, M., Breuer, M., Durst, F., et al. (2005). Wind loads on lightweight structures: Numerical simulation and wind tunnel tests. *GAMM-Mitteilungen*, 28 (1), 73-89.
- [51] Redactie Editie - Timothy. (2009). *Storm velt tenten DRC*. Retrieved June 3, 2014 from <http://www.editedendermonde.be/2009/05/26/storm-velt-tenten-drc/>
- [52] Rhinoceros. (2014). <http://www.rhino3d.com/>. Retrieved May 13, 2014
- [53] Rizzo, F., D'Asdia, P., Lazzari, M., & Procino, L. (2011). Wind action evaluation on tension roofs of hyperbolic paraboloid shape. *Engineering Structures*, 33, 445-461.
- [54] Rizzo, F., D'Asdia, P., Ricardelli, F., & Bartoli, G. (2012). Characterisation of pressure coefficients on hyperbolic paraboloid roofs. *Journal of Wind Engineering and Industrial Aerodynamics*, 102, 61-71.
- [55] Rock News Desk. (2011). *5 dead in new stage collapse*. Retrieved June 3, 2014 from <http://rocknewsdesk.com/world-news/5-dead-in-new-stage-collapse/3138/>
- [56] Scanivalve. (2014). <http://www.scanivalve.com/>. Retrieved May 17, 2014
- [57] Schamper, Universiteit Gent. (2011). *Pukkelpop 2011: Tent aan Boiler Room*. Retrieved June 3, 2014 from <http://www.schamper.ugent.be/afbeelding/pukkelpop-2011-tent-aan-boiler-room>
- [58] Silas, J., The Wall Street Journal. (2011). *Scenes From the Stage Colapse*. Retrieved June 3, 2014 from <http://online.wsj.com/news/articles/SB10001424053111903392904576508813891203284#3>
- [59] SMILE Winter activity Satellite Winds. (2007). *The Beaufort Scale of Wind Velocity*. Retrieved May 2, 2014 from <http://www.docstoc.com/docs/82804867/The-Beaufort-Scale>
- [60] Stathopoulos, T. (2007). Introduction to Wind Engineering, Wind Structure, Wind-Building Interaction. In T. Stathopoulos, & C. C. Baniotopoulos (Eds.), *International Centre for Mechanical Sciences - Wind Effects on Buildings and Design of Wind-Sensitive Structures* (Vol. 493, pp. 1-30). Montreal.
- [61] Stratasys. (2014). <http://www.stratasys.com/>. Retrieved April 10, 2014
- [62] Sun, X. Y., Chen, Z. Q., Wu, Y., & Shen, S. Z. (2012). Numerical studies on the behaviors of wind-structure interaction for membrane structures. *7th International Colloquium on Bluff Body Aerodynamics and Applications* (pp. 234-243). Shanghai: BBAA.
- [63] Sunrise Packing. (2013). *Upcoming Trends in Thermoforming*. Retrieved April 10, 2014 from <http://www.sunrisethermoforming.com/upcoming-trends-in-thermoforming/>
- [64] Technische Universität München, Institute of Aerodynamics and Fluid Mechanics. (2014). *Aerodynamics of Buildings*. Retrieved April 10, 2014 from <http://www.aer.mw.tum.de/en/research-groups/aerodynamics-of-buildings/>
- [65] TensiNet. (2012). *Wind Loading WG5 - Draft Version*. TensiNet.
- [66] TensiNet. (2014). <http://www.tensinet.com/>. Retrieved February 21, 2014

Appendices

Appendix A

Wind Actions – Eurocode Mathematical model for wind design

Appendix A

A.1 Eurocode NBN EN 1991-1-4:2005	66
A.2 Mathematical model for the turbulent wind.....	67
A.3 Wind interaction.....	71
A.4 Pressure coefficients	72

List of Figures

Figure A1: Fiche Eurocode EN1991-1-4 – Summary: General actions – Wind actions – [8].....	66
Figure A2: Turbulent and mean wind velocity in function of the height – [16].....	67
Figure A3: Turbulent wind velocity in function of the time – [60]	67
Figure A4: Basic wind speed Belgium – [8].....	68
Figure A5: Atmospheric boundary layer - terrain roughness – [60]	69
Figure A6: Roughness length z_0 – [16]	69
Figure A7: Orography factor calculation – [8].....	69
Figure A8: Interpolation overall and local pressure coefficients – [8].....	72

List of Tables

Table A1: Calculation values for C_{dir} , C_{season} and C_{prob} – [8].....	68
Table A2: Terrain categories – [8]	69

A.1 Eurocode NBN EN 1991-1-4:2005

Eurocode 1: Actions on structures - Part 1-4: General actions - Wind actions provides a general directive on predicting the characteristic natural wind actions that interact on a land-based structures with a height up to 200 m. The guidance is based on a step-by-step modeling of the wind loads that will act on the components, surfaces and sub-surfaces of the considered structure. Through the calculation process the National Annex is often referred to, giving country specific values to model the wind actions that are function of the geographical and meteorological aspects of the location, such as wind climate, the terrain roughness and orography.

FICHE EUROCODE

EN 1991-1-4

Eurocode 1 : Belastingen op constructies

Deel 1-4 : Algemene belastingen – Windbelasting

FR : Eurocode 1 : Actions sur les structures - Partie 1-4 : Actions générales – Actions du vent
NL : Eurocode 1 : Belastingen op constructies - Deel 1-4 : Algemene belastingen – Windbelasting

Leiding en algemeen kader

De Eurocode 1 bepaalt hoe de krachten moeten worden berekend bij de berekening van een constructie onderhevig aan verschillende soorten belastingen en voor bepaalde bijzondere constructies (bruggen, silos, ...).

Deel 1 (EN 1991-1) is op zijn beurt onderverdeeld in een aantal deelrubrieken, waarin de krachten worden bepaald die het gevolg zijn van verschillende lasten (wind, sneeuw, thermische belastingen, ...).

Onderdeel 1991-1-4 bepaalt de belastingen te wijten aan wind en de methode om ze te berekenen.

Samenvatting van de inhoud

Deze Eurocode bestaat uit 6 secties en 6 bijlagen.

Na het afmaken van het toepassingsdomain (Sectie 1 Algemeen), worden de verschillende ontwerpituaties samengevat in Sectie 2. De Sectie 3 geeft op één blad de modellering van de windbelasting weer. Er wordt onder andere uitgelegd dat de berekende belastingen karakteristieke waarden zijn voor een terugkeerperiode van 50 jaar.

De berekening van de windbelasting begint vanaf Sectie 4 die gaat over de windsnelheid en stuwdruk. Die laatste is de windbelasting voor een gegeven hoogte en gebied. Die moet dus in balans gehouden worden door de lokale effecten die eigen zijn aan de morfologie van het gebouw.

De berekeningswijze voor de windbelastingen voor de verschillende situaties, voor de dynamische puntbelasting en voor de druk- en krachtcoëfficiënten worden uitvoerig beschreven in Sectie 5.

Sectie 6 geeft vervolgens de rekenregels om de bouwwerkfactor c_{fd} te bepalen, die rekening houden met het effect op de windbelasting van enerzijds de afwezigheid van gelijkrichtigheid van de puntbelastingen aan het oppervlak van het gebouw (c_{fd}) en, anderzijds, bijlagen van de structuur veroorzaakt door de turbulentie (c_{fd}). Deze sectie verwijst naar bijlagen B en C voor twee gedetailleerde methoden en naar bijlage D voor een reeks van klassieke waarden van deze coëfficiënt.

De druk- en krachtcoëfficiënten worden bepaald in de Sectie 7. Deze coëfficiënten bestaan uit vier types: de drukcoëfficiënten aan binnen- en buitenkant die van toepassing zijn op gesloten gebouwen, de netto drukcoëfficiënten voor dak- en geïsoleerde muren, de wrijvingscoëfficiënt voor het bepalen van de belasting evenwijdig aan de blootgestelde oppervlakten en de drukcoëfficiënt die van toepassing is voor kleinere elementen (borden, omheining, vlaggen enz.)

Tenslotte laat Sectie 8 toe de windbelasting op bruggen te bepalen.

Bijlage A (informatief) geeft alle terreinfactoren op de windbelasting weer.

Bijlage B (informatief) geeft een eerste procedure weer ter bepaling van de structurele coëfficiënt c_{fd} .

Bijlage C (informatief) geeft een tweede procedure weer ter bepaling van de structurele coëfficiënt c_{fd} .

Bijlage D (informatief) geeft c_{fd} waarden weer voor allerlei gebouwtypes.

Bijlage E (informatief) laat toe de invloed te bepalen van de wervelroming en aero-elastische instabiliteiten.

Bijlage F (informatief) laat toe de dynamische eigenschappen van de constructies te bepalen: eigen frequentie, modale vervorming, ...

ANB :
 Bijlagen A, B, E en F worden normaal voor België. Bijlage D blijft informatief en bijlage C is niet van toepassing in België.

Indicatief NBN	Taal	Prijs	Aantal blz.
Voor EN : NBN EN 1991-1-4:2005	en, fr	125 €	151
Voor ANB : NBN EN 1991-1-4-ANB:2010	fr, nl	55 €	59

Berekening van de windbelasting

De windkracht op een gebouw (F_w) wordt over het algemeen berekend aan de hand van de vergelijking:

$$F_w = c_{pe} c_{pe} S_{ref} q_p(z)$$

c_{pe} is een **drukcoëfficiënt** die afhangt van het type van het onderzochte bouwwerk. Voor een alleenstaand bouwwerk, gaat het om een c_{pe} voor een gesloten gebouw (c_{pe}), voor kleine structuren : de krachtcoëfficiënt c_{pe} , enz. Deze coëfficiënten staan in de tabellen van Sectie 7 van de Eurocode.

De **extreme stuwdruk** $q_p(z)$ hangt af van een groot aantal parameters: de referentiehoogte (z), de ruwheidscategorie van het terrein, de in acht genomen terugkeerperiode, de orografie van het terrein, de in acht genomen windrichting, enz.

De **referentieoppervlakte** (A_{ref}) is de oppervlakte die overeenkomt met een bepaalde c_{pe} . Deze oppervlakte mag niet verward worden met de **belaste oppervlakte** (A) die gebruikt wordt om c_{pe} te bepalen op basis van c_{pe} en c_{pe} . Deze laatste is de aan de wind blootgestelde oppervlakte die leidt tot de belasting van het te dimensioneren element. Bijvoorbeeld A voor een dakpan is de tussenstand van de steunen vermenigvuldigd met de afstand tussen de dakpannen.

De **bouwwerkfactor** c_{fd} mag in de volgende situaties gelijk gesteld worden aan 1:

- gebouwen waarvan de hoogte minder is dan 15 m;
- gevel- en dak-elementen waarvan de eigen frequentie hoger is dan 5 Hz;
- skeletbouw met schiedrigvanden waarvan de hoogte minder is dan 100m en dan 4 maal de opgemeten lengte in de windrichting;
- Schouwen met transversale ronde secties waarvan de hoogte kleiner is dan 60 m en dan 6,5 keer de diameter.

In andere gevallen moet de structurele coëfficiënt bepaald worden volgens §6.3 of bijlage D van de Eurocode.

Bepaling van de categorie van het terrein

Eurocode voorziet 5 ruwheidscategorieën voor terreinen geklassificeerd van de strengste naar de minst strenge:

- Zee of kustzone blootgesteld aan de zee/wind
- Meren of platte, horizontale zone met verwaarloosbare vegetatie en vrij van alle obstakels
- Zone met lage vegetatie zoals gras, met of zonder enkele, geïsoleerde obstakels (bomen, gebouwen) die minstens 20 keer hun hoogte van elkaar gescheiden zijn
- Zone met een gelijkmatige begroeiing of met gebouwen, of met geïsoleerde obstakels die maximaal 20 keer hun hoogte van elkaar gescheiden zijn (bijvoorbeeld dorpen, bebouwde kom, bebost gebied)
- Zone waarvan minimaal 15 % van de oppervlakte bedekt is met gebouwen waarvan de gemiddelde hoogte hoger is dan 15 m.

De te gebruiken terreincategorie is de minst gunstige categorie die meer dan 10% uitloopt van een hoeksector van 30° (blauw gestreept) binnen de hoeksector van 45° rond de loodrechte lijn van de te beschouwen gevel of rond de bissectie van de beschouwen hoek (zie fig.1).

De te beschouwen afstand x hangt af van de hoogte van het gebouw.

Hoogte (m)	≤ 5	10	15	25	50	75	100	200
x (m)	300	360	590	1100	2500	4100	5800	13000

Extreme stuwdruk

De extreme stuwdruk kan met de volgende vergelijking berekend worden:

$$q_p(z) = 0.625 (1 + 7I(z)) q_{ref}(z)$$

waar:

$$q_{ref}(z) = 0.19 v_{b,0} (c_{pe}/0.05)^{0.42} \ln(z/z_0) c_{pe} c_{dir} c_{top}$$

$$I(z) = \frac{1 - 2.10^{-10} (\ln(z/z_0) + 3)^8}{\ln(z/z_0)}$$

Nota: als z kleiner is dan z_{min} dan moet men in de berekening z_{min} gebruiken.

Terugkeerperiode (jaar)	1	2	5	10	20	50	100	200
c_{top}	0.75	0.78	0.85	0.90	0.85	1.00	1.04	1.08

Alkomstige windrichting	0°	22.5°	37.75°	45°	56.25°	90°	120°	150°	180°	270°
Noord	1.00	1.00	0.95	0.90	0.85	0.95	0.90	0.95	1.00	1.00
Oost										
Zuid										
West										

Tijdelijk project van minder dan 1 jaar: neem de minst gunstige maand over de ganse duur van het project.

Maand	Jan.	Feb.	Maart	April	Mai	Juni	Juli	Aug.	Sep.	Ok.	Nov.	Dec.
c_{dir}	0.92	0.92	0.85	0.77	0.69	0.69	0.69	0.69	0.77	0.85	1.00	0.92

Voor alle project die langer dan een jaar duren, is c_{dir} gelijk aan 1.

De **orografiefactor** c_{or} wordt 1 indien de gemiddelde helling van het terrein kleiner is dan 5%. In andere gevallen moet de factor bepaald worden volgens bijlage A.3 van de Eurocode.

Figure 1 - De in acht te nemen hoeksector

NBN Verkoop Dienst ☎ 02/738.01.12 ✉ verkoop@nbn.be 🌐 www.nbn.be
 WTCB Gauthier Zarmati ☎ 02/655.77.11 ✉ gauthier.eurocodes@wbti.be 🌐 www.normes.be

NBN Verkoop Dienst ☎ 02/738.01.12 ✉ verkoop@nbn.be 🌐 www.nbn.be
 Gauthier Zarmati ☎ 02/655.77.11 ✉ gauthier.eurocodes@wbti.be 🌐 www.normes.be

APRIL 2012

Figure A1: Fiche Eurocode EN1991-1-4 – Summary: General actions – Wind actions – [8]

A.2 Mathematical model for the turbulent wind

The establishment of a mathematical model that accounts for the turbulent nature of the fluctuating wind, that could be used determine and predict the wind actions on and deformations of structures, starts from defining the mean wind velocity and the peak velocity pressure. These two parameters mainly describe the fluctuating nature of wind in a characteristic distribution. Consequently both parameters are function of a mean component or the expectance value and a fluctuating component or standard deviation and accompanying probability density, to cover the extreme effects of turbulent wind with an annual exceedance of 2%. The expectance value is represented by the mean wind velocity v_m , while the fluctuating component is represented by the turbulence intensity I_v .

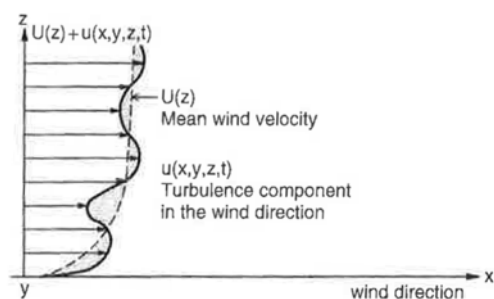


Figure A2: Turbulent and mean wind velocity in function of the height – [16]

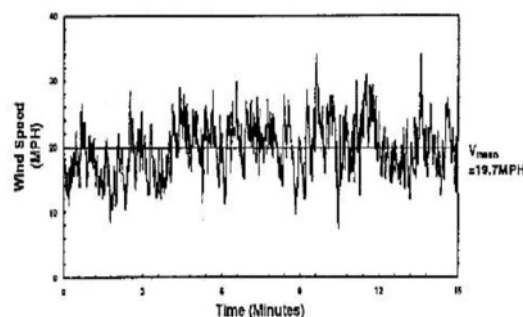


Figure A3: Turbulent wind velocity in function of the time – [60]

The **mean wind velocity** $v_m(z)$ at a height z above the terrain is function of the terrain roughness, the orography and the basic wind velocity. This function takes account for the influence of the specific conditions of the site and its surroundings on the mean wind velocity. The mean wind velocity profile shows a reduced wind speed in the so-called boundary layer close to the earth surface, caused by the viscosity and inertia forces.

$$v_m(z) = c_r(z) \cdot c_0(z) \cdot v_b$$

with:

- $v_m(z)$ the mean wind velocity
- v_b the basic wind velocity
- $c_r(z)$ the roughness factor
- $c_0(z)$ the orography factor

The **basic wind velocity** v_b is function of wind direction, the time of the year and the expected lifetime of the considered structure. The determination of this basic wind speed assumes a fundamental wind velocity that depends on geographical location and its corresponding wind climate. This value is based on a statistical approach of the climatological studies, with the annual probability density of 2% exceedance and is listed in the National Annex. For Belgium this value ranges from 23m/s in the southwestern hillside up to 26 m/s at the coastal area in the northwest. To this fundamental value some reduction coefficients could be applied, reducing the basic wind velocity under specific conditions. One of them, the probability factor allows a reduction of the fundamental wind speed in accordance to a reduced lifetime of the structure up to a maximum reduction of 25% for temporary structures. In addition it is possible to reduce this fundamental wind speed even further by the seasonal factor and the directional factor, taking into account the statistical distribution of the wind speed respectively over the seasons and the wind directions. Taking into account the most favorable situation for all of these reduction parameters, a maximal reduction of up to 56% is allowed in case of a temporary structure erected during the months May to August for pure easterly winds, while the other winds will allow a maximal reduction of 48%. Nevertheless these reduction parameters are hardly used and typically set to 1.

$$v_b = c_{dir} \cdot c_{season} \cdot c_{prob} \cdot v_{b,0}$$

with:

- v_b the basic wind velocity
- $v_{b,0}$ the fundamental value of the basic wind velocity
- c_{dir} the directional factor which varies with the wind direction
- c_{season} the season factor which varies with the season
- c_{prob} the probability factor which varies with the lifetime of the structure



Figure A4: Basic wind speed Belgium – [8]

Wind direction	0° North	22,5°	37,75°	45°	56,25°	90° East	120°	150°	180° South	270° West
c_{dir}	1,00	1,00	0,95	0,90	0,85	0,85	0,90	0,95	1,00	1,00

Month	Jan	Feb	Mar	Apr	May	Jun	Jul	Aug	Sep	Oct	Nov	Dec
c_{season}	0,92	0,92	0,85	0,77	0,69	0,69	0,69	0,69	0,77	0,85	1,00	0,92

Return period (year)	1	2	5	10	20	50	100	200
c_{prob}	0,75	0,78	0,85	0,90	0,85	1,00	1,04	1,08

Table A1: Calculation values for c_{dir} , c_{season} and c_{prob} – [8]

The **roughness factor** $c_r(z)$ at a height z above the terrain is function of the roughness length, the terrain factor and the minimum height, or simply the considered terrain category that takes into account the influence of the surface roughness at the site upwind of the structure. The roughness will affect the mean wind velocity profile and the corresponding boundary layer. An increased roughness will reduce the mean wind velocity and increase the starting height of the atmospheric boundary layer because of the increased viscosity and inertia forces on one hand and the generated turbulence on the other hand.

The calculation of the roughness coefficient is simplified by the introduction of five terrain categories, ranging from open coastal areas to dens high-rise city centers. Each category is related to a specific roughness length that illustrates the height of the atmospheric boundary layer under which wind actions are negligible and a specific minimum height under which the mean roughness factor and thus also wind flow is assumed constant by considering the effect of the surrounding buildings on the wind flow. In addition, both factors will define a unique terrain factor for each terrain category. Beside, the mathematical calculation formula for the roughness factor illustrates that the Eurocode is based on a logarithmic wind velocity profile that considers the maximal height of the atmospheric boundary layer at 200 m, causing the free flow field of constant wind velocity to start here.

$$c_r(z) = K_r \cdot \ln\left(\frac{z}{z_0}\right) \quad \text{for} \quad z_{min} \leq z \leq z_{max}$$

$$c_r(z) = c_r(z_{min}) \quad \text{for} \quad z < z_{min}$$

with:

- $c_r(z)$ the roughness factor
- z_0 the roughness length
- K_r the terrain factor depending on the roughness length z_0 and calculated by:

$$K_r = 0,19 \cdot \ln\left(\frac{z_0}{z_{0,II}}\right)^{0,07}$$
- $z_{0,II}$ = 0,05 m (terrain category II)
- z_{min} the minimum height
- z_{max} to be taken at 200 m






Terrain category			z_0 [m]	z_{min} [m]
0		Sea, coastal area exposed to the open sea	0,003	1
I		Lakes or area with negligible vegetation and without obstacles	0,01	1
II		Area with low vegetation such as grass and isolated obstacles (trees, buildings) with separations of at least 20 obstacle heights	0,05	2
III		Area with regular cover of vegetation or buildings or with isolated obstacles with separations of maximum 20 obstacle heights (such as villages, suburban terrain, permanent forest)	0,3	5
IV		Area in which at least 15 % of the surface is covered with buildings and their average height exceeds 15 m	1,0	10

Table A2: Terrain categories – [8]

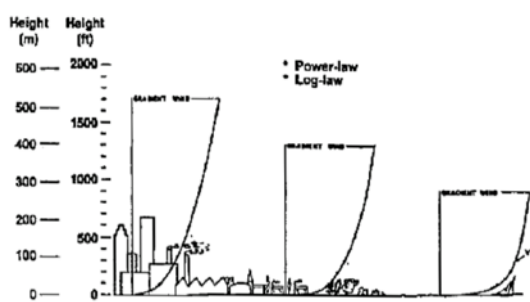


Figure A5: Atmospheric boundary layer - terrain roughness – [60]

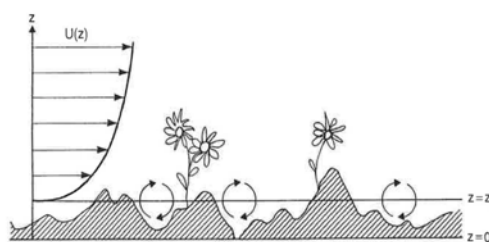


Figure A6: Roughness length z_0 – [16]

The **orography factor** $c_0(z)$ considers the effects of the site’s specific orography, such as significant hillsides, cliffs, ridges and slopes that could increase the basic wind velocity with a minimum of 5%. The detailed calculation of this coefficient for different situations is specified in Appendix A.3 of the Eurocode: *Numerical calculation of orography coefficients*, but is fixed at a minimum value of 1,00 for upwind slopes in the wind direction smaller than 3° or for Belgium smaller than 5%.

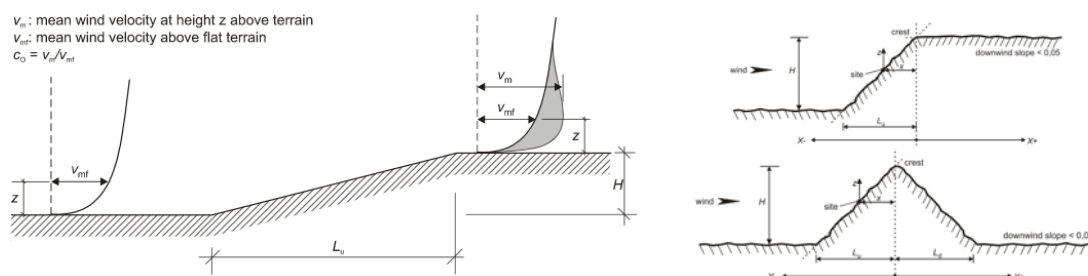


Figure A7: Orography factor calculation – [8]

In addition to the roughness and the orography factor one should investigate the presence of the surrounding environment with care (built structures, natural objects, etc.) as it will have significant influence on the wind load that will act on the structure. Large and considerably higher neighbouring structures could result (dependent on the properties of the structure) in exposure to increased wind velocities for certain wind directions by so-called falling winds, while on the other hand the vicinity of closely spaced buildings and obstacles could reduce the wind exposure as earlier mentioned.

After defining the mean wind velocity, one should also consider the fluctuating component of the wind to take into account for the turbulent nature of the wind.

The **turbulence intensity** $I_v(z)$ at height z is defined as the ratio of the standard deviation of the turbulence to the mean wind velocity. In this approach, the turbulence is considered as pure velocity fluctuations relative to mean wind velocity and is function of the terrain characteristics and the considered height above the terrain. The mathematical formula of the turbulence intensity illustrates as already mentioned, that an increased roughness results in an increased turbulence, which is thus associated with the terrain category that is considered. Beside, the turbulence intensity will decrease in the atmospheric boundary layer with an increasing height, and stabilize in the free flow field above. Finally the turbulence factor, which is generally set to 1, allows accounting for specific turbulence conditions at the site's location. For example the presence of surrounding structures upwind to the site that could generate vortex shedding in the wind flow that will act on the structure.

$$I_v(z) = \frac{\sigma_v}{v_m(z)} = \frac{K_I}{c_0(z) \cdot \ln(z/z_0)} \quad \text{for} \quad z_{min} \leq z \leq z_{max}$$

$$I_v(z) = I_v(z_{min}) \quad \text{for} \quad z < z_{min}$$

with:

- $I_v(z)$ the turbulence intensity
- σ_v the standard deviation of the turbulence and calculated by:
 $\sigma_v = K_r \cdot v_b \cdot K_I$
- $v_m(z)$ the mean wind velocity
- K_r the terrain factor
- K_I the turbulence factor
- v_b the basic wind velocity
- $c_0(z)$ the orography factor
- z_0 the roughness length

Finally, the **peak velocity pressure** $q_p(z)$ at height z that accounts for the mean and short-term velocity fluctuations is function of the turbulence intensity and the mean wind velocity, which can be translated to a basic velocity pressure corrected by a wind exposure factor. In fact, the peak velocity pressure is based on the kinetic energy transfer that takes place at the interaction surface between the colliding air molecules in the wind flow and considered structure. The total kinetic energy is consequently constituted of the kinetic energy associated with the mean velocity and the contributing turbulence fluctuations. Mark that the empirical factor 7 in the formula ensures a sufficient safe approach for the unpredictable character of the atmospheric turbulence in this mathematical representation of the wind.

$$q_p(z) = [1 + 7 \cdot I_v(z)] \cdot \frac{1}{2} \cdot \rho \cdot v_m^2(z) = c_e(z) \cdot q_b$$

with:

- $q_p(z)$ the peak velocity pressure
- $I_v(z)$ the turbulence intensity
- ρ the air density, which depends on the altitude, temperature and barometric pressure to be expected in the region during wind storms
- $v_m(z)$ the mean wind velocity
- $c_e(z)$ the exposure factor and calculated by:
 $c_e(z) = \frac{q_p(z)}{q_b}$
- q_b the basic velocity pressure and calculated by:
 $q_b = \frac{1}{2} \cdot \rho \cdot v_b^2$

Up to here there will be no differences in the case of membrane structures, since one merely represents the turbulent wind by a mathematical model that is based on a statistical approach with an annual probability density of 2% exceedance.

A.3 Wind interaction

As earlier mentioned, the wind interacts with any object that influences or disturbs the free wind flow. Consequently every building, bridge or structure that is placed in open air will be loaded by the wind. The amount of kinetic energy that is transferred from the wind flow to the structure depends on aerodynamic parameters of the object. The associated wind pressures or forces acting on the structure are corrected by pressure or force coefficients taking into account the aerodynamics of the structure. The net wind pressure acting on an object is calculated as the vector summation of the simultaneous wind pressures acting on the different element faces. For the main building components, i.e. walls and roofs and other two dimensional plate shaped elements, the resulting wind pressure is simplified to the summation of the pressures acting on its opposing faces. From this point of view one should note that roof structures are loaded differently for canopies or enclosed buildings. An open canopy roof is directly loaded by the wind acting on the upper and lower face of the structure, while a roof of an enclosed building is directly loaded on its outer face and indirectly on its inner face. Consequently, canopy roofs are calculated directly by net wind pressures, while roofs of enclosed buildings are calculated by vector summation of the external and internal wind pressures. During the calculations, one has to carefully consider the direction of the pressure. Pressure directed towards the surface is taken as positive, while suction directed away from the surface as negative.

$$w_{net} = w_e - w_i$$

with:

- w_{net} the net wind pressure
- w_e the wind pressure acting on the external surfaces
- w_i the wind pressure acting on the internal surfaces

The **wind pressure w_e acting directly on the external surfaces** is calculated by multiplying the peak velocity pressure, taken at the external reference height of the structure, with the appropriate aerodynamic correction factors for the considered (sub-) surfaces of the structure. These correction factors are defined as pressure coefficient distributions presented in the Eurocode for some common geometrical shapes.

$$w_e = q_p(z_e) \cdot c_{pe}$$

with:

- w_e the wind pressure acting on the external surfaces
- $q_p(z_e)$ the peak velocity pressure
- z_e the reference height for the external pressure
- c_{pe} the pressure coefficient for the external pressure

The **wind pressure w_i acting indirectly on the internal surfaces** is function of the porosity of the buildings envelope, the internal dimensions of the building and the angle of attack. The internal wind pressure is calculated in analogy to the external wind pressure, but the internal pressure coefficient depends on the dimensions and the distribution of the openings including background permeability, in the buildings envelope relative to the considered angle of attack. Since this thesis focuses on the external and the net pressure coefficients reference is made to Eurocode section 7.2.9 *Internal pressure*, for a detailed procedure to define appropriate internal pressure coefficients. For example, in case of a building with a dominant face, the internal pressure coefficients are defined as a fraction of the external pressure coefficients at the openings in the blown envelope's face.

In the case of a canopy roof, the **net wind pressure w_{net} acting on the surfaces** is calculated in analogy with wind pressure w_e acting directly on the external surfaces, by considering the appropriate net pressure coefficients presented in the Eurocode.

$$w_{net} = q_p(z) \cdot c_{p,net}$$

with:

- w_{net} the net wind pressure acting on the surface
- $q_p(z)$ the peak velocity pressure
- z the reference height for the net pressure
- $c_{p,net}$ the pressure coefficient for the net pressure

Finally the corresponding wind forces could be calculated from the surface pressures for the whole structure or a structural component. **The resulting wind force F_w** is the vector summation of the external, internal and frictional wind forces, respectively calculated from the external and internal pressures and the frictional forces.

$$\vec{F}_w = \vec{F}_{we} + \vec{F}_{wi} + \vec{F}_{fr}$$

$$F_{we} = c_s c_d \cdot \sum_{surfaces} w_e \cdot A_{ref} \quad \text{for external forces}$$

$$F_{wi} = \sum_{surfaces} w_i \cdot A_{ref} \quad \text{for internal forces}$$

$$F_{fr} = c_{fr} \cdot q_p(z_e) \cdot A_{fr} \quad \text{for friction forces}$$

with:

- F_w the resulting wind force
- F_{we} the external wind force
- F_{wi} the internal wind force
- F_{fr} the friction wind force
- $c_s c_d$ the structural factor constituted of a size factor c_s and a dynamic factor c_d , and accounts for the non-simultaneous occurrence of peak wind pressures and turbulence vibrations of the structure
- w_e the external pressure on the individual surface at height z_e
- w_i the external pressure on the individual surface at height z_i
- A_{ref} the reference area of the individual surface
- c_{fr} the frictional coefficient
- $q_p(z_i)$ the peak velocity pressure
- z_i the reference height for the individual external surface
- A_{fr} the area of external surface parallel to the wind

Wind acting parallel to the external faces induces frictional forces on the considered element acting along this parallel direction. The Eurocode describes that the effects of wind friction on the surface can be disregarded when the total area of all surfaces parallel with (or at a small angle to) the wind is equal to or less than 4 times the total area of all external surfaces perpendicular to the wind (windward and leeward). Consequently these frictional forces could have significant importance for straight canopy structures that are aligned parallel to the main wind direction. Nevertheless for double curved membrane structures the significance of friction could be disregarded because the norm vector of the membrane face will change for every infinitesimal point on the membrane, resulting in a parallel area smaller than 4 times the total perpendicular area for sufficiently curved membranes.

The structural factor $c_s c_d$ accounts for the non-simultaneous occurrence of peak wind pressures and turbulence vibrations of the structure. A detailed procedure to define this parameter that is generally set to 1, is presented in Eurocode section 6.3: *Structural Factor $c_s c_d$* .

A.4 Pressure coefficients

The last step in the modeling process of the wind actions is to determine appropriate aerodynamic coefficients for each structure. These aerodynamic parameters are defined in the Eurocode by pressure coefficient distributions, giving the effect of the wind per unit area for some common structures and building configurations. Most coefficients in EN 1991-1-4 are based on wind tunnel studies in a free flow field and are listed in tables for specified wind directions. All pressure distributions are given for standard rectangular ground plans and are based on geometrical proportions. In the case of unconventional structures sufficient safe assumptions have to be made while defining the pressure coefficients based on the provided data in the norm or additional wind investigation is required. The Eurocode provides internal and external pressure coefficients for an enclosed building situation and net pressure coefficients for a canopy structure. The internal and external pressure coefficients give respectively the effect of the wind on the internal and external building faces, while the net pressure coefficients account for the total effect of the wind on canopy surfaces. Beside, the Eurocode provides for each type of structure overall and local pressure coefficients respectively for areas equal to or larger than 10 m² and smaller than 1 m². It's observed that wind loads corresponding pressure coefficients depend on the size of the loaded area. For surface areas between 1 m² and 10 m² logarithmic interpolation is used if required. Nevertheless in most design cases the overall coefficients $c_{pe,10}$ are used for the overall load bearing calculation, while the local coefficients $c_{pe,1}$ are used to dimension small elements or fixings.

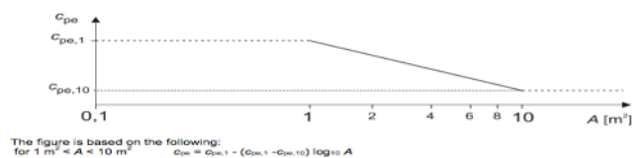


Figure A8: Interpolation overall and local pressure coefficients – [8]

Appendix B

Pressure Measurement Graphs 360°-rotation

Appendix B

B.1 Flat roof.....	74
B.2 Flat canopy.....	75
B.3 Duo-pitch roof	76
B.4 Duo-pitch canopy	77
B.5 Hypar roof.....	78
B.6 Hypar canopy	80

List of Figures

Figure B1: Continuous 360°-rotation – flat roof – upper face.....	74
Figure B2: Continuous 360°-rotation – flat roof – lower face	74
Figure B3: Continuous 360°-rotation – flat canopy – upper face	75
Figure B4: Continuous 360°-rotation – flat canopy – lower face	75
Figure B5: Continuous 360°-rotation – duo-pitch roof with pitch inclinations of 30° – upper face	76
Figure B6: Continuous 360°-rotation – duo-pitch roof with pitch inclinations of 30° – lower face.....	76
Figure B7: Continuous 360°-rotation – duo-pitch canopy with pitch inclinations of 30° – upper face.....	77
Figure B8: Continuous 360°-rotation – duo-pitch canopy with pitch inclinations of 30° – lower face	77
Figure B9: Continuous 360°-rotation – hypar roof with a shape parameter of 11,3 – upper face – high corner.....	78
Figure B10: Continuous 360°-rotation – hypar roof with a shape parameter of 11,3 – upper face – low corner	78
Figure B11: Continuous 360°-rotation – hypar roof with a shape parameter of 11,3 – lower face – high corner	79
Figure B12: Continuous 360°-rotation – hypar roof with a shape parameter of 11,3 – lower face – low corner.....	79
Figure B13: Continuous 360°-rotation – hypar canopy with a shape parameter of 11,3 – upper face – high corner	80
Figure B14: Continuous 360°-rotation – hypar canopy with a shape parameter of 11,3 – upper face – low corner	80
Figure B15: Continuous 360°-rotation – hypar canopy with a shape parameter of 11,3 – lower face – high corner	81
Figure B16: Continuous 360°-rotation – hypar canopy with a shape parameter of 11,3 – lower face – low corner	81

B.1 Flat roof

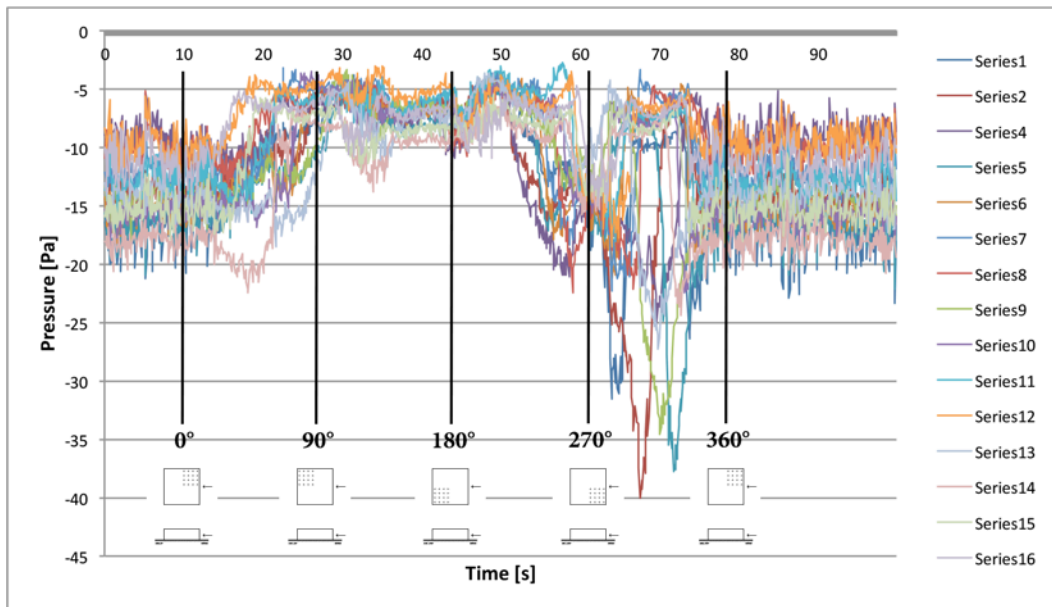


Figure B1: Continuous 360°-rotation – flat roof – upper face

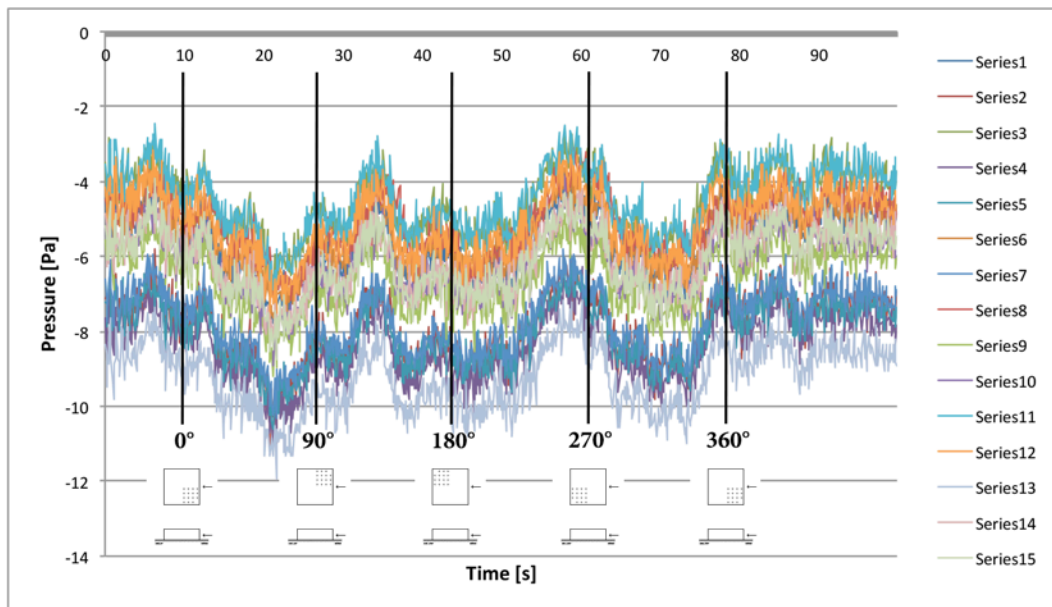


Figure B2: Continuous 360°-rotation – flat roof – lower face

B.2 Flat canopy

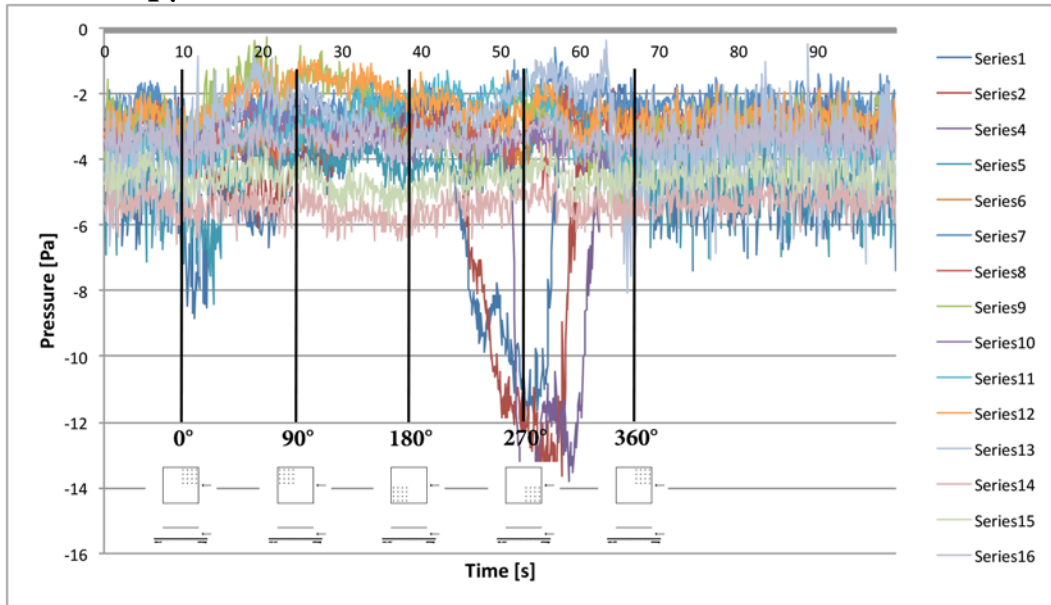


Figure B3: Continuous 360°-rotation – flat canopy – upper face

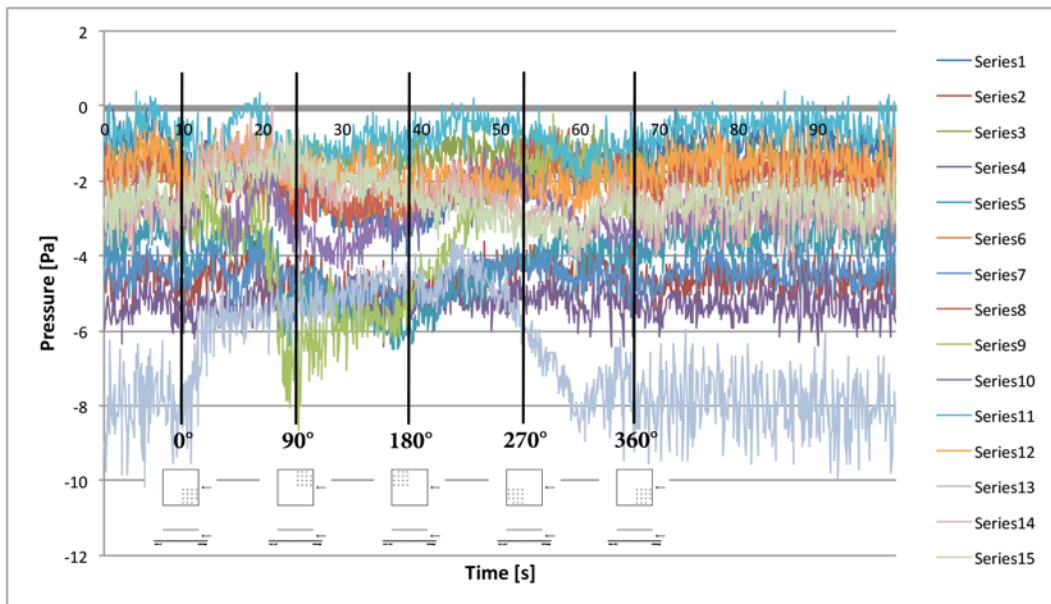


Figure B4: Continuous 360°-rotation – flat canopy – lower face

B.3 Duo-pitch roof

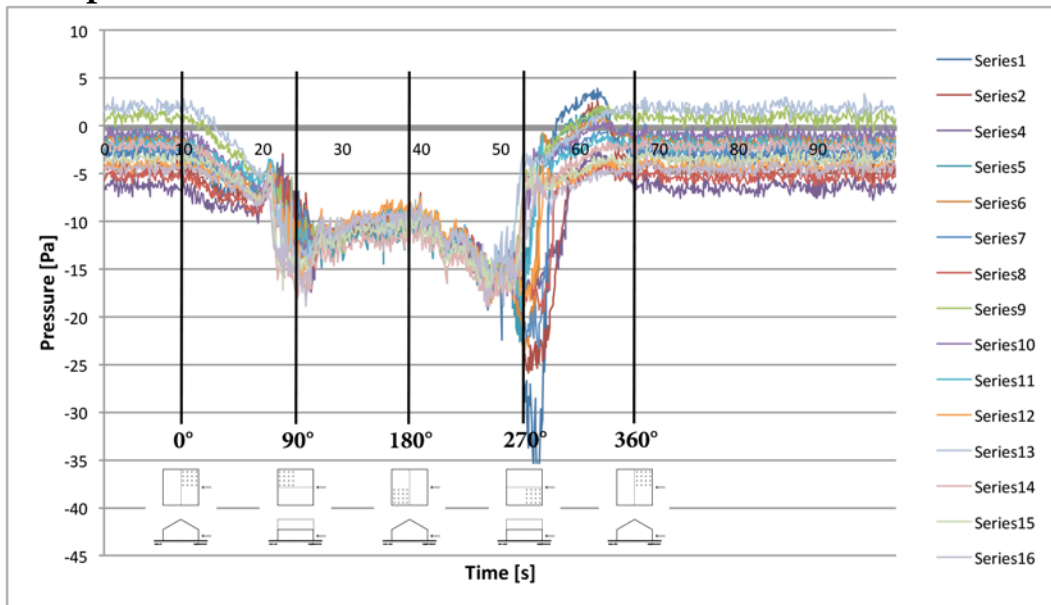


Figure B5: Continuous 360°-rotation – duo-pitch roof with pitch inclinations of 30° – upper face

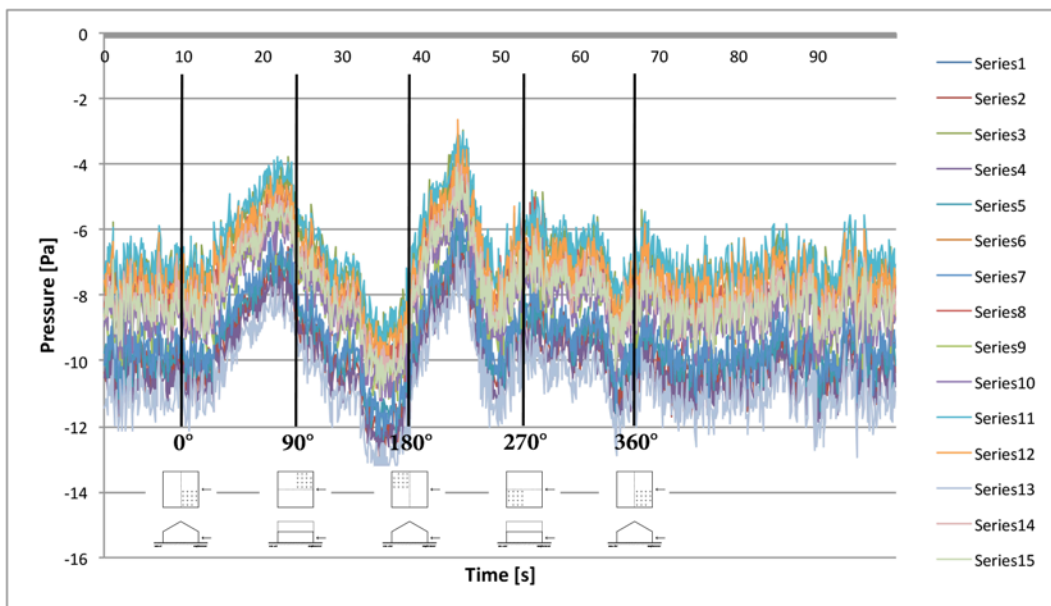


Figure B6: Continuous 360°-rotation – duo-pitch roof with pitch inclinations of 30° – lower face

B.4 Duo-pitch canopy

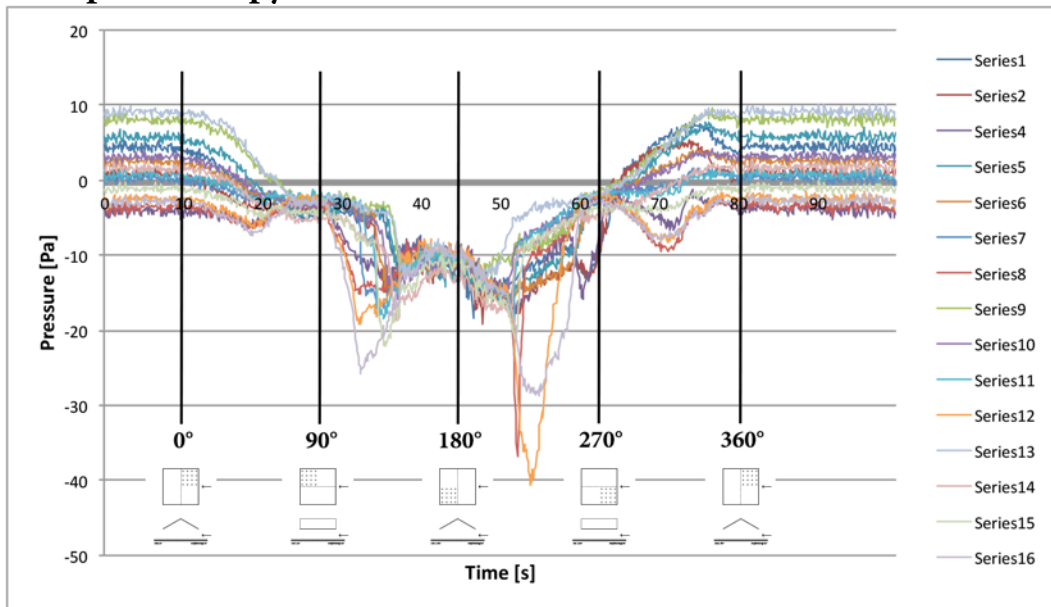


Figure B7: Continuous 360°-rotation – duo-pitch canopy with pitch inclinations of 30° – upper face

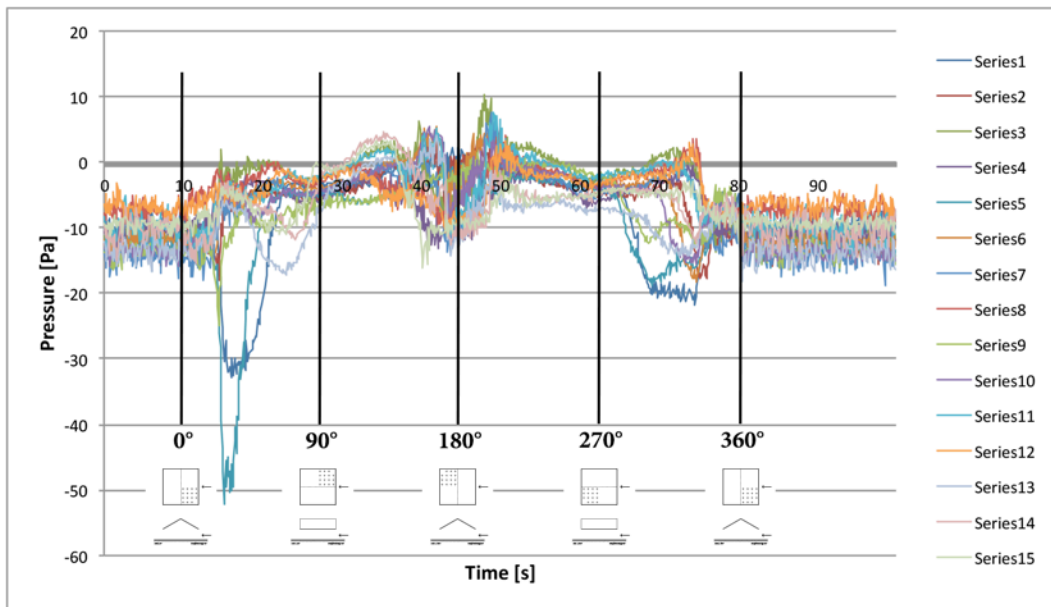


Figure B8: Continuous 360°-rotation – duo-pitch canopy with pitch inclinations of 30° – lower face

B.5 Hypar roof

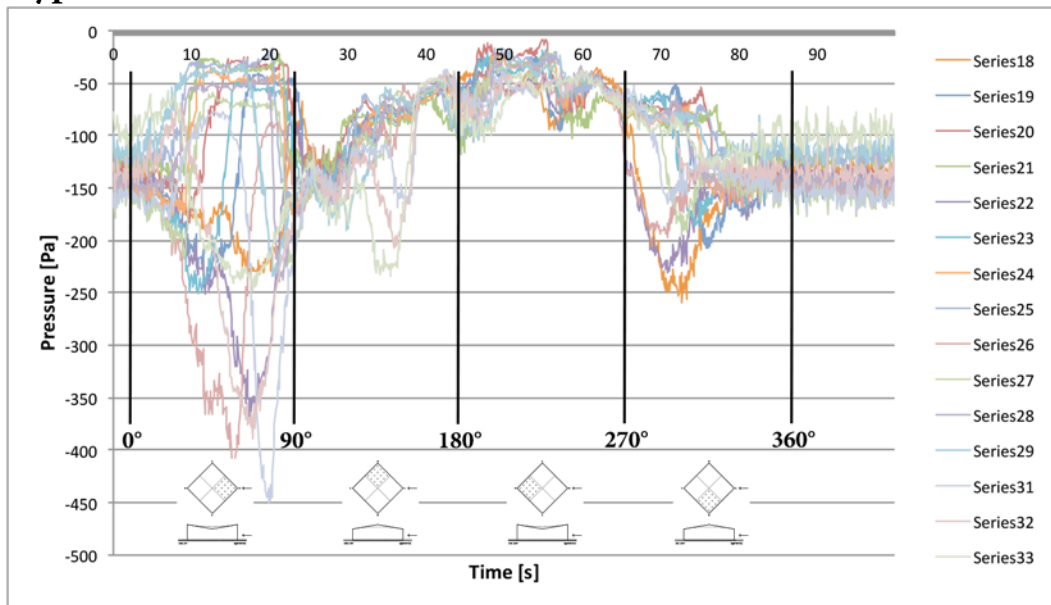


Figure B9: Continuous 360°-rotation – hypar roof with a shape parameter of 11,3 – upper face – high corner

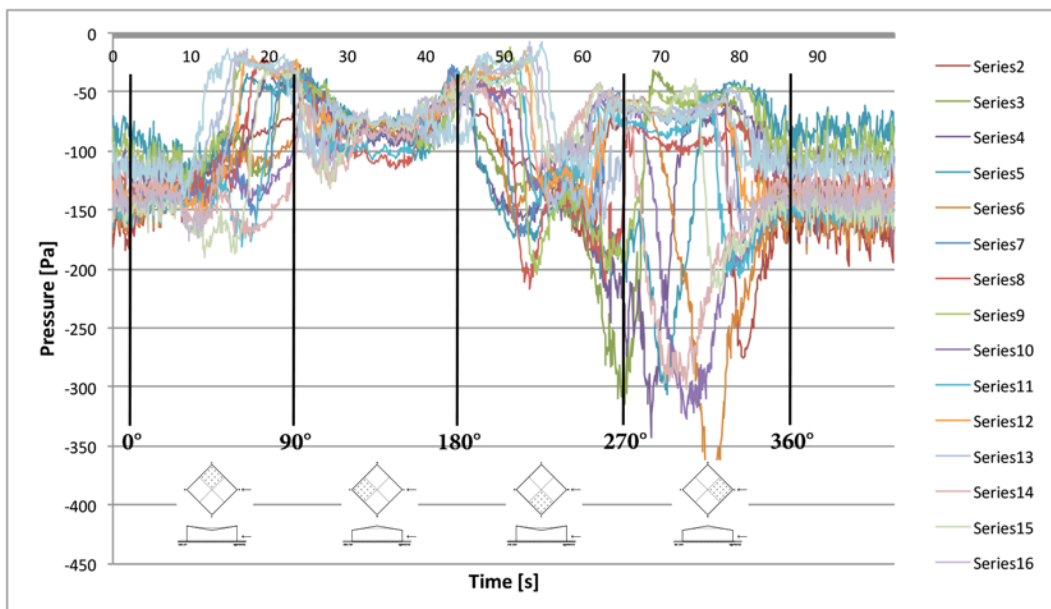


Figure B10: Continuous 360°-rotation – hypar roof with a shape parameter of 11,3 – upper face – low corner

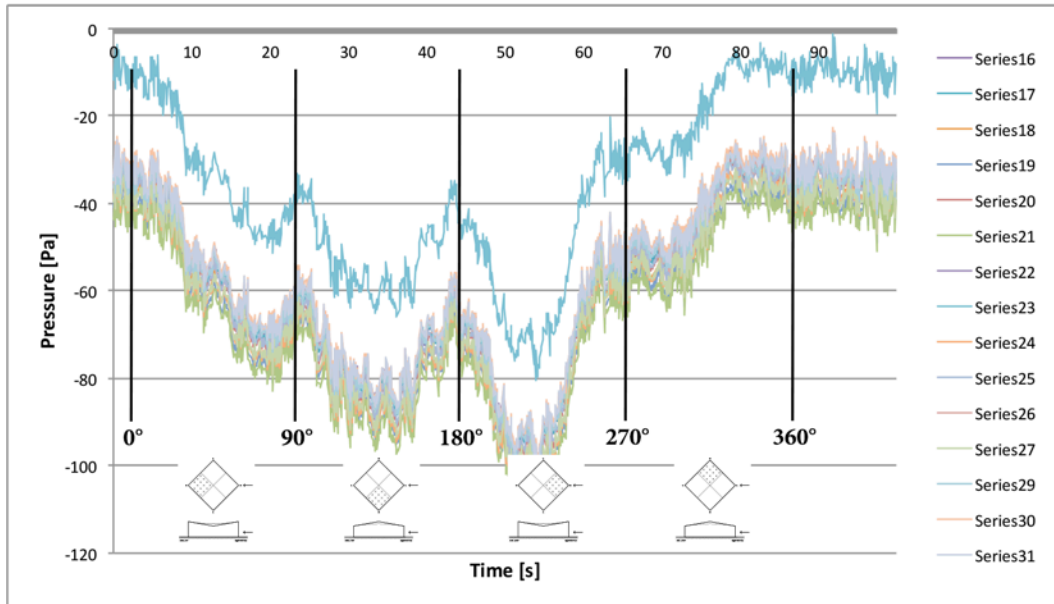


Figure B11: Continuous 360°-rotation – hypar roof with a shape parameter of 11,3 – lower face – high corner

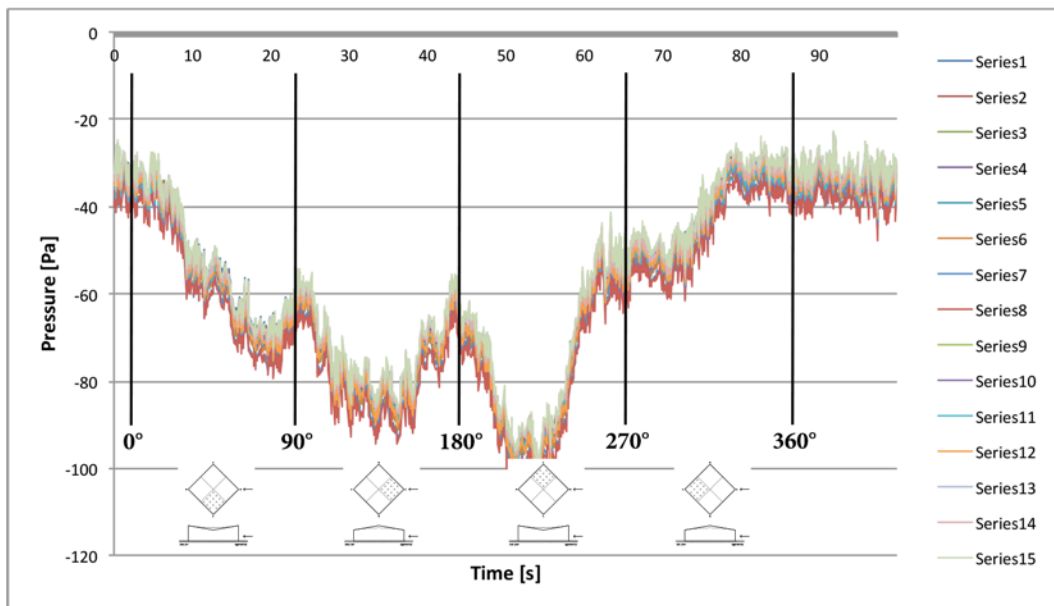


Figure B12: Continuous 360°-rotation – hypar roof with a shape parameter of 11,3 – lower face – low corner

B.6 Hypar canopy

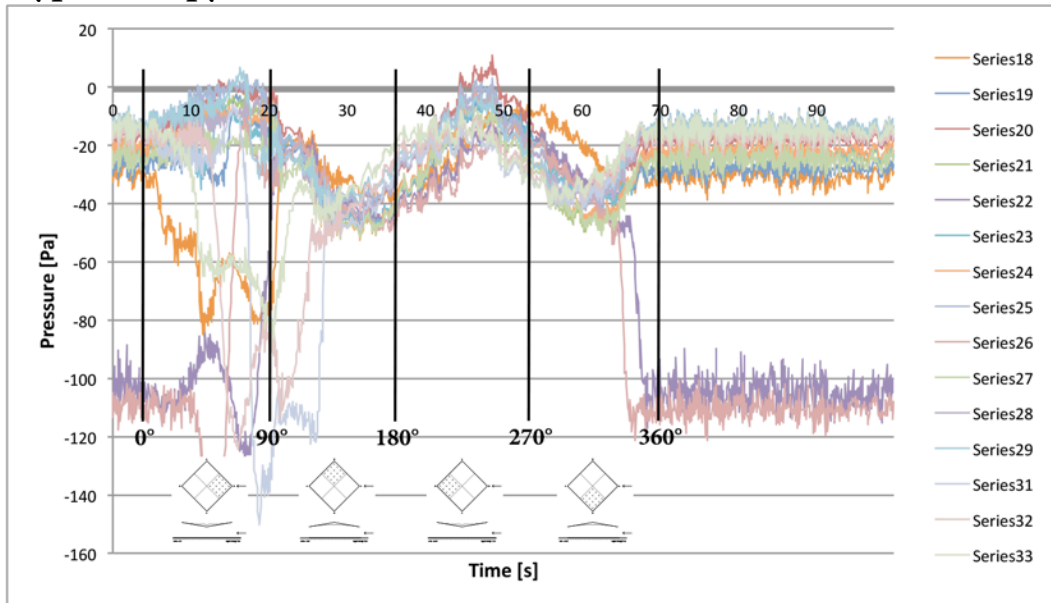


Figure B13: Continuous 360°-rotation – hypar canopy with a shape parameter of 11,3 – upper face – high corner

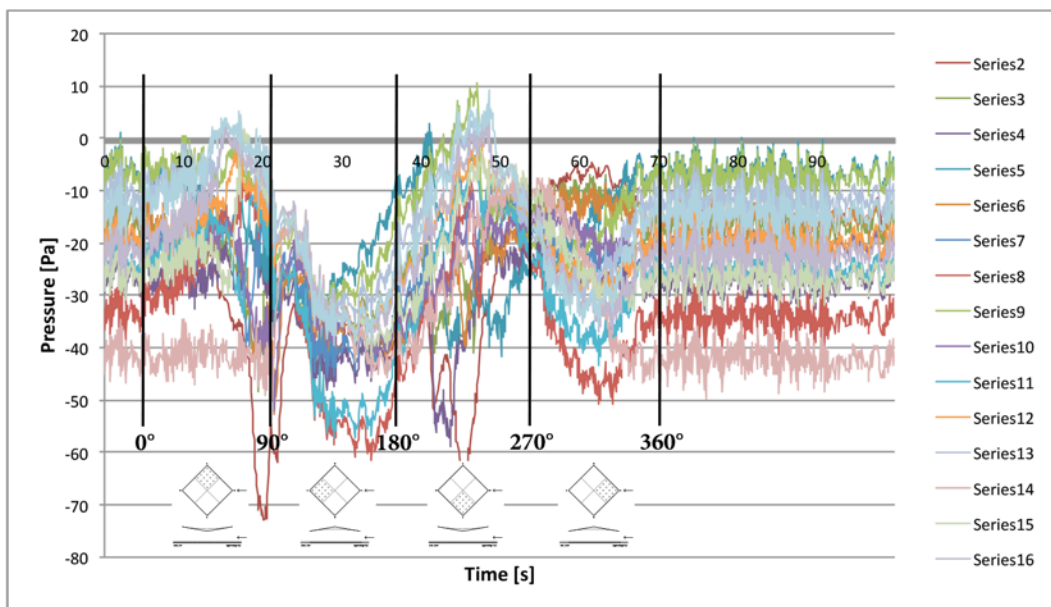


Figure B14: Continuous 360°-rotation – hypar canopy with a shape parameter of 11,3 – upper face – low corner

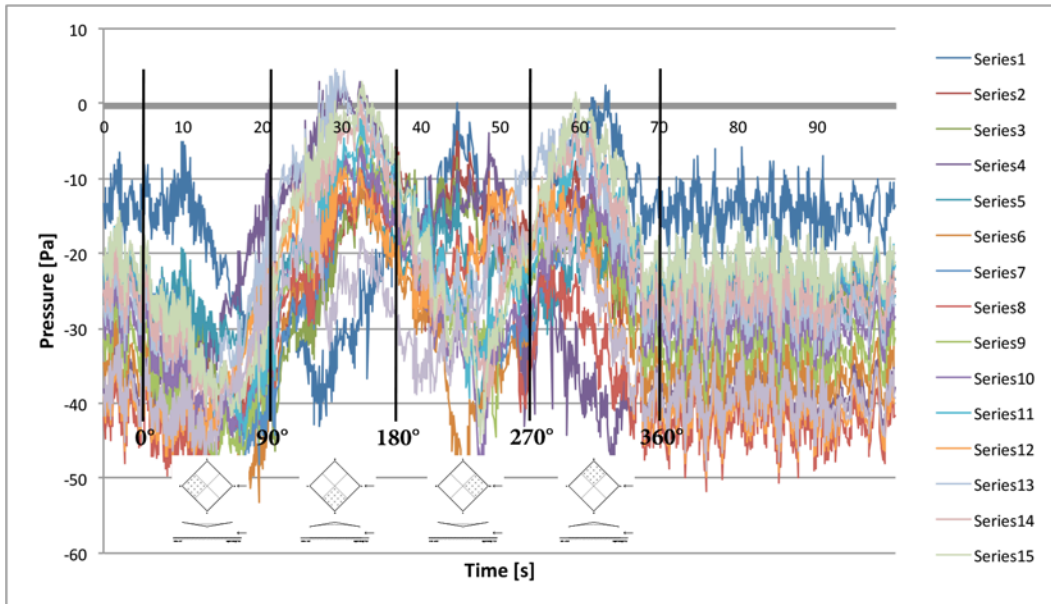


Figure B15: Continuous 360°-rotation – hypar canopy with a shape parameter of 11,3 – lower face – high corner

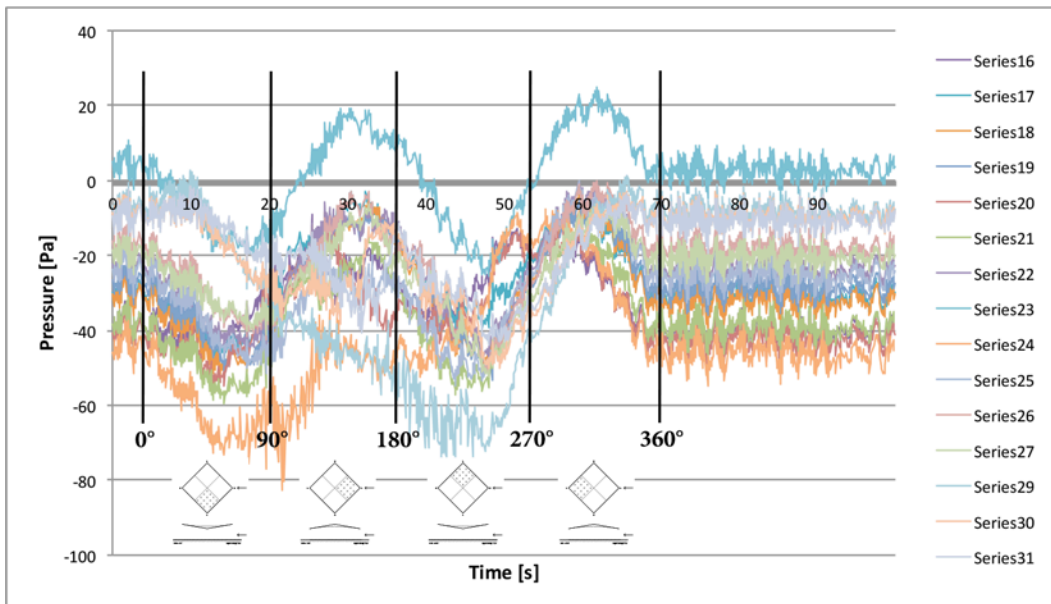


Figure B16: Continuous 360°-rotation – hypar canopy with a shape parameter of 11,3 – lower face – low corner

Appendix C

Pressure Coefficient Distributions Discrete angles of attack

Appendix C

C.1 Flat roof.....	83
C.2 Flat canopy.....	83
C.3 Duo-pitch roof	84
C.4 Duo-pitch canopy	85
C.5 Hypar roof.....	88
C.6 Hypar canopy	89

List of Figures

Figure C1: External pressure coefficient distribution flat roof.....	83
Figure C2: Net pressure coefficient distribution flat canopy (Left) External pressure coefficient distribution flat canopy (Right)	83
Figure C3: External pressure coefficient distribution duo-pitch roof with pitch inclinations of 30°	84
Figure C4: Net pressure coefficient distribution duo-pitch canopy with pitch inclinations of 30°	85
Figure C5: External pressure coefficient distribution duo-pitch canopy with pitch inclinations of 30°	86
Figure C6: Net pressure coefficient distribution duo-pitch canopy with pitch inclinations of 30° (Left) Net pressure coefficient distribution duo-pitch canopy with pitch inclinations of 30° - freeflow field (Right)	87
Figure C7: External pressure coefficient distribution duo-pitch canopy with pitch inclinations of 30° (Left) External pressure coefficient distribution duo-pitch canopy with pitch inclinations of 30° - freeflow field (Right)	87
Figure C8: External pressure coefficient distribution hypar roof with a shape parameter of 11,3	88
Figure C9: Net pressure coefficient distribution hypar canopy with a shape parameter of 11,3	89
Figure C10: External pressure coefficient distribution hypar canopy with a shape parameter of 11,3	90

C.1 Flat roof

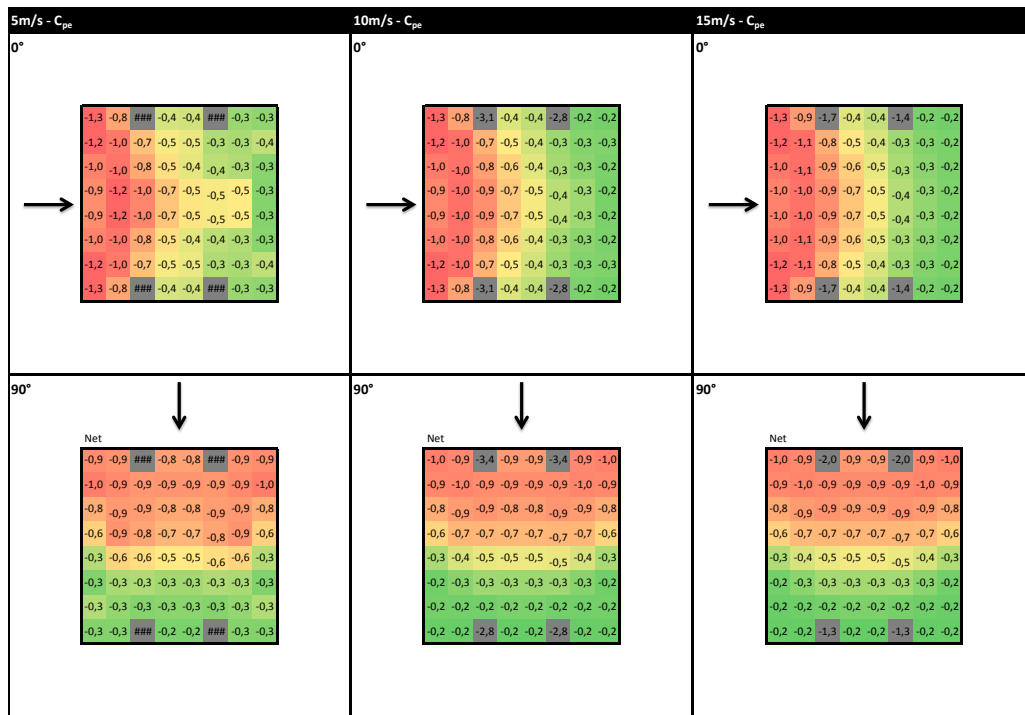


Figure C1: External pressure coefficient distribution flat roof

C.2 Flat canopy

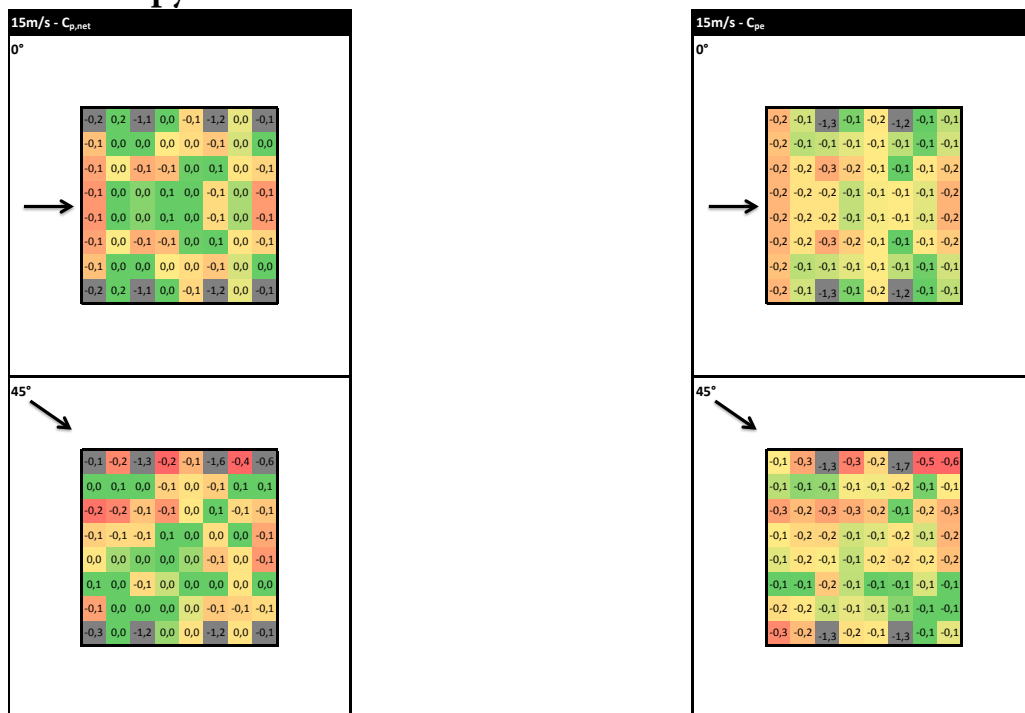


Figure C2: Net pressure coefficient distribution flat canopy (Left)
External pressure coefficient distribution flat canopy (Right)

C.3 Duo-pitch roof

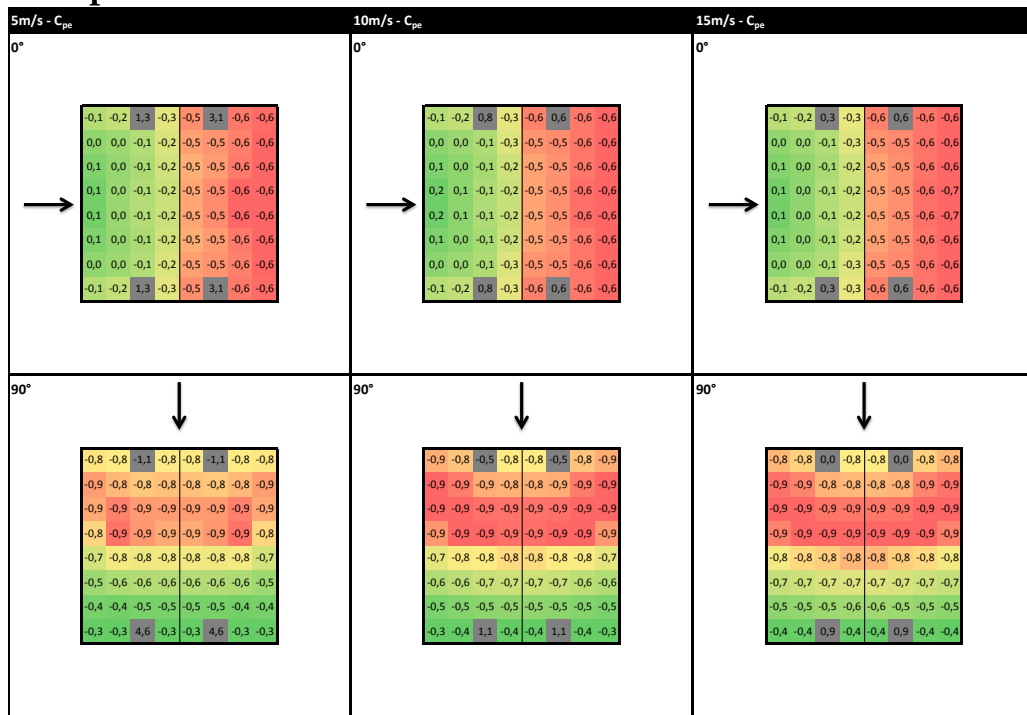


Figure C3: External pressure coefficient distribution duo-pitch roof with pitch inclinations of 30°

C.4 Duo-pitch canopy

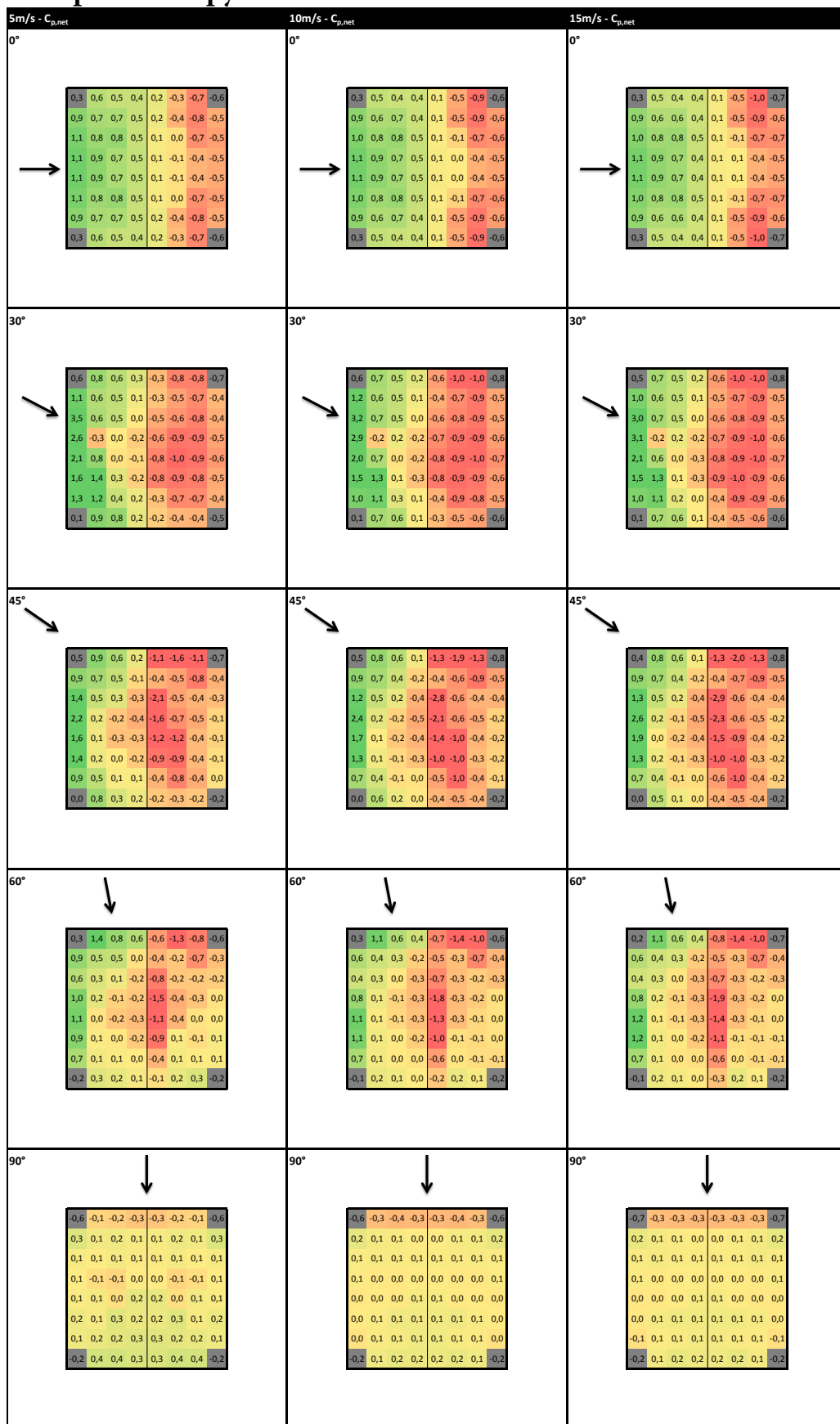


Figure C4: Net pressure coefficient distribution duo-pitch canopy with pitch inclinations of 30°

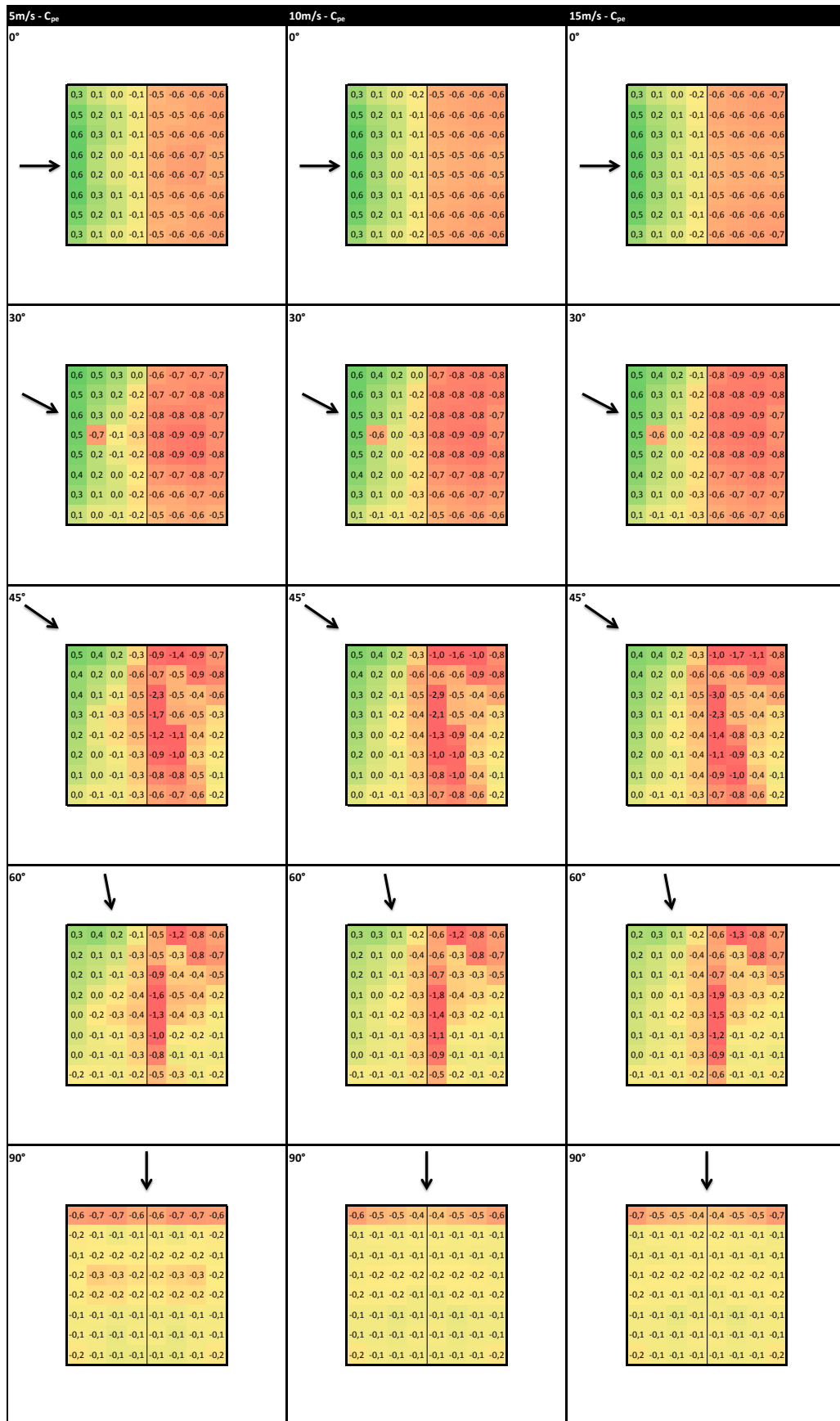


Figure C5: External pressure coefficient distribution duo-pitch canopy with pitch inclinations of 30°

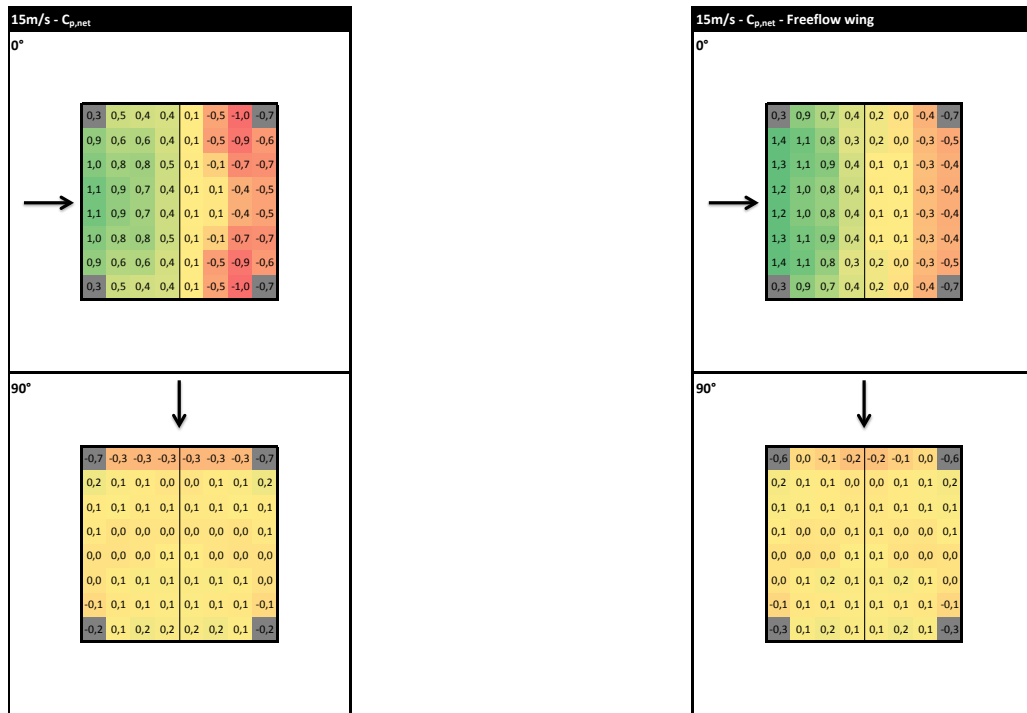


Figure C6: Net pressure coefficient distribution duo-pitch canopy with pitch inclinations of 30° (Left)
 Net pressure coefficient distribution duo-pitch canopy with pitch inclinations of 30° - freeflow field (Right)

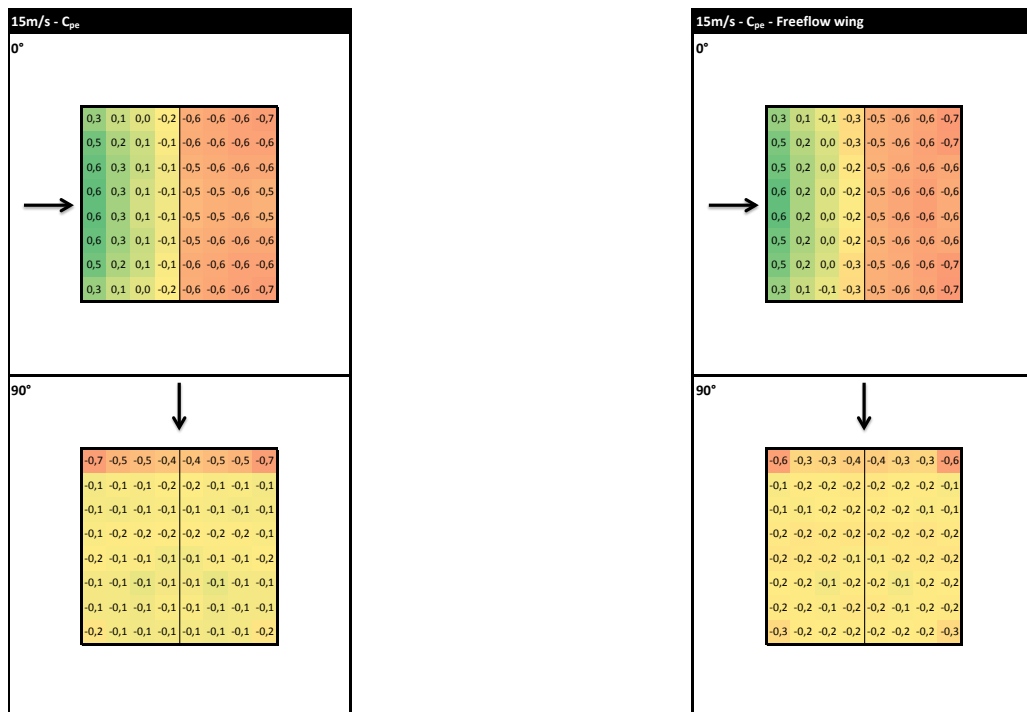


Figure C7: External pressure coefficient distribution duo-pitch canopy with pitch inclinations of 30° (Left)
 External pressure coefficient distribution duo-pitch canopy with pitch inclinations of 30° - freeflow field (Right)

C.5 Hypar roof

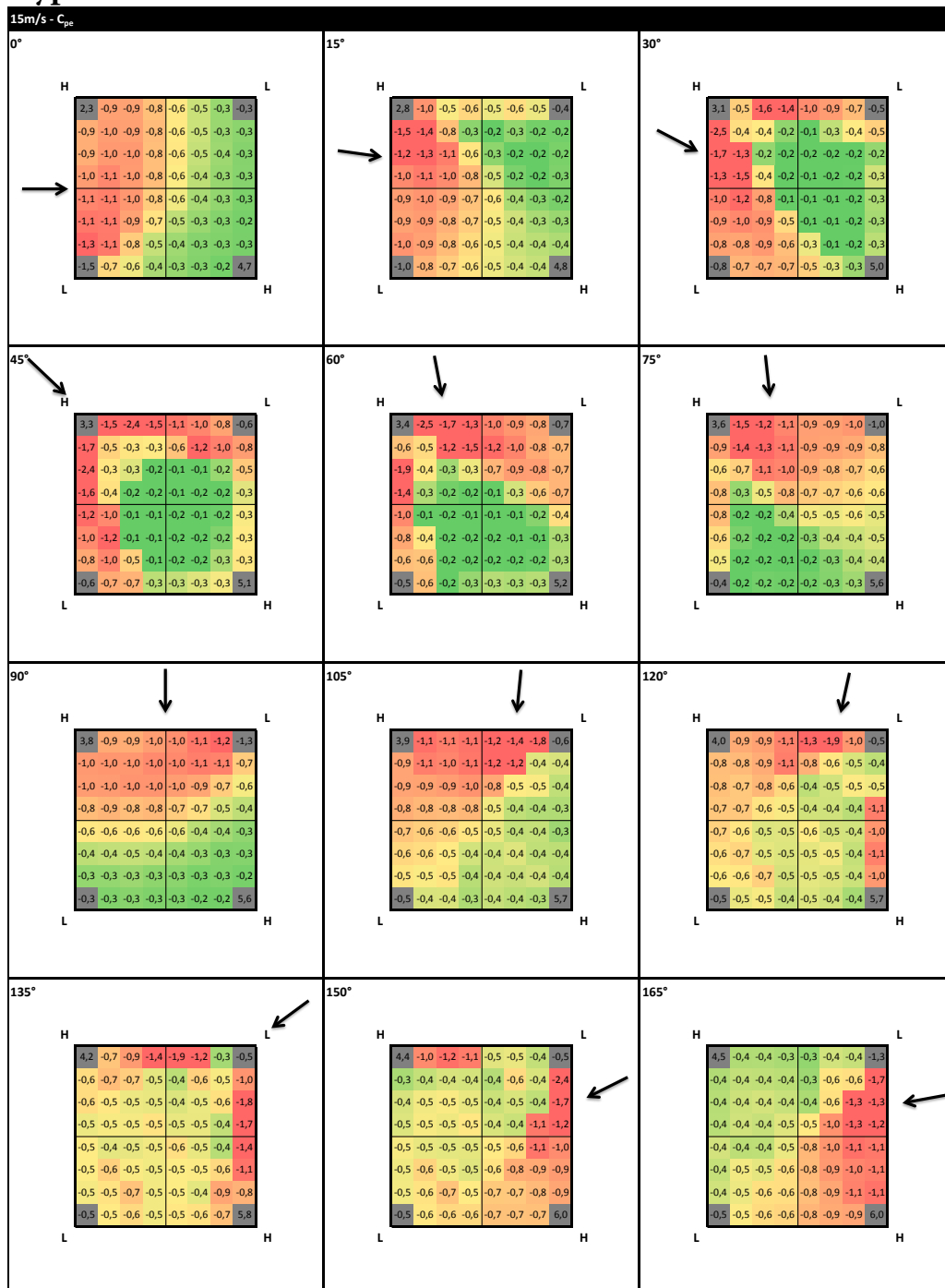


Figure C8: External pressure coefficient distribution hypar roof with a shape parameter of 11,3

C.6 Hypar canopy

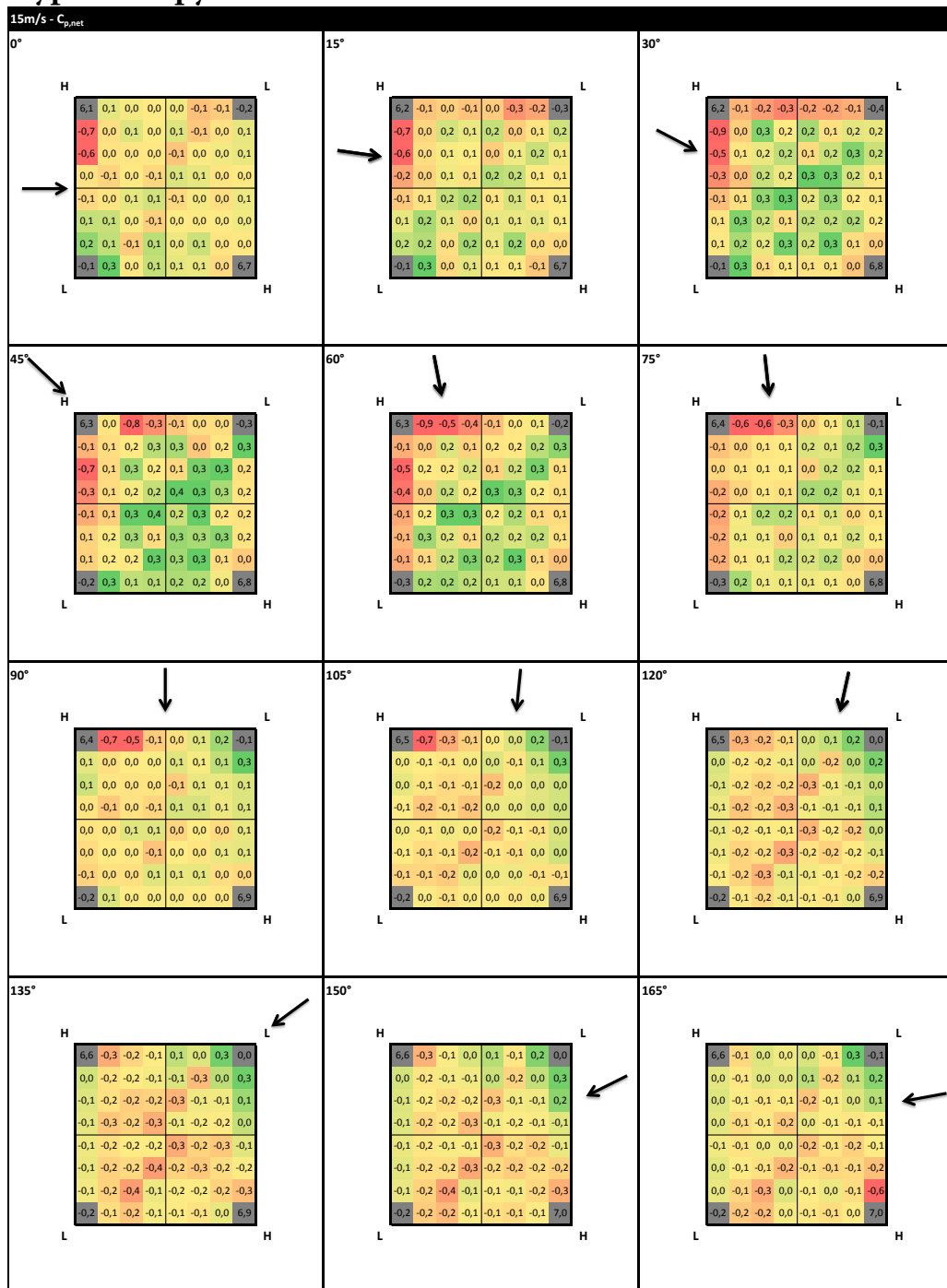


Figure C9: Net pressure coefficient distribution hypar canopy with a shape parameter of 11,3

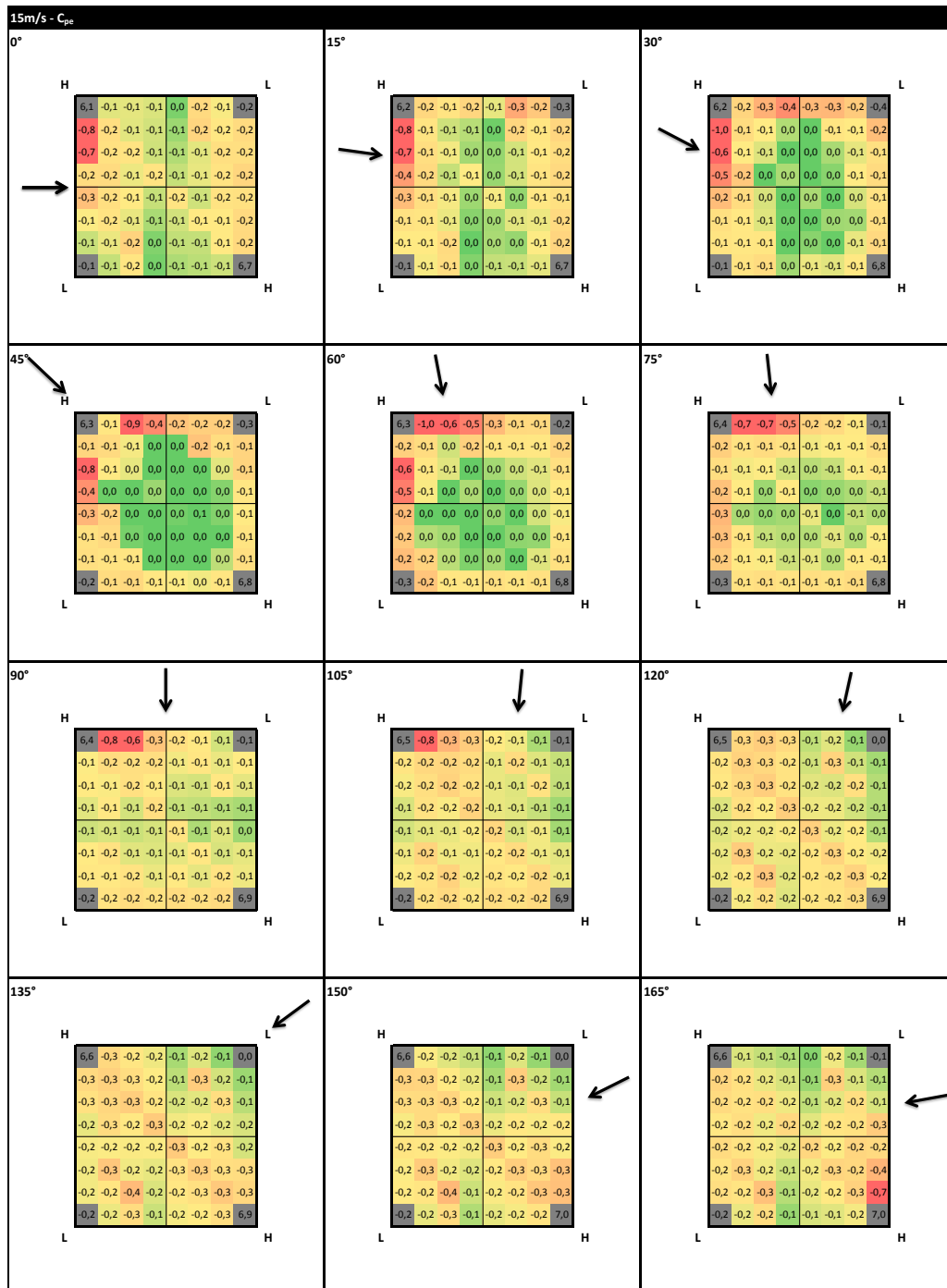


Figure C10: External pressure coefficient distribution hyper canopy with a shape parameter of 11,3